UNIVERSITY OF CALIFORNIA

Santa Barbara

Mapping and quantifying methane emissions from local sources using airborne imaging spectrometers

A dissertation submitted in partial satisfaction

of the requirements for the degree Doctor of Philosophy

in Geography

by

Andrew Kenji Thorpe

Committee in charge:

Professor Dar Roberts, Chair
Professor Joseph McFadden
Dr. Christopher Funk
Dr. Christian Frankenberg, Jet Propulsion Laboratory, California Institute of Technology

June 2015

The dissertation of Andrew Kenji Thorpe is approved.

Joseph McFadden

Christopher Funk

Christian Frankenberg

Dar Roberts, Committee chair

May 2015

Mapping and quantifying methane emissions from local sources using airborne imaging spectrometers

by

Andrew Kenji Thorpe

Acknowledgments

This dissertation could not have been completed without the support and guidance of friends, family, and colleagues. First, I would like to thank Dar Roberts for the opportunity to join his lab and pursue this research. Over these past few years, I have greatly appreciated your feedback, mentorship, and am grateful for the research funding you have provided. Thanks for helping me obtain additional funding to support this research and the opportunity to transition full time to the Jet Propulsion Lab before completing my degree.

I would also like to thank my additional committee members, Chris Funk, Joe McFadden, and Christian Frankenberg. Chris, your experience with image filtering really helped to initiate the search for methane plumes in AVIRIS imagery. Joe, I have always appreciated your insightful comments. Christian, it has been a real pleasure working with you over the last few years. I have appreciated your expertise and willingness to take the time to bring me up to speed when I started at JPL.

I would like to thank Philip Dennison for being a great collaborator over the years, for whom I consider an honorary committee member. In addition, I would like to thank Robert Green, the AVIRIS/AVIRIS-NG team, and Andrew Aubrey for their continued support at JPL. I want to thank everyone in the VIPER lab at UCSB for the wonderful environment that made graduate school less of a grind. Specifically, I would like to thank Eliza Bradley, Seth Peterson, and Keely Roth for helping me get situated as I began graduate school. Over the years, the administrative staff in the Department of Geography and computing support by Dylan Parenti have been greatly appreciated.

Thanks so much to my family, who has been supportive of me over the years despite a somewhat circuitous path to graduate school. Finally, thank you Katie for stepping into my car one rainy Brooklyn morning back in 2009, driving to California, and embarking on graduate school together. You have kept me strong, made me laugh, and been by my side every step of the way in completing this degree. For that I am grateful.

Vita of Andrew Kenji Thorpe

Education

University of California, Santa Barbara, Santa Barbara, CA, 2015
-Ph.D. in Geography

Brown University, Providence, RI, 2004
-B.S. in Geological Sciences with Honors, Magna Cum Laude

Experience

Researcher, Jet Propulsion Laboratory, California Institute of Technology, Pasadena, CA, Oct. 2012-Present

-Contributed to planning two AVIRIS-NG flight campaigns for methane detection

-Performed sensitivity analysis to determine gas detection limits of algorithms and imaging spectrometers

-Collaborated with LANL researchers to compare results from AVIRIS-NG and plume model

Graduate Student Researcher, University of California, Santa Barbara, Santa Barbara, CA, Sept. 2009-Present

-Developed gas retrieval algorithms for AVIRIS and AVIRIS-NG imaging spectrometers for grant: Airborne instrument methane retrieval processing and algorithm development, Sept. 2012-Present

-Implemented trace gas detection algorithm for grant: Hyperspectral mapping of trace gas emissions, June 2009-Aug. 2012

Analyst, GreenOrder, New York, NY, Jan. 2007-July 2008

-Contributed to consulting engagements for multiple Fortune 500 and startup clients to align sustainability with business objectives

-Created detailed environmental scorecard and product claims to quantify lifecycle benefits of building material produced with 91% less energy and 97% fewer carbon dioxide emissions than traditional products

Manager, Visual Motion Productions, New York, NY, Nov. 2005-June 2006

-Managed studio operations and projects for adventure/sport photographer, Jorg Badura

-Planned photo shoots in remote locations, including Costa Rica, Colorado, and Florida, leading to spreads in Newsweek, Men's Health, and Self Magazine

Researcher, Free University, Berlin, Germany, Oct. 2004-Aug. 2005

-Processed and interpreted digital imagery from the HRSC Camera on ESA's Mars Express mission

-Developed press releases and edited papers to contribute to knowledge of Martian geology

Awards and honors

-NASA Planetary Science Summer School (PSSS), 2014

-AAG Student Illustrated Paper Competition Award, 2014

-SPIE Optics and Photonics Education Scholarship, 2013

-U.S. Geospatial Intelligence Foundation (USGIF) Graduate Scholarship, 2012

-Sigma Xi membership for excellence in academics and research, 2004

-Brown University Scholarship for Field Research, 2003

-Juneau Ice-Field Research Program Scholarship, 2003

Funding awarded

-NASA Earth and Space Science Fellowship (NESSF), Mapping local greenhouse gas emissions using airborne imaging spectrometry, $60,000, 2014-2015

-Jet Propulsion Laboratory Subcontract, Airborne instrument methane retrieval processing and algorithm development, $175,004, 2013-2015

-Department of Geography Dangermond Travel Scholarship, $600, 2015

-Department of Geography Dangermond Travel Scholarship, $600, 2014

-Department of Geography Dangermond Travel Scholarship, $500, 2013

-University of California, Santa Barbara, Doctoral Student Travel Grant, $685, 2013

-Department of Geography Dangermond Travel Scholarship, $1,450, 2012

-NASA California Space Grant, Mapping methane emissions from a cattle feedlot using imaging spectroscopy, $1,000, 2010

-NASA Alaska Space Grant, $1,000, 2003

Publications

Thorpe, A.K., Frankenberg, C., Aubrey, A.D., Roberts, D.A., et al. (2015). Measuring methane concentrations from a controlled release experiment using the next generation Airborne Visible/Infrared Imaging Spectrometer (AVIRIS-NG). *Remote Sensing of Environment*, Manuscript submitted.

Thompson, D.R., Leifer, I., Bovensmann, H., Eastwood, M.L., Green, R.O., Eastwood, M.L., Fladeland, M., Frankenberg, C., Gerilowski, K., Green, R.O., Kratwurst, S., Krings, T., Luna, B., **Thorpe, A.K.** (2015). Real time remote detection and measurement for airborne imaging spectroscopy: A case study with methane. *Atmospheric Measurement Techniques*, Manuscript submitted.

Aubrey, A.D., Frankenberg, C., Green, R.O., Eastwood, M.L., Thompson, D.R., and **Thorpe, A.K.** (2015). Crosscutting airborne remote sensing technologies for oil and gas and earth science applications, paper presented at Offshore Technology Conference, Houston, Texas.

Thorpe, A.K., Frankenberg, C., Roberts, D.A. (2014). Retrieval techniques for airborne imaging of methane concentrations using high spatial and moderate spectral resolution: Application to AVIRIS. *Atmospheric Measurement Techniques, 7*, 491-506.

Dennison, P.E., **Thorpe, A.K.**, Qi, Y., Roberts, D.A., Green, R.O., Bradley, E.S., Funk, C.C. (2013). High spatial resolution mapping of elevated atmospheric carbon dioxide using

airborne imaging spectroscopy: Radiative transfer modeling and power plant plume detection. *Remote Sensing of Environment, 139*, 116-129.

Dennison, P.E., **Thorpe, A.K.**, Qi, Y., Roberts, D.A., Green, R.O. (2013). Modeling sensitivity of imaging spectrometer data to carbon dioxide and methane plumes. *Proc. Workshop on Hyperspectral Image and Signal Processing: Evolution in Remote Sensing (WHISPERS).*

Thorpe, A.K., Roberts, D.A., Bradley, E.S., Funk, C.C., Dennison, P.E., Leifer I. (2013). High resolution mapping of methane emissions from marine and terrestrial sources using a Cluster-Tuned Matched Filter technique and imaging spectrometry. *Remote Sensing of Environment, 134*, 305-318.

Thorpe, A.K., Roberts, D.A., Dennison, P.E., Bradley, E.S., Funk, C.C. (2012). Point source emissions mapping using the Airborne Visible/Infrared Imaging Spectrometer (AVIRIS). *Proc. SPIE, 8390*, 839013.

Elkins-Tanton, L.T., Draper, D.S., Agee, C.B., Jewell, J., **Thorpe, A.**, Hess, P.C. (2007). The last lavas erupted during the main phase of the Siberian flood volcanic province: results from experimental petrology. *Contributions to Mineralogy and Petrology, 153*, 191-209.

Van Gasselt, S., Reiss, D., **Thorpe, A.K.**, Neukum, G. (2005). Seasonal variations of polygonal thermal contraction crack patterns in a south polar trough, Mars. *Journal of Geophysical Research-Planets, 110*, E08002.

Published abstracts and presentations

Aubrey, A.D., Frankenberg, C., Green, R.O., Eastwood, M.L., Thompson, D.R., and **Thorpe, A.K.** (2015). Crosscutting airborne remote sensing technologies for oil and gas and earth science applications. In, Offshore Technology Conference. Houston, TX.

Thorpe, A.K., Frankenberg, C., Roberts, D.A., Aubrey, A.D., Green. R.O., Hulley, G., Hook, S.J. (2014). Mapping methane concentrations from a controlled release experiment using airborne imaging spectroscopy. In, American Geophysical Union Fall Meeting. San Francisco, CA.

Lawson, M.J., Amador, E.S., Carrier, B.L., Albuja, A., Bapst, J., Cahill, K.R., Ebersohn, F., Gainey, S., Gartrelle, G., Greenberger, R.N., Hale, J.M., Johnston, S., Olivares, J., Parcheta, C.E., Sheehan, J. P., **Thorpe, A.K.**, Zareh, S.K. (2014). Enceladus Environmental Explorer (EVE): A Mission Concept. In, American Geophysical Union Fall Meeting. San Francisco, CA.

Thorpe, A.K., Frankenberg, C., Roberts, D.A., Aubrey, A.D. (2014). Retrieval of methane concentrations using the airborne imaging spectrometers AVIRIS and AVIRISng. In, HyspIRI Science Workshop. Pasadena, CA.

Thorpe, A.K., Frankenberg, C., Roberts, D.A., Aubrey, A.D. (2014). Quantifying methane emissions from natural and anthropogenic sources using AVIRIS-like instruments (**invited**). In, Ecological Society of America Annual Meeting. Sacramento, CA.

Thorpe, A.K., Frankenberg, C., Roberts, D.A., Aubrey, A.D. (2014). Airborne imaging of methane concentrations from a controlled release experiment using the imaging spec-

trometer AVIRISng. In, Ecological Society of America Annual Meeting. Sacramento, CA.

Thorpe, A.K., Frankenberg, C., Roberts, D.A., Aubrey, A.D. (2014). Retrieval of methane concentrations using airborne imaging spectroscopy with high spatial and moderate spectral resolution. In, 10th International Workshop on Greenhouse Gas Measurements from Space (IWGGMS). Noordwijk, Netherlands.

Thorpe, A.K., Frankenberg, C., Roberts, D.A., Aubrey, A.D. (2014). Mapping and quantifying methane emissions using airborne imaging spectroscopy. In, Association American Geographers Annual Meeting. Tampa, FL.

Thorpe, A.K., Frankenberg, C., Roberts, D.A. (2013). Measuring methane concentrations from anthropogenic and natural sources using airborne imaging spectroscopy. In, American Geophysical Union Fall Meeting. San Francisco, CA.

Aubrey, A.D., **Thorpe, A.K.**, Christensen, L.E., Dinardo, S., Frankenberg, C., Rahn, T.A., Manvendra, K.D. (2013). Demonstration of technologies for remote and in situ sensing of atmospheric methane abundances - A controlled release experiment. In, American Geophysical Union Fall Meeting. San Francisco, CA.

Nottrott, A.A., Rahn, T.A., Costigan, K.R., Canfield, K., Arata, C., Manvendra, K.D., Frankenberg, C., **Thorpe, A.K.**, Aubrey, A.D. (2013). Measurements and simulations of methane concentration during a controlled release experiment for top-down emission quantification by in situ and remote sensing. In, American Geophysical Union Fall Meeting. San Francisco, CA.

Dennison, P.E., **Thorpe, A.K.**, Roberts, D.A., and Parydjak, E.R. (2013). Modeling sensitivity of imaging spectrometer data to carbon dioxide and methane plumes. In, 5th Workshop on Hyperspectral Image and Signal Processing: Evolution in Remote Sensing (WHISPERS), Gainesville, FL.

Thorpe, A.K., Roberts, D.A., Bradley, E.S., Dennison, P.E. (2013). Fugitive emission mapping using airborne imaging spectrometry. In, Association American Geographers Annual Meeting. Los Angeles, CA.

Thorpe, A.K., Roberts, D.A., Dennison, P.E., Bradley, E.S., Funk, C.C. (2013). Detection of methane, carbon dioxide, and water vapor plumes using airborne imaging spectrometry: Potential for oil and gas industry. In, American Society for Photogrammetry and Remote Sensing (ASPRS) Annual Conference. Baltimore, MD.

Thorpe, A.K., Dennison, P.E., Roberts, D.A., Bradley, E.S., Funk, C.C. (2012). Airborne mapping of methane, carbon dioxide, and water vapor plumes using imaging spectrometry. In, American Geophysical Union Fall Meeting. San Francisco, CA.

Thorpe, A.K., Dennison, P.E., Roberts, D.A., Bradley, E.S., Funk, C.C. (2012). Detecting CH_4, CO_2, and N_2O plumes using the Airborne Visible/Infrared Imaging Spectrometer (AVIRIS): Complimenting satellite data and potential for HyspIRI. In, 8th International Workshop on Greenhouse Gas Measurements from Space (IWGGMS). Pasadena, CA.

Thorpe, A.K., Roberts, D.A., Dennison, P.E., Bradley, E.S., Funk, C.C. (2012). Point source emissions mapping using Airborne Visible/Infrared Imaging Spectrometer data (**invited**).

In, SPIE Defense, Security, and Sensing. Baltimore, MD.

Thorpe, A.K., Dennison, P.E., Roberts, D.A., Bradley, E.S., Funk, C.C. (2012). A remote sensing technique for mapping CH_4, N_2O, and CO_2 emissions from anthropogenic sources. In, Association American Geographers Annual Meeting. New York, NY.

Dennison, P.E., **Thorpe, A.K.**, Qi, Y., Green, R.O., Roberts, D.A., Bradley, E.S., Funk, C.C. (2012). AVIRIS and HyspIRI sensitivity to atmospheric carbon dioxide plumes. In, HyspIRI Science Workshop. Washington, D.C.

Thorpe, A.K., Roberts, D.A., Dennison, P.E., Bradley, E.S., Funk, C.C. (2011). Detection of trace gas emissions from point sources using shortwave infrared imaging spectrometry. In, American Geophysical Union Fall Meeting. San Francisco, CA.

Dennison, P.E., Qi, Y., **Thorpe, A.K.**, Pardyjak, E.R., Roberts, D.A., Funk, C.C. (2011). High spatial resolution mapping of power plant CO_2 plumes using imaging spectrometer data. In, American Geophysical Union Fall Meeting. San Francisco, CA.

Thorpe, A.K. (2011). CH_4, CO_2, and N_2O detection and quantification using airborne imaging spectrometry. In, University of California, Santa Barbara, Biogeosciences Seminar. Santa Barbara, CA.

Thorpe, A.K., Bradley, E.S., Roberts, D.A., Dennison, P.E., Funk, C.C. (2011). Using AVIRIS to map local CH_4 emissions: Potential for HyspIRI. In, HyspIRI Science Workshop. Washington, D.C.

Dennison, P.E., Qi, Y., **Thorpe, A.K.**, Pardyjak, E., Roberts, D.A., Bradley, E.S., Funk, C.C. (2011). Detection and measurement of power plant CO_2 plumes using imaging spectrometer data. In, HyspIRI Science Workshop. Washington, D.C.

Thorpe, A.K., Bradley, E.S., Funk, C., Roberts, D.A., Leifer, I., Dennison, P.E. (2011). Mapping methane from terrestrial hydrocarbon seepage using AVIRIS. In, Association of American Geographers Annual Meeting. Seattle, WA.

Thorpe, A.K., Bradley, E.S., Funk, C., Roberts, D.A., Leifer, I., Dennison, P.E., Margolis, J. (2010). Mapping methane from marine and terrestrial hydrocarbon seepage using AVIRIS. In, American Geophysical Union Fall Meeting. San Francisco, CA.

Roberts, D.A., Bradley, E.S., **Thorpe, A.K.**, Dennison, P.E., Leifer, I. (2010). Mapping methane over marine and terrestrial surfaces using imaging spectrometry. In, International Conference on Airborne Research for the Environment (ICARE). Toulouse, France.

Roberts, D.A., Bradley, E.S., **Thorpe, A.K.**, Dennison, P.E., Leifer, I. (2010). Mapping methane over marine and terrestrial surfaces using imaging spectrometry. In, Art, Science, and Applications of Reflectance Spectroscopy (ASARS). Boulder, CO.

Thorpe, A.K. (2010). Mapping methane from terrestrial hydrocarbon seepage using AVIRIS. In, University of California, Santa Barbara, Department of Geography Colloquium. Santa Barbara, CA.

Bradley, E.S., **Thorpe, A.K.**, Funk, C., Roberts, D.A., Leifer, I., Dennison, P.E., Margolis, J. (2010). Mapping methane from marine and terrestrial hydrocarbon seepage using AVIRIS.

In, HyspIRI Science Workshop. Pasadena, CA.

Teaching experience

Guest Lecturer, University of California, Santa Barbara, Santa Barbara, CA, Mar. 2015

-Lectured on imaging spectroscopy of gases for course in Advanced Optical Remote Sensing

Teaching Assistant, University of California, Santa Barbara, Santa Barbara, CA, Sept.-June 2009

-Lead laboratory sections for three courses in Ocean/Atmosphere and Physical Geography/Landsurface Geography

Academic service

-Reviewer: Nature Geoscience, Remote Sensing, Marine and Petroleum Geology

-Session chair and organizer, 2014, Measurement and modeling of environmental degradation and pollution. In, Association American Geographers Annual Meeting. Tampa, FL.

-Session presider, 2014, Remote Sensing and Image Analysis. In, Ecological Society of America Annual Meeting. Sacramento, CA.

Professional memberships

-American Geophysical Union (AGU)

-American Society for Photogrammetry and Remote Sensing (ASPRS)

-Association of American Geographers (AAG)

-Ecological Society of America (ESA)

-European Geosciences Union (EGU)

-SPIE

Geospatial, imaging, and technical experience

-Programming: IDL, MATLAB, KML, HTML, Python

-Software: ENVI/IDL, ArcGIS, MATLAB, MODTRAN 5.3, ACORN 6.0, Adobe Photoshop, Illustrator, LaTeX

Abstract

Mapping and quantifying methane emissions from local sources using airborne imaging spectrometers

by Andrew Kenji Thorpe

Most of the existing techniques for detecting, quantifying, and attributing point source emissions of methane (CH_4) have relied on ground-based measurements. These methods are limited either by their spatial resolution or temporal coverage, which makes identifying the location of individual sources challenging. By combining large image footprints and fine spatial resolution, airborne imaging spectrometers offer the potential to permit direct attribution of emissions to individual point sources.

This dissertation explores the potential of using imaging spectrometers like the Airborne Visible/Infrared Imaging Spectrometer (AVIRIS) and the next generation sensor (AVIRIS-NG) for high resolution mapping of emissions and quantification of CH_4 concentrations present within scenes. To do so, non-quantitative filtering methods and quantitative CH_4 retrievals were adapted for use with AVIRIS and AVIRIS-NG scenes over both marine and terrestrial environments. These techniques were applied to scenes acquired at natural marine CH_4 seeps (Coal Oil Point, COP) and for natural and anthropogenic sources in the Los Angeles Basin. At these locations, distinct plumes consistent with local wind direction were observed. As part of this study, I developed methods of reducing noise and false positives in results.

As part of a controlled release experiment, AVIRIS-NG was flown at multiple flight altitudes and CH_4 flux rates to determine its sensitivity for CH_4 detection. From these results, detection rates were calculated for multiple flux rates and indicate a detection threshold around 3.4 m^3/h (0.02 kt/year). Given this threshold, AVIRIS-NG has the potential to detect a number of fugitive CH_4 source categories for natural gas fields. Ongoing analysis of AVIRIS-NG scenes over oil and gas fields indicates multiple CH_4 plumes, further emphasizing the utility of imaging spectrometers for direct attribution of CH_4 emissions.

Contents

Front matter **i**

Abstract xii

1 Introduction **1**

1.1 Motivation and summary of chapters 1

1.2 Atmospheric methane 3

1.3 Geological methane seeps 5

1.4 Methane in the Los Angeles Basin 7

1.5 Fugitive methane emissions 8

1.6 Monitoring methane concentrations from space 9

1.7 Measuring methane on local scales 10

1.8 Absorption spectroscopy in the shortwave infrared 12

1.9 AVIRIS and AVIRIS-NG imaging spectrometers 14

2 High resolution mapping of methane emissions from marine and terrestrial sources using a Cluster-Tuned Matched Filter technique and imaging spectrometry **18**

2.1 Abstract 19

2.2 Introduction 19

2.3 Methods 25

2.3.1 Study sites 25

2.3.2 AVIRIS data 27

2.3.3 Cluster-Tuned Matched Filter 28

2.3.4 Input parameters for Cluster-Tuned Matched Filter 36

2.3.5 Segmentation and classification 37

2.4 Results 38

2.4.1 Cluster-Tuned Matched Filter 38

2.4.2 Noise and false positives . . . 46
2.4.3 Segmentation and classification . . . 47
2.5 Discussion . . . 53
2.6 Conclusions . . . 57
2.7 Acknowledgments . . . 58

3 Retrieval techniques for airborne imaging of methane concentrations using high spatial and moderate spectral resolution: Application to AVIRIS 59
3.1 Abstract . . . 60
3.2 Introduction . . . 61
3.3 Airborne measurements of methane . . . 62
3.4 Basic principles of IMAP-DOAS . . . 64
3.5 Study sites and AVIRIS data . . . 69
3.6 IMAP-DOAS retrieval method . . . 69
3.6.1 IMAP-DOAS input parameters . . . 70
3.6.2 Forward model and optimal estimation . . . 72
3.7 Basic principles of SVD . . . 75
3.8 SVD retrieval method . . . 76
3.9 Results for IMAP-DOAS sensitivity study . . . 79
3.10 Results for IMAP-DOAS . . . 80
3.10.1 COP . . . 80
3.10.2 Inglewood . . . 83
3.11 Results for SVD . . . 85
3.11.1 COP . . . 85
3.11.2 Inglewood . . . 87
3.12 Discussion . . . 90
3.12.1 Comparison of retrieval results . . . 90
3.12.2 Potential for AVIRIS-NG and future sensors . . . 95
3.13 Conclusions . . . 97
3.14 Acknowledgments . . . 98

4 Mapping methane concentrations from a controlled release experiment using the next generation Airborne Visible/Infrared Imaging Spectrometer (AVIRIS-NG) 100

4.1 Abstract . . . 101

4.2 Introduction . . . 101

4.3 Controlled release experiment . . . 104

4.4 AVIRIS-NG instrument and data processing . . . 107

4.5 Hybrid IMAP/SVD methane retrieval . . . 108

4.6 Matched filter detection . . . 113

4.7 Results . . . 115

4.7.1 Multiple fluxes and flight altitude examples . . . 115

4.7.2 Residual and radiance analysis . . . 118

4.7.3 Summary of all results . . . 121

4.8 Discussion and conclusion . . . 125

4.9 Acknowledgments . . . 129

5 Conclusions 130

5.1 Summary of research . . . 130

5.2 Potential application . . . 134

5.3 Ongoing research and future directions . . . 138

A Appendix: Point source emissions mapping using the Airborne Visible/Infrared Imaging Spectrometer (AVIRIS) 142

A.1 Abstract . . . 143

A.2 Introduction . . . 144

A.3 Methodology . . . 146

A.3.1 AVIRIS data and Modtran radiative transfer model . . . 146

A.3.2 Study sites . . . 148

A.3.3 Cluster-Tuned Matched Filter algorithm . . . 148

A.4 Initial results and discussion . . . 150

A.5 Conclusions . . . 154

References **156**

Chapter 1

Introduction

1.1 Motivation and summary of chapters

Methane (CH_4) is a long-lived greenhouse gas that contributes approximately one third the radiative forcing of carbon dioxide (CO_2) (Butler 2012). CH_4 concentrations are currently increasing (Nisbet et al. 2014), there is considerable uncertainty in the global CH_4 budget (Kirschke et al. 2013), and emission estimates for individual source categories can vary by as much as a factor of two (Dlugokencky et al. 2011).

Existing spaceborne spectrometers provide an effective means of detecting continental scale variation in CH_4 concentrations, however, they lack the fine spatial resolution needed to detect near-surface emissions. In contrast, local emission monitoring often relies upon ground-based measurements at fixed sites with limited spatial coverage. By combining large image footprints and fine spatial resolution, airborne imaging spectrometers offer the potential to permit direct attribution of emissions to individual point sources.

This dissertation explores the use of imaging spectrometers like the Airborne Visible/Infrared Imaging Spectrometer (AVIRIS) and the next generation sensor (AVIRIS-NG) for high resolution mapping of emissions and quantification of CH_4 concentrations present

within scenes. In addition, I examine the CH_4 sensitivity of the AVIRIS-NG instrument and the possibility of using CH_4 retrievals to place constraints on emission fluxes.

In Chapter 2, I use AVIRIS data and the non-quantitative Cluster-Tuned Matched Filter (CTMF) (Funk et al. 2001) for high resolution mapping of CH_4 anomalies from marine and terrestrial sources. Distinct plumes consistent with local wind direction were observed for the Coal Oil Point (COP) marine seep field and downwind of hydrocarbon storage tanks at the Inglewood Oilfield in Los Angeles, CA. As part of this study, I develop a method of reducing noise and false positives based on segmentation of CTMF results and the spectral properties of the underlying surface over the full spectral range measured by AVIRIS.

I focus on quantification of CH_4 concentrations and uncertainty estimation in Chapter 3 by adapting an iterative maximum a posteriori differential optical absorption spectroscopy (IMAP-DOAS) (Frankenberg et al. 2005) algorithm for use with AVIRIS. In addition, I develop a hybrid approach using Singular Value Decomposition (SVD) and IMAP-DOAS as a complementary method of quantifying gas concentrations within complex AVIRIS scenes. I use the same study sites to test both algorithms and perform a sensitivity study to estimate the precision error of the IMAP-DOAS retrieval algorithm and the expected CH_4 sensitivities of AVIRIS and AVIRIS-NG.

Chapter 4 builds upon the previous research to better understand the ability of AVIRIS-NG to detect and quantify CH_4 emissions using a controlled CH_4 release experiment with AVIRIS-NG overflights. This study determines which flux rates can be observed using both the non-quantitative CTMF algorithm and the quantitative hybrid retrieval using IMAP-DOAS and SVD. In some cases plumes were detected as low as 3.40 m^3/h (0.02 kt/year), indicating that

AVIRIS-NG has the capability of detecting a number of fugitive CH_4 source categories for natural gas fields.

Finally, additional material is provided in the appendix showing the potential for detecting carbon dioxide (CO_2) and nitrous oxide (N_2O) using AVIRIS-like sensors. Gas anomalies were observed at a natural gas-fired power plant (CO_2), flaring stack (CH_4), and at the Hyperion wastewater treatment facility in Los Angeles, CA (N_2O and CH_4).

1.2 Atmospheric methane

Atmospheric CH_4 absorbs incoming shortwave solar radiation and causes greenhouse warming by absorbing outwelling longwave radiation from the Earth. The contribution of CH_4 to the global energy budget is often quantified using the concept of radiative forcing, the change in energy flux (watts per square meter, W m^{-2}) over the period from the start of the industrial era (about 1750) to present (IPCC 2013). The direct radiative forcing of CH_4 from 1750 to 2011 is estimated to be 0.48 W m^{-2} (Myhre et al. 2013). However, CH_4 causes an additional 0.51 W m^{-2} of indirect radiative forcing through the formation of absorbing gasses like water vapor (H_2O) and ozone (O_3), and increased warming as a result of reductions in hydroxol radicals (OH) that decreases sulfate aerosol production (Shindell et al. 2009). This results in a total radiative forcing for direct and indirect effects of 0.99 W m^{-2} compared with to 1.6 W m^{-2} for CO_2 (Shindell et al. 2009). In addition, CH_4 is more effective than CO_2 at trapping radiant energy on a molecular basis and has a global warming potential 86 times that of CO_2 for a 20 year time interval (Myhre et al. 2013).

In the Archean (4.0-2.5 billion years ago), atmospheric CH_4 originated from methanogens, anaerobic bacteria that generate CH_4 as a metabolic byproduct. Methanogens present in wet-

lands and oceans have remained an important contributor to atmospheric CH_4 in addition to termites, wild ruminants, and geological seeps. Prior to the start of the industrial era, sources of CH_4 resulting from human activity included domestic ruminants, rice agriculture, and biomass burning. At present, approximately 90% of CH_4 destruction is due to OH oxidation (Lelieveld et al. 1993), while additional CH_4 sinks include loss to the stratosphere, and consumption by methanotrophs in soils (Lelieveld et al. 1998).

In the late preindustrial Holocene (1000 to 1800 A.D.), mean atmospheric CH_4 concentrations were 695 ppb (Etheridge et al. 1998) and global concentrations have increased to around 1,847 ppb in 2014 (NOAA 2015). The growth rate of global atmospheric CH_4 concentrations slowed between 1999 and 2006, but has increased since 2007 (Nisbet et al. 2014). While anthropogenic sources made up an estimated 4 to 34% of pre-industrial emissions (IPCC 2007; Houweling et al. 2000), between 50 and 65% of the global CH_4 budget can be attributed to anthopogenic emissions (Ciais et al. 2013).

Ice core records have indicated CH_4 concentrations are closely tied to atmospheric temperature records, while present-day concentrations have not been observed in the previous 420,000 years (Wuebbles and Hayhoe 2002). Therefore, there is concern that increased surface and ocean temperatures associated with global warming may increase CH_4 emissions from wetlands (Shindell et al. 2004), melting permafrost (Woodwell et al. 1998) and CH_4 hydrate destabilization (Kvenvolden 1988).

The global CH_4 budget is relatively well constrained and top-down inversion of atmospheric measurements from surface stations estimate total global CH_4 emissions of 553 Tg CH_4 yr^{-1} (range of 526 to 569 Tg CH_4 yr^{-1}) and total loss of 550 Tg CH_4 yr^{-1} (range of 514 to

560 Tg CH_4 yr^{-1}) (Ciais et al. 2013). This results in a 3 Tg CH_4 yr^{-1} net imbalance consistent with the observed increase in the atmospheric CH_4 growth rate for the 2000s (Ciais et al. 2013). However, considerable uncertainty remains regarding partitioning between individual natural and anthropogenic source types and locations.

The single most important natural CH_4 source is wetlands, estimated at 175 Tg CH_4 yr^{-1} (range of 142 to 208 Tg CH_4 yr^{-1}) and accounting for 80% of total natural emissions (218 Tg CH_4 yr^{-1}, range of 179 to 273 Tg CH_4 yr^{-1}) (Ciais et al. 2013). There is a 50% uncertainty associated with wetlands while smaller natural sources can have uncertainties around 100% (Kirschke et al. 2013). Between 50 and 65% of the global CH_4 budget can be attributed to anthropogenic emissions (335 Tg CH_4 yr^{-1}, range of 273 to 409 Tg CH_4 yr^{-1}) (Ciais et al., 2013). Globally, uncertainties associated with anthropogenic emissions are around 30% for both agriculture/waste and fossil-fuel emission categories and fall to 20% for biomass burning (Kirschke et al. 2013). In the United States, major anthropogenic CH_4 sources listed by importance include livestock (enteric fermentation and manure management), natural gas (production, transmission, and storage), landfills, and wastewater treatment (EPA 2013).

1.3 Geological methane seeps

After wetlands, geological CH_4 seeps are the next largest natural emission source, estimated to contribute about 40 Tg CH_4 yr^{-1} for marine seepage (Kvenvolden and Rogers 2005) and between 20 to 40 Tg CH_4 yr^{-1} for terrestrial environments (Etiope et al. 2009). Study sites for Chapters 2 and 3 include marine CH_4 seeps at Coal Oil Point (COP) and terrestrial seepage in the Los Angeles Basin.

Active for over 500,000 years (Boles et al. 2001), the COP seep field is one of the largest

and best studied sources of natural CH_4 emissions and oil seepage. Located in the Santa Barbara Channel offshore of the University of California, Santa Barbara, COP is made up of a number of individual seep locations that are influenced by subsurface geology (Leifer et al. 2010) and include the Trilogy Seep, Horseshoe Seep, and IV Super Seep. Bubble diameters range between 200 and 104 μm (Leifer et al. 2006a) and CH_4 fractions vary between 50 and 70% at the surface (Clark et al. 2010). Total atmospheric CH_4 emissions for COP are estimated at 100,000 m^3/day over an area of 20 km^2 at the surface (Hornafius et al. 1999). The spatial distribution of the seep expression at the surface can change considerably (Clark et al. 2010) and flux rates from individual seep locations can also vary (Leifer et al. 2006b; Boles et al. 2001).

Located approximately 8 to 12 km west of downtown Los Angeles, the Mid-Wilshire and Inglewood neighborhoods have significant oil and CH_4 seepage. This is most clearly illustrated by the hydrocarbon and water mixture with visible CH_4 bubbles present at the La Brea Tar Pits. In the surrounding areas, CH_4 gas can often be seen bubbling from between cracks in paved surfaces after rains (Gurevich et al. 1993). Following the 1985 Ross Department Store explosion caused by natural CH_4 buildup, the city of Los Angeles designated a Methane Zone and Methane Buffer Zone with additional building codes requiring CH_4 mitigation such as gas detectors in addition to active and passive venting systems (Chilingar and Endres 2005). CH_4 seepage in the Mid-Wilshire and Inglewood regions is poorly constrained and a recent study suggests these emissions are considerable (Farrell et al. 2013).

1.4 Methane in the Los Angeles Basin

In many regions of the Los Angeles Basin, CH_4 concentrations are significantly above the average global concentrations of 1.85 ppm in 2014 (NOAA 2015). For example, data from four monitoring stations averaged over 1994 and 1995 indicate elevated levels of CH_4, between 1.91 to 2.10 ppm (Dwight Oda, California Air Resources Board, personal communication, 2010) and in 2008 concentrations were reported between 1.76 to 2.16 ppm (Hsu et al. 2010). Diurnal variation in CH_4 concentrations has been measured and can result from transport of CH_4 enhanced air from Los Angeles to other regions of the South Coast Air Basin (Wunch et al. 2009).

In addition to the natural CH_4 seepage, the Los Angeles Basin has additional emission sources, including landfills, livestock, wastewater treatment, as well as petroleum and natural gas production, transmission, and storage (Wennberg et al. 2012). The urban Los Angeles Basin contains over seventy oil fields (Chilingar and Endres 2005) with over 21,000 inactive or active oil and natural gas wells in Los Angeles county alone (DOGGR 2010a). Many of these wells were drilled decades ago and subsequently abandoned with well documented CH_4 leaks that primarily result from improperly sealed wells. For the Salt Lake Oil Field alone, there are an estimated 528 improperly sealed wells (Pipkin and Proctor 1992). At the Inglewood Oil Field, there is active hydrocarbon extraction, producing approximately 3.1 million barrels of oil (bbl) and 1.5 billion cubic feet (Bcf) of natural gas in 2008 (DOGGR 2010b).

In the Los Angeles Basin, CH_4 emissions appear underestimated (Wunch et al. 2009) and unaccounted sources appear to be anthropogenic and natural CH_4 emissions (Wennberg et al. 2012). Stable isotope analysis suggests elevated levels of CH_4 in the Los Angeles area

result primarily from non-biogenic sources such as hydrocarbon refining and gas pipelines (Townsend-Small et al. 2012). Given this uncertainty, there have been a number of studies trying to better attribute CH_4 emissions in the Los Angeles Basin including in situ measurement using driving surveys (Farrell et al. 2013) and airborne campaigns (Wennberg et al. 2012; Peischl et al. 2013). Additional studies for measuring CH_4 concentrations in Los Angeles include a Fourier transform spectrometer at Mount Wilson that measures reflected sunlight in the near infrared (Fu et al. 2014) and a suite of instruments as part of the Megacities Carbon Project (JPL 2014).

1.5 Fugitive methane emissions

CH_4 leaks that occur during the extraction, treatment, transport, and use of fossil fuels are collectively termed fugitive CH_4 emissions. These emissions can result over the lifetime of oil and gas wells, including during well completion, operation (Allen et al. 2013), and from abandoned wells that are improperly sealed (Chilingar and Endres 2005). After hydrocarbons are extracted, CH_4 can be vented and flared at equipment present at oil fields or refineries, including those used for liquid unloading, storage of oil and condensate, and dehydration of natural gas (GAO 2010). Fugitive CH_4 can also occur from hydrocarbon storage tanks (EPA 2013) and there has been increased concern of these emissions from leaking natural gas pipelines (Murdock et al. 2008) and hydraulic fracturing (Howarth et al. 2011).

Global fugitive CH_4 emissions from natural gas and oil systems are estimated between 105.00 Tg CH_4 yr^{-1} (Ciais et al. 2013) and 64.50 Tg CH_4 yr^{-1} (1,354.42 MMT CO_2 E yr^{-1}) and are expected to increase 35% by 2020 based on 2010 levels (EPA 2006a). Numerous studies suggest bottom-up inventories for fugitive CH_4 from natural gas production and distribution

are underestimated (Kort et al. 2008; Brandt et al. 2014; Miller et al. 2013). Multiple top-down estimates suggest fugitive CH_4 emissions from natural gas and oil production can be large, ranging between 2.3 to 7.0% of CH_4 produced annually for the Denver-Julesburg Basin, Colorado (Petron et al. 2012) and between 6.2 to 11.7% of average hourly natural gas production in the Uintah County oil and gas field (Karion et al. 2013). These estimates pertain to specific locations/times and leak rates from different facilities should vary considerably. For example, additional studies suggest that fugitive CH_4 leakage is considerably lower (Alvarez et al. 2012; Allen et al. 2013; O'Sullivan and Paltsev 2012).

1.6 Monitoring methane concentrations from space

Global CH_4 concentrations are well constrained due to existing spaceborne remote sensing that provides an effective means of detecting continental scale variation in CH_4 concentrations. Satellite sensors like the Infrared Atmospheric Sounding Interferometer (IASI) (Aires et al. 2002), the Tropospheric Emission Spectrometer (TES) (Beer et al. 2001), and the Atmospheric Infrared Sounder (AIRS) (Tobin et al. 2006) utilize strong rotational-vibrational transitions causing absorption in the mid-infrared (MIR) and thermal-infrared (TIR) to measure column averaged CH_4 concentrations across much of the globe. However, current sensors do not provide near-surface concentrations given detection in the TIR requires a strong thermal contrast between ground and lower atmosphere and is limited by sensor saturation due to a high CH_4 absorption coefficient.

CH_4 also has absorptions in the shortwave infrared (SWIR) between 1,400 and 2,500 nm, which permitted global CH_4 mapping by the Scanning Imaging Absorption Spectrometer for Atmospheric Chartography (SCIAMACHY) onboard the Envisat satellite. This grating spec-

trometer has eight channels operating from 240 to 2,400 nm with a spectral resolution between 0.2 to 1.4 nm and spatial resolution ranging from 30 × 60 km to 30 × 240 km (Buchwitz et al. 2005a). The Weighting Function Modified Differential Optical Absorption Spectroscopy (WFM-DOAS) retrieval algorithm (Buchwitz et al. 2000) was applied to 2003 data from SCIAMACHY channels 4, 6, and 8 to estimate column amounts of CO (carbon monoxide), CO_2, and CH_4 (Buchwitz et al. 2005b). Frankenberg et al. (2005b) developed an iterative maximum a posteriori-DOAS (IMAP-DOAS) algorithm using DOAS and the linear relationship between vertical column-densities for CO_2 and CH_4 to estimate global CH_4 column-averaged mixing ratios over terrestrial surfaces and detect regions with high column averages, including the Red Basin in China and the Sudd wetlands of southern Sudan (Frankenberg et al. 2011). More recently, CH_4 enhancements were also observed using SCIAMACHY for the Four Corners region of northern New Mexico, a region with extraction of coalbed CH_4 (Kort et al. 2014). While the Envisat satellite mission ended in 2012, the Greenhouse Gas Observing Satellite (GOSAT) (Saitoh et al. 2009) continues to provide global CH_4 mapping in good agreement with ground based measurements (Butz et al. 2011) and results from global 3-D chemical transport models (Parker et al. 2011).

1.7 Measuring methane on local scales

While spaceborne sensors lack the fine spatial resolution needed to detect near-surface CH_4, local measurement of CH_4 concentrations typically relies upon ground-based measurements with limited spatial coverage, such as gas chromatography (Leifer et al. 2013), cavity ring down spectroscopy (Farrell et al. 2013), tunable diode lasers (Hsu et al. 2010), or Fourier transform spectrometers at fixed sites (Wunch et al. 2009; Fu et al. 2014). Many of these

instruments can be used to estimate CH_4 emission flux rates of individual point sources or for local regions using the eddy covariance technique applied to micrometeorological measurements (Eugster and Pluss 2010), atmospheric tracers (Lamb et al. 1995), and mass balance approaches (Cambaliza et al. 2013).

Aircraft measurements of CH_4 concentrations are useful because they offer the potential to measure local/regional variations in gas concentrations and complement ongoing efforts at coarser spatial resolutions, such as spaceborne sensors. Research and commercial aircraft equipped with in situ gas measurement provides some sense of CH_4 variability at local and regional scales (ARCTAS 2010; Schuck et al. 2012). The nadir-viewing Fourier transform spectrometer included as part of the Carbon in Arctic Reservoirs Vulnerability Experiment (CARVE) (Miller and Dinardo 2012) and spectrometers like MAMAP (Methane Airborne MAPper) (Gerilowski et al. 2011) also permit measuring CH_4 concentrations on local scales.

Airborne measurements are increasingly being used to study fugitive CH_4 emissions from the oil and gas industry. This includes in situ CH_4 measurement by aircraft using mass balance approaches (Karion et al. 2013), ethane (C_2H_6) to CH_4 enhancement ratios (Wennberg et al. 2012), and observations of alkanes used with high-resolution atmospheric transport models (Miller et al. 2013). The airborne spectrometer MAMAP measured elevated CH_4 concentrations from coal mine ventilation shafts near Ibbenbüren, Germany and permitted an inversion estimate in good agreement with reported emissions rates from mine operators (Krings et al. 2013). However, MAMAP is a non-imaging spectrometer with a small field of view (FOV) limited to flying transects across local gas plumes rather than mapping plumes in their entirety.

1.8 Absorption spectroscopy in the shortwave infrared

In the SWIR, absorptions of reflected solar radiance can be described using the Lambert-Beer law that describes the relationship between incident intensity for the vertical column ($I_0(v)$) and measured intensity ($I(v)$) after passing through a light path (ds) containing multiple absorbers:

$$I(v) = I_0(v) \cdot \exp\left(-\int \sigma(v,p,T)\, c(s)\, \mathrm{d}s\right) \tag{1.1}$$

Each absorber has an associated absorption cross section (σ) and number concentration of the absorber ($c(s)$, molecules m^{-3}). Eq. 1.1 is wavelength dependent and the absorption cross section varies with temperature (T) and pressure (p). If the atmospheric absorption features are fully resolved by the instrument and only weak absorbers are present, Eq. 1.1 can be linearized with respect to slant column density S:

$$\begin{aligned} \boldsymbol{\tau} &= \ln\left(\frac{I_0(v)}{I(v)}\right) \approx \sigma\left(v,\bar{p},\bar{T}\right) \cdot \int c(s)\, \mathrm{d}s \\ &= \sigma(v,p,T) \cdot S \end{aligned} \tag{1.2}$$

where measured optical density ($\boldsymbol{\tau}$) is proportional to the product of the absorption cross section and the retrieved S, the path integral of the concentration of the absorber along the light path. S is related to the vertical column density (V), the integral of the concentration along the vertical from the surface to the top of atmosphere, by way of the air mass factor (A), where $A = S/V$. In the SWIR, scattering in the atmosphere is generally low (Buchwitz and Burrows 2003, Dufour and Breon 2003) and for AVIRIS and AVIRIS-NG, the impact of scattering is far lower than the retrieval precision error. Thus, it can be neglected and $A = 1/\cos(\mathrm{SZA}) + 1/\cos(\mathrm{LZA})$, where SZA is the solar zenith angle and LZA is the line-of-sight

zenith angle.

In the SWIR, retrieval algorithms for absorbing species require radiative transfer modeling of solar radiation along the light path from the sun to the sensor. They permit comparison of simulated at sensor radiance with a known abundance of absorbers with measured radiance provided by the sensor. Differential optical absorption spectroscopy (DOAS) (Platt 1994) is one approach that has been used for a number of applications, including ground-based (Stutz et al. 2010), satellite (Schneising et al. 2012), and airborne measurement (Gerilowski et al. 2011). The underlying principle of DOAS is to isolate higher frequency features resulting from gas absorptions from lower frequency surface reflectance features (Bovensmann et al. 2011). A related technique, iterative maximum a posteriori differential optical absorption spectroscopy (IMAP-DOAS) (Frankenberg et al. 2005b), uses optimal estimation theory to adjust the slant column densities of multiple gasses until total optical density fits the observed measurement. This technique will be explained in greater detail in Chapters 3 and 4, where it is applied to data from the airborne imaging spectrometers AVIRIS and AVIRIS-NG to quantify CH_4 enhancements.

The atmospheric radiative transfer model Modtran (Berk et al. 1989) can simulate radiances in addition to the spectral transmittance, the ratio between measured intensity ($I(v)$ and ($I_0(v)$, Eq. 1.1). In Fig. 1.1a Modtran transmittance is shown for weaker CH_4 absorption features around 1,667 nm and stronger absorptions between 2,100 and 2,500 nm. In this region, water vapor (H_2O) has considerable spectral overlap with CH_4, particularly beyond 2,300 nm, which complicates CH_4 detection (Fig. 1.1b).

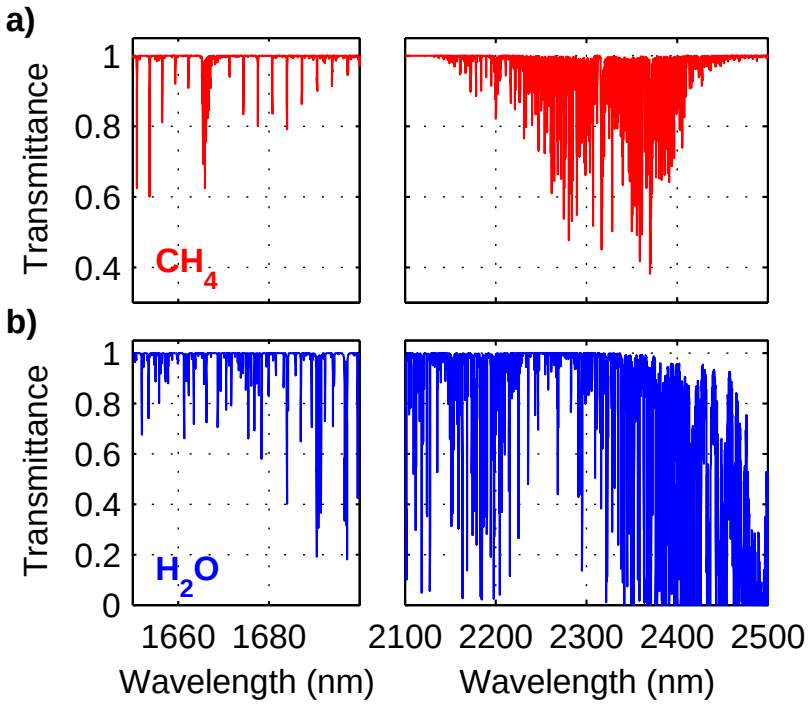

Figure 1.1. (a) High resolution CH_4 transmittance for two spectral regions, from 1,650 to 1,700 nm and between 2,100 and 2,500 nm. (b) High resolution H_2O transmittance for the same wavelengths. Transmittance spectra were calculated using the radiative transfer model Modtran 5.3 (Berk et al. 1989) parameterized for a mid-latitude summer model atmosphere and nadir-looking sensor at 8.9 km altitude.

1.9 AVIRIS and AVIRIS-NG imaging spectrometers

The Airborne Visible/Infrared Imaging Spectrometer (AVIRIS) is a whisk broom sensor with a 34° FOV and measures reflected solar radiance at the nadir viewing geometry across 224 channels between 350 and 2,500 nm with a 10 nm spectral resolution and full width at half maximum (FWHM) (Green et al. 1998). Historically it has been used to map mineralogical, biochemical, and biophysical properties of soils, rocks, and plants (Green et al., 1998). However, the high signal-to-noise ratio of AVIRIS and strong CH_4 absorption features present between 2,000 and 2,500 nm have permitted mapping of concentrated gas plumes in marine environments using AVIRIS. For bright sun-glint scenes at the Coal Oil Point (COP) marine

seep field in the Santa Barbara Channel, California, Roberts et al. (2010) developed a spectral residual approach between 2,000 and 2,500 nm and Bradley et al. (2011) a band ratio technique using the 2,298 nm CH_4 absorption band and the 2,058 nm CO_2 absorption band. These techniques are not suited for terrestrial locations that have lower albedos and are not spectrally flat in the SWIR.

The next generation Airborne Visible/Infrared Imaging Spectrometer (AVIRIS-NG) has a 36° FOV with 427 spectral channels between 380 and 2,510 nm at a 5 nm spectral resolution and 6 nm FWHM (Hamlin et al. 2011). This pushbroom instrument is similar to the visible-to-shortwave infrared (VSWIR) imaging spectrometer used in the Carnegie Airborne Observatory next generation Airborne Taxonomic Mapping Systems (AToMS) (Asner et al. 2012). In addition, similar spectrometers are being used in the Airborne Observation Platform (AOP) by the National Ecological Observatory Network (NEON) (Kampe et al. 2010).

For both AVIRIS and AVIRIS-NG, the spatial resolution for each image pixel depends on the altitude of the flights. For AVIRIS-NG, typical spatial resolutions range between 0.4 m per pixel for a flight at 0.43 km above ground level (AGL) (image swath width 0.28 km) to 3.6 m per pixel for 3.8 km AGL (image swath of 2.47 km). By combining large image footprints and fine spatial resolution, airborne imaging spectrometers are well suited for mapping local CH_4 plumes. However, AVIRIS and AVIRIS-NG were not designed for CH_4 detection, providing high spatial resolution and limited spectral resolution that reduces CH_4 sensitivity. A comparison of the AVIRIS and AVIRIS-NG instrument parameters is provided in Table 1.1.

AVIRIS and AVIRIS-NG cannot fully resolve the individual CH_4 absorption lines shown in Fig. 1.1a and must convolve light using an instrument lineshape (ILS) function wider than

Category	Parameter	AVIRIS	AVIRIS-NG
Spectral	Range	380 to 2500 nm	380 to 2510 nm
	Spectral resolution	10 nm	5 nm
	Response	1 to 1.5× sampling	1 to 1.5× sampling
	Calibration	±0.1 nm	±0.1 nm
Radiometric	Range	0 to max Lambertian	0 to max Lambertian
	Precision (SNR)	>1000 @ 600 nm	>2000 @ 600 nm
	Precision (SNR)	>400 @ 2200 nm	>1000 @ 2200 nm
	Accuracy	90% (10% uncertainty)	95% (10% uncertainty)
	Linearity	≥9% characterization	≥9% characterization
Spatial	Range	34° FOV	36° FOV
	Sampling	1 milliradian	1 milliradian
	Response	1 to 1.5× sampling	1 to 1.5× sampling
	Spatial resolution	4 to 20 m	0.3 to 20 m
	Geometric model	Full 3 axes cosines	Full 3 axes cosines
Uniformity	Spectral cross-track	>98% across FOV	>95% across FOV
	Spectral-IFOV-variation	>98% spectral direction	>95% spectral direction

Table 1.1. AVIRIS and AVIRIS-NG sensor characteristics (Robert Green, Jet Propulsion Laboratory, personal communication, 2014).

individual absorption lines. As a result, CH_4 sensitivity is reduced compared to instruments with finer spectral resolutions. The high resolution transmittance from Fig. 1.1a is convolved using the ILS functions of AVIRIS and AVIRIS-NGand is shown in Fig. 1.2a for CH_4. While CH_4 absorption features are weak at 1,667 nm, reflected radiances are generally higher at

shorter wavelengths, compared to the lower radiances present for the strong absorptions between 2,250 and 2,400 nm. Convolved H_2O transmittance has been included in Fig. 1.2b indicating spectral overlap with CH_4.

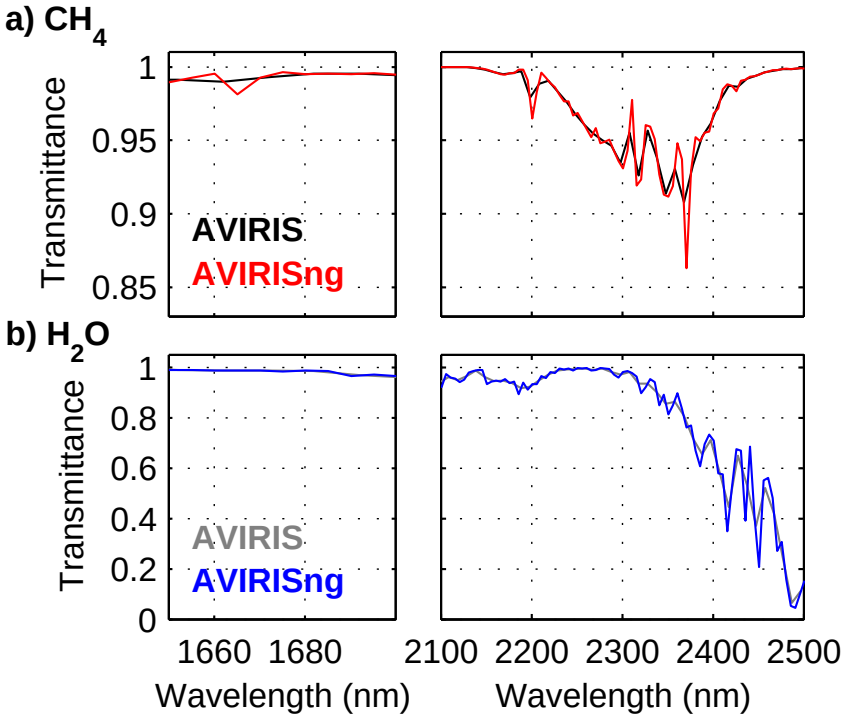

Figure 1.2. (a) CH_4 transmittance for two spectral regions, from 1,650 to 1,700 nm and between 2,100 and 2,500 nm convolved to AVIRIS and AVIRIS-NG spectral resolution (10 and 5 nm respectively). (b) H_2O transmittance for the same wavelengths convolved to AVIRIS and AVIRIS-NG spectral resolution. Transmittance spectra were calculated using the radiative transfer model Modtran 5.3 (Berk et al. 1989), parameterized for a mid-latitude summer model atmosphere and nadir-looking sensor at 8.9 km altitude.

Chapter 2

High resolution mapping of methane emissions from marine and terrestrial sources using a Cluster-Tuned Matched Filter technique and imaging spectrometry

A. K. Thorpe[1], D. A. Roberts[1], E.S. Bradley[1], C. C. Funk[1,2], P.E. Dennison[3], I. Leifer[4]

[1]Department of Geography, University of California, Santa Barbara, Santa Barbara, CA

[2]U.S. Geological Survey, Department of Geography, University of California, Santa Barbara, CA

[3]Department of Geography, University of Utah, Salt Lake City, UT

[4]Marine Science Institute, University of California, Santa Barbara, Santa Barbara, CA

This chapter was published in Remote Sensing of Environment and is referenced as Thorpe et al. (2013).

2.1 Abstract

In this study, a Cluster-Tuned Matched Filter (CTMF) technique was applied to data acquired by the Airborne Visible/Infrared Imaging Spectrometer (AVIRIS) over marine and terrestrial locations known to emit methane (CH_4). At the Coal Oil Point marine seep field, prominent CH_4 anomalies were consistent with advection from known areas of active seepage. For a region with natural CH_4 and oil seepage located west of downtown Los Angeles, significant CH_4 anomalies were identified for known sources at the La Brea Tar Pits and in close proximity to probable sources, including an office complex documented as venting CH_4 continuously and hydrocarbon storage tanks on the Inglewood Oil Field. However, interpretation of anomalies was complicated by noise and false positives for surfaces with strong absorptions at the same wavelengths as CH_4 absorption features. Segmentation of results identified 16 distinct locations of contiguous pixels with high CTMF scores and segments were classified into probable CH_4 anomalies and confusers based on the spectral properties of the underlying surface over the full spectral range measured by AVIRIS. This technique is particularly well suited for application over large areas to detect CH_4 emissions from concentrated point sources and should permit detection of additional trace gasses with distinct absorption features, including carbon dioxide (CO_2) and nitrous oxide (N_2O). Thus, imaging spectrometry by an AVIRIS-like sensor has the potential to improve high resolution greenhouse gas mapping, better constraining local sources.

2.2 Introduction

Methane (CH_4) is a long-lived greenhouse gas with an average atmospheric residence of approximately 7.9 years (Lelieveld et al. 1998). One molecule of CH_4 is 72 times more effective

at trapping radiant energy than a molecule of carbon dioxide (CO_2) on a 20 year time scale (IPCC 2007). Global atmospheric CH_4 has more than doubled in the last two centuries with an annual growth rate that has been highly variable since the 1990s with renewed growth starting in 2007 (Dlugokencky et al. 2009) and average concentrations exceeding 1.8 ppm in 2012 (NOAA 2012).

Emission sources and sinks exhibit high spatial heterogeneity and large-scale interannual variability (Bousquet et al. 2006) and estimates for total sources of atmospheric CH_4 have considerable uncertainty, ranging between 500 and 600 Tg yr^{-1} (IPCC 2007). Between 60 and 70% of CH_4 emissions are presently anthropogenic (Lelieveld et al. 1998) and include emissions from domestic ruminants, rice agriculture, waste handling, and fossil fuel production. Wetlands, termites, and geological seeps are significant natural sources (Etiope et al. 2009), while major CH_4 sinks include oxidization by the hydroxyl radical (OH), loss to the stratosphere, and consumption by methanotrophs in soils (Lelieveld et al. 1998). Approximately 90% of CH_4 destruction is due to OH oxidation (Lelieveld et al. 1993), however, CH_4 destruction is minimal on the time scale of minutes to hours relevant to studying local emissions nearby the source.

On global scales, partitioning between natural and anthropogenic CH_4 sources remains uncertain and emission estimates for individual source categories can vary by as much as a factor of two (Dlugokencky et al. 2011). On regional scales, uncertainties for anthropogenic CH_4 emissions are considerable, between 9 and 17% in the United States (EPA 2011b) and 19 and 36% for a number of countries in northwest Europe (Bergamaschi et al. 2010).

CH_4 has strong rotational-vibrational transitions causing absorption in the mid-infrared

(MIR) and thermal-infrared (TIR), permitting detection by satellite sensors like the Infrared Atmospheric Sounding Interferometer (IASI) (Aires et al. 2002), the Tropospheric Emission Spectrometer (TES) (Beer et al. 2001), and the Atmospheric Infrared Sounder (AIRS) (Tobin et al. 2006). Because detection in the TIR requires a strong thermal contrast between ground and lower atmosphere and is limited by sensor saturation due to a high CH_4 absorption coefficient, current sensors cannot provide near-surface concentrations.

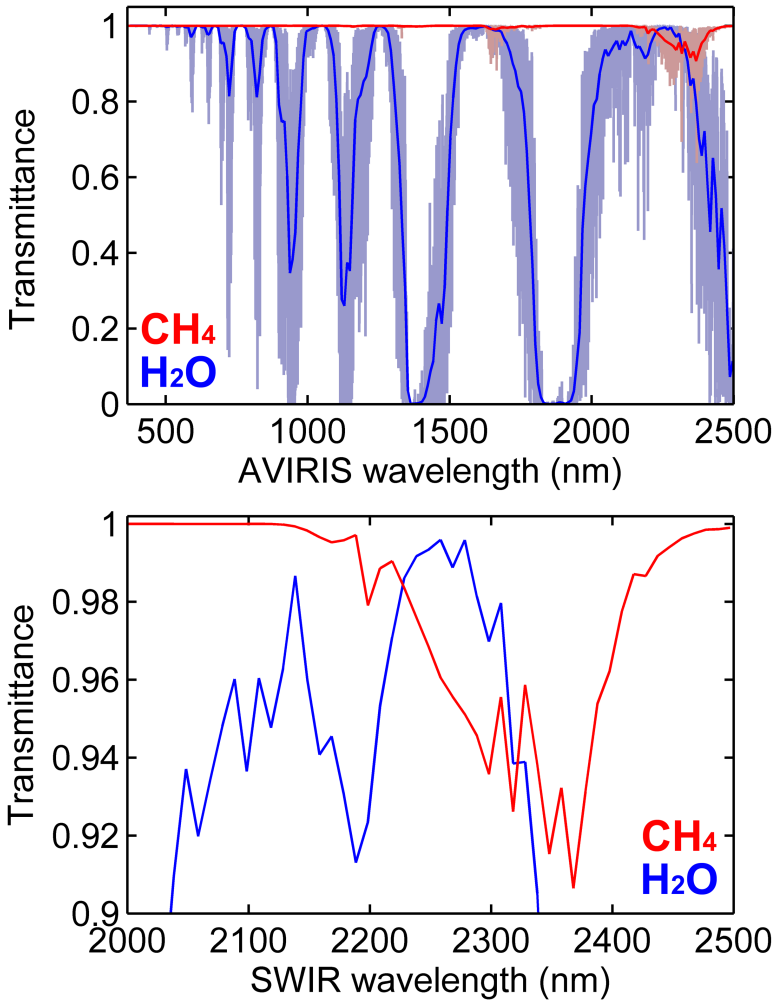

Figure 2.1. (top) CH_4 and H_2O transmittance spectra generated using Modtran 5.3, parameterized for a mid-latitude summer model atmosphere and 8.9 km sensor altitude for the COP scene. Transmittance is shown in high resolution for CH_4 (light red) and H_2O (light blue) and convolved to AVIRIS wavelengths for CH_4 (dark red) H_2O (dark blue). (bottom) SWIR region showing considerable spectral overlap between H_2O and CH_4.

In addition to absorptions in the TIR, CH_4 has absorptions in the shortwave infrared (SWIR) between 1,400 and 2,500 nm (Fig. 2.1, top). In this region, water vapor has considerable spectral overlap with CH_4, particularly beyond 2,300 nm, which complicates CH_4 detection (Fig. 2.1, bottom). These SWIR absorptions enabled global CH_4 mapping by the Scanning Imaging Absorption Spectrometer for Atmospheric Chartography (SCIAMACHY) onboard the Envisat satellite, a grating spectrometer with eight channels operating from 240 to 2,400 nm with a spectral resolution between 0.2 to 1.4 nm and spatial resolution ranging from 30 × 60 km to 30 × 240 km (Buchwitz et al. 2005b). The Weighting Function Modified Differential Optical Absorption Spectroscopy (WFM-DOAS) retrieval algorithm (Buchwitz et al. 2000) was applied to 2003 data from SCIAMACHY channels 4, 6, and 8 to estimate column amounts of CO (carbon monoxide), CO_2, and CH_4 (Buchwitz et al. 2005b). Frankenberg et al. (2005b) developed an iterative maximum a posteriori-DOAS (IMAP-DOAS) algorithm using DOAS and the linear relationship between vertical column-densities for CO_2 and CH_4 to estimate global CH_4 column-averaged mixing ratios over terrestrial surfaces and detect regions with high column averages, including the Red Basin in China and the Sudd wetlands of southern Sudan (Frankenberg et al. 2011). While the Envisat satellite mission ended in 2012, the Greenhouse Gas Observing Satellite (GOSAT) (Saitoh et al. 2009) continues to provide global CH_4 mapping in good agreement with ground based measurements (Butz et al. 2011) and results from global 3-D chemical transport models (Parker et al. 2011).

Global CH_4 concentrations are well constrained due to existing spaceborne remote sensing that provides an effective means of detecting continental scale variation in CH_4 concentrations. However, spaceborne sensors lack the fine spatial resolution needed to detect

near-surface emissions. Local emission monitoring typically relies upon ground-based measurements with limited spatial coverage, such as gas chromatography, tunable diode lasers (Hsu et al. 2010), or Fourier transform spectrometers at fixed sites (Wunch et al. 2009). Airborne sensors could provide valuable data for constraining emissions at local to regional scales (NRC 2010). Improved constraint of emissions at these scales is critical for improving national greenhouse gas budgets and the partitioning between anthropogenic and natural sources (Bovensmann et al. 2010). Airborne measurements could also help address discrepancies between top-down and bottom-up estimates of emissions (Montzka et al. 2011) and complement ongoing global monitoring efforts at coarser spatial resolutions (Schepers et al. 2012).

Airborne imaging spectrometers are well suited for monitoring local sources because they can provide coverage over large regions with the fine spatial resolution necessary to resolve point source emissions. The Airborne Visible Infrared Imaging Spectrometer (AVIRIS) measures reflected solar radiance across 224 contiguous spectral bands between 350 and 2,500 nm with a signal-to-noise ratio that should permit CH_4 mapping (Leifer et al. 2006b). Roberts et al. (2010) used AVIRIS data acquired over the Coal Oil Point (COP) seep field in the Santa Barbara Channel, California to calculate spectral residuals for CH_4 above background and a CH_4 index derived from the average residual between 2,248 and 2,298 nm. Although strong CH_4 anomalies were detected in close proximity to known seeps, mapping proved challenging given results were overly sensitive to albedo (Roberts et al. 2010).

Using a high-glint AVIRIS scene acquired over COP, Bradley et al. (2011) developed a band ratio technique using radiance for a CH_4 absorption band (2,298 nm) and a CO_2 absorption

band (2,058 nm) to generate the AVIRIS CH_4 index, ζ ($\vec{L}_{2298}/\vec{L}_{2058}$). In the absence of strong local sources of CH_4 or CO_2, these gasses are well mixed and a regression of CH_4 and CO_2 bands produces a straight line. If additional CH_4 above background is present in the lower boundary layer and CO_2 is well mixed, radiance for the CH_4 band decreases due to increased absorption, resulting in a lower CH_4 to CO_2 band ratio. Despite variations in surface albedo, this method clearly detected a CH_4 plume that was consistent with wind advection from a sonar-quantified source (Bradley et al. 2011).

While Roberts et al. (2010) and Bradley et al. (2011) demonstrate that CH_4 from marine sources can be detected using AVIRIS scenes with high sunglint, these techniques cannot be applied to terrestrial locations that rarely exceed 50% albedo, where the majority of anthropogenic emissions occur (NRC 2010). Although water can often be assumed spectrally flat in the SWIR (Roberts et al. 2010), this assumption is unrealistic for most land cover types. Spectral variation in surface reflectance arising from heterogeneous land cover invalidates the use of a ratio, where a change in radiance at 2,298 nm relative to 2,058 nm could either be a product of changing CH_4 or CO_2 absorption, or a change in surface reflectance with wavelength.

This study aims to improve methods for detecting absorption features of CH_4, thereby permitting high spatial resolution mapping of local emissions over marine environments and heterogeneous terrestrial surfaces. We applied a Cluster-Tuned Matched Filter (CTMF) technique (Funk et al. 2001) to AVIRIS scenes from the COP seep field and a portion of Los Angeles known for natural CH_4 and oil seepage. The CTMF algorithm identified a number of significant CH_4 anomalies over known and probable CH_4 sources, including natural marine and

terrestrial CH_4 seepage and a CH_4 plume at the Inglewood Oil Field.

2.3 Methods

2.3.1 Study sites

The COP seep field as well as the Mid-Wilshire and Inglewood neighborhoods of Los Angeles, California were the focus of this study because they contain known CH_4 sources from marine and terrestrial environments (Fig. 2.2). Located offshore of Santa Barbara, California, the COP seep field is one of the largest and best studied sources of natural CH_4 emissions. Major seeps include the Trilogy Seep, Horseshoe Seep, and IV Super Seep with bubble diameters ranging between 200 and 104 μm (Leifer et al. 2006a) and CH_4 fractions between 50 and 70% at the surface (Clark et al. 2010). Total atmospheric CH_4 emissions for COP are estimated at 100,000 m^3/day (Hornafius et al. 1999), while the global contribution from marine seepage is estimated at 50 Tg CH_4 yr^{-1} of which 30 Tg CH_4 yr^{-1} reaches the atmosphere (Kvenvolden and Rogers 2005).

The terrestrial study sites are located in Los Angeles, California, which has a history of poor air quality and CH_4 concentrations well above global averages (Townsend-Small et al. 2012). Located approximately 8 to 12 km west of downtown Los Angeles, the Mid-Wilshire and Inglewood neighborhoods have significant oil and CH_4 seepage. This is most clearly illustrated by the hydrocarbon and water mixture with visible CH_4 bubbles present at the La Brea Tar Pits. In the surrounding areas, CH_4 gas can often be seen bubbling from between cracks in paved surfaces after rains (Gurevich et al. 1993). Following the 1985 Ross Department Store explosion caused by natural CH_4 buildup, the city of Los Angeles designated a Methane Zone and Methane Buffer Zone with additional building codes requiring CH_4 miti-

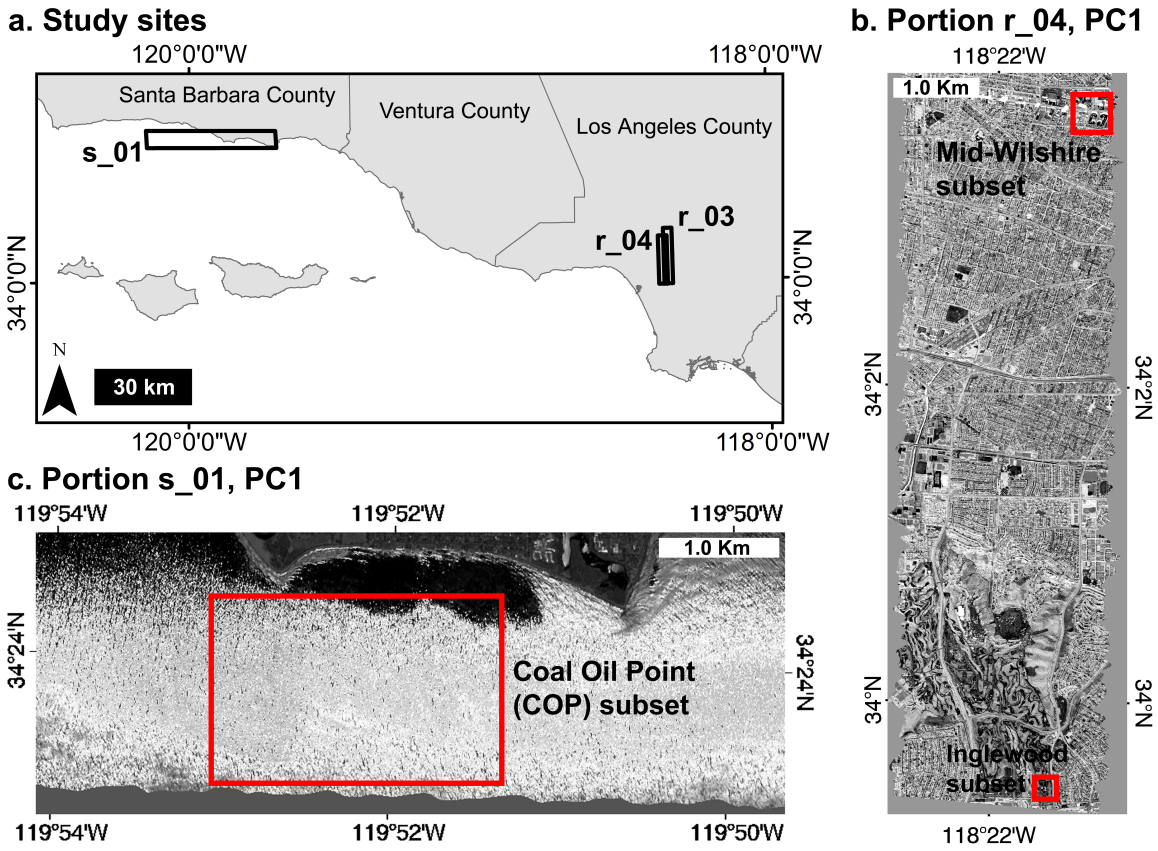

Figure 2.2. (a) Study sites showing one AVIRIS scene for COP (s_01) and two overlapping flight lines (r_03, r_04) in Los Angles. (b) First principal component (PC1) for portion of r_04 showing Mid-Wilshire and Inglewood subsets. (c) PC1 for portion of s_01 showing COP subset.

gation such as gas detectors in addition to active and passive venting systems (Chilingar and Endres 2005). Beyond potential safety hazards, CH_4 seepage on the global scale contributes to the estimated 20 to 40 Tg CH_4 yr^{-1} released globally by natural terrestrial CH_4 seepage (Etiope et al. 2009).

The urban Los Angeles Basin contains over 70 oil fields (Chilingar and Endres 2005) with over 21,000 inactive or active oil and natural gas wells in Los Angeles county alone (DOGGR 2010a). Much of the basin has elevated levels of CH_4, between 1.91 to 2.10 ppm based on data from four monitoring stations averaged over 1994 and 1995 (Dwight Oda California Air Resources Board, personal communication, 2010) and more recently 1.76 to 2.16 ppm in 2008

(Hsu et al. 2010). Preliminary research using stable isotope analysis suggests elevated levels of CH_4 in the Los Angeles area result primarily from non-biogenic sources such as hydrocarbon refining and gas pipelines (Townsend-Small et al. 2012). Significant diurnal variation in CH_4 concentrations has been measured and can result from transport of CH_4 enhanced air from Los Angeles to other regions of the South Coast Air Basin (Wunch et al. 2009).

Over 1,700 inactive or active wells, mostly concentrated in the Salt Lake and Inglewood Oil Fields, are located in the 70 km^2 study site (DOGGR 2010a), which was imaged by two sequential AVIRIS flights (Fig. 2.2a). Because many of these wells were drilled decades ago and subsequently abandoned, CH_4 leaks are well documented and primarily result from improperly sealed wells. There are an estimated 528 improperly sealed wells for the Salt Lake Oil Field alone (Pipkin and Proctor 1992). At the Inglewood Oil Field, there is active hydrocarbon extraction, producing approximately 3.1 million barrels of oil (bbl) and 1.5 billion cubic feet (Bcf) of natural gas in 2008 (DOGGR 2010b).

2.3.2 AVIRIS data

Flown on aircraft at altitudes ranging between 4 and 20 km, AVIRIS measures radiance at nadir with a spectral sampling interval and nominal full width half maximum (FWHM) of 10 nm, 34° field of view (FOV), and 1 mrad instantaneous field of view (IFOV) (Green et al. 1998). For this study, one AVIRIS scene was acquired for COP at approximately 19:55 UTC on 19 June 2008 from 8.9 km altitude (Fig. 2a, s_01), with a solar zenith of 11.4° (high sunglint), ground IFOV of 7.5 m, and swath width of 5.4 km. Two sequential flight lines were acquired for the Mid-Wilshire and Inglewood neighborhoods of Los Angeles between 20:57 and 21:20 UTC on 18 September 2008 from 4.0 km altitude (Fig. 2.2a, r_03 and r_04), with a

solar zenith of 38.1°, ground IFOV of 3 m, and swath width of 2.7 km. AVIRIS radiance data were georectified and radiometrically calibrated by the Jet Propulsion Laboratory (JPL).

The two Los Angeles flight lines were processed to surface reflectance using a technique described by Roberts et al. (1997). This involved forward inversion to match AVIRIS radiance with modeled Modtran radiance while varying column water vapor. Column water vapor estimates were refined, averaging around 1 cm, and a ground reflectance target was used to reduce reflectance artifacts (Clark et al. 2002). In order to investigate algorithm performance, radiance and surface reflectance images were used at terrestrial locations for the CTMF analysis. For COP, the radiance image was used to avoid surface reflectance artifacts caused by low reflectance and high sunglint.

2.3.3 Cluster-Tuned Matched Filter

Theiler and Foy (2006) and Villeneuve et al. (1999) demonstrated that the Simple Matched Filter (SMF) and Clutter Matched Filter (CMF) could detect simulated gas plumes. To do so, a matched filter algorithm is trained with a gas target spectrum to generate a linear weighting function that produces high values when an unknown spectrum matches the shape of the gas target spectrum and is distinct from the covariance of the background. The optimal matched filter calculation uses the inverse of the scene's covariance structure to remove large-scale noise (background clutter) and to isolate the gas signal. Matched filters assume that the signal does not contribute substantially to the background scene-wide covariance. Thus, matched filters are best suited for detecting concentrated sources rather than elevated background levels present over entire scenes.

The CTMF algorithm was originally developed by Funk et al. (2001) to detect faint sulphur

dioxide (SO_2) signatures superimposed on synthetic thermal images using the absorption coefficient to calculate the gas target spectrum. This study explored the use of transmittance since radiance has a linear relationship to transmittance and causes reduced radiance with increasing concentration, matching the expected impact of increased concentration in radiance space. In contrast, an increase in the absorption coefficient translates to a decrease in radiance, the opposite pattern observed in radiance space in the SWIR.

Originally developed for use with 128 spectral bands between 7.8 and 13.5 micrometers, the CTMF algorithm was modified to permit use with the 224 AVIRIS bands between 350 and 2,500 nm. The CTMF was designed for weak signal detection and assumes gas plumes are modeled as a linear superposition of gas signal and background clutter as shown in the following equation (Eq. 2.1),

$$\vec{r} = \vec{u} - \alpha\vec{b} + \epsilon \tag{2.1}$$

where radiance or reflectance ($\vec{r}$) can be modeled as the linear combination of the mean background radiance or reflectance ($\vec{u}$), a gas absorption term ($-\alpha\vec{b}$) that reduces radiance or reflectance in the SWIR, and ϵ, which contains both sensor noise and scene clutter. The gas absorption term contains the gas signal strength (α, a scalar representing the amount of signal present in a pixel) multiplied by the gas target spectrum ($\vec{b}$), which contains gas absorption features across the 224 AVIRIS bands. When applying the CTMF to AVIRIS data, atmospheric scattering can be ignored given it occurs at shorter wavelengths than gas absorptions and is usually dominated by background clutter variability.

The CTMF was applied to both radiance and reflectance images for entire AVIRIS flight lines that were first standardized by subtracting the mean and dividing by the standard de-

viation of the scene, both scalar values. A sample-based k-means algorithm using extreme centroid initialization was used with the first few principle components of the image to assign extreme locations for each of the k-means class centroids (Funk et al. 2001). For the Coal Oil Point and Los Angeles radiance scenes, principle components were calculated using all 224 image bands. For the Los Angeles reflectance images, principle components were calculated using 180 bands that excluded those characterized by high sensor noise or strong water vapor absorptions.

After the k-means algorithm assigns clusters and creates a k-means class image, a CTMF specifically tuned for each class was calculated. The CTMF was 'matched' to both the gas signature as well as the background clutter and was calculated using the following equation (Eq. 2.2),

$$\vec{q_j} = \frac{\mathbf{C}_j^{-1}\vec{b}}{\sqrt{\vec{b^T}\mathbf{C}_j^{-1}\vec{b}}} \tag{2.2}$$

For class j, $\vec{q_j}$ is the CTMF and represents an n-dimensional vector of optimal weights, where n is the number of spectral channels. $\mathbf{C}_j^{-1}$ is the inverted n by n covariance matrix for the jth class and $\vec{b}$ is the n-dimensional vector containing the gas target spectrum. T is the transpose operator.

Modtran 5.3 (Berk et al. 1989) was used to generate gas transmittance spectra using default gas concentrations defined by a mid-latitude summer model with 30 km visibility, 293.15 K boundary temperature, scattering turned off, and the sensor altitude for each flight line. Modtran transmittance for CH_4 and H_2O was convolved to AVIRIS wavelengths using the band centers and FWHM supplied by JPL. CH_4 and H_2O transmittance spectra indicating gas absorptions are shown in Fig. 2.1 for COP, including both the high resolution and convolved

transmittance shown for CH_4 (red) and H_2O (blue). For the COP scene, the sensor altitude was set to 8.9 km with total column absorber amounts of 208.77 atm-cm for CO_2, 0.913 atm-cm for CH_4 and 3,615.90 atm-cm for H_2O, approximately 385.01, 1.68, and 6,668.34 ppmV respectively.

The sensor altitude was lower for the Los Angeles scenes (4.0 km), resulting in smaller total column absorber amounts of 117.59 atm-cm for CO_2, 0.519 atm-cm for CH_4 and 3,230.10 atm-cm for H_2O. Given CO_2 and CH_4 are well mixed gasses in Modtran, the estimated 385.00 (CO_2) and 1.70 (CH_4) ppmV for the Los Angeles scenes are similar to COP, however, the higher value of 10,575.56 ppmV for H_2O results from decreased path length (lower sensor altitude) and more water vapor near the surface. Fig. 2.5 shows CH_4 and H_2O transmittance spectra for the Los Angeles scenes with 180 bands excluding those characterized by high sensor noise or strong water vapor absorptions that can cause reflectance artifacts.

These gas transmittance spectra were used to calculate the CH_4 and H_2O target spectrum ($\vec{b}$) for each scene using the following equation (Eq. 2.3),

$$\vec{b} = \vec{t}ps \tag{2.3}$$

where the n-dimensional vector $\vec{t}$ is the standardized gas transmittance spectrum, which is calculated by subtracting the mean of this spectrum and dividing by the standard deviation. Next, $\vec{t}$ is scaled by a percentage (p, gas signal percent) of the standard deviation of the image (s, a scalar value); p is chosen empirically prior to applying the CTMF algorithm (see Sect. 2.3.4). The CH_4 and H_2O target spectrum was used to generate CH_4 and H_2O CTMF results for the three AVIRIS images. Given spectral overlap between CH_4 and H_2O (Figs. 2.1 and 2.5), H_2O CTMF results were used as a means of validating CH_4 CTMF results.

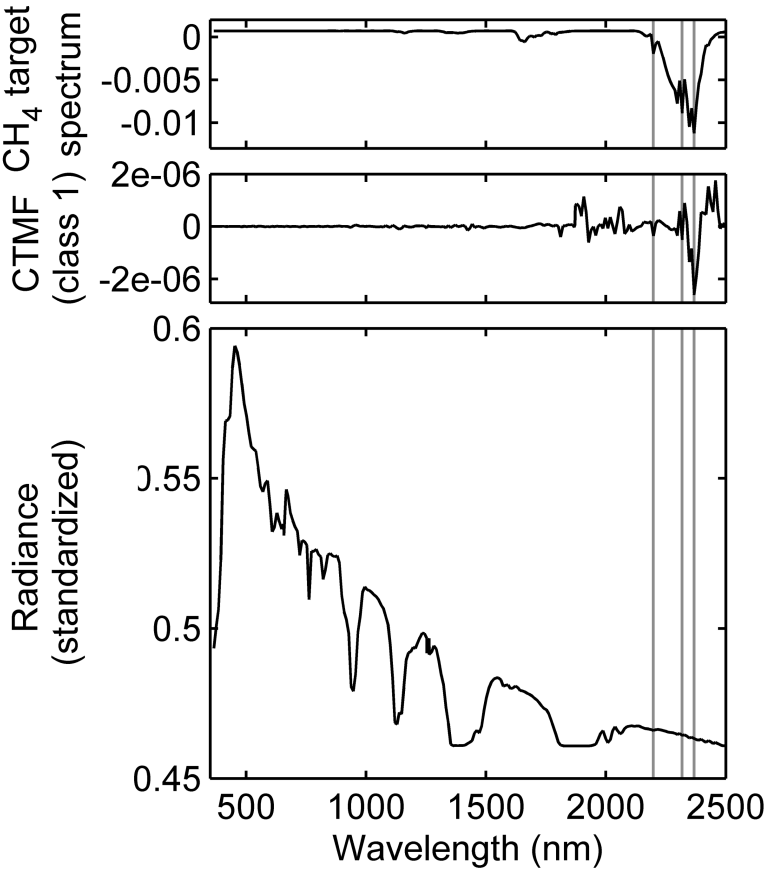

Figure 2.3. (top) CH_4 target spectrum for COP scene. (middle) CTMF for one class. (bottom) Standardized radiance spectrum for an ocean pixel containing sunglint within the class. Vertical lines indicate locations of strong CH_4 absorptions at 2,198, 2,318, and 2,368 nm.

In Fig. 2.3 (top) an example of the CH_4 target spectrum ($\vec{b}$) is shown calculated for the COP radiance image using p=0.002 of the standard deviation of the image. The CTMF for class j=1 ($\vec{q_j}$) is also included (Fig. 2.3, middle) with strong CH_4 absorptions indicated by vertical lines. An example standardized radiance spectrum for an ocean pixel containing sunglint ($\vec{r_i}$ for the ith pixel within this class) is shown in Fig. 2.3 (bottom).

Next, a CTMF score for ith pixel within the class (f_i) was calculated by multiplying the transpose of the CTMF ($\vec{q_j}$) by each standardized image spectrum within the class ($\vec{r_i}$, for radiance or reflectance), as shown in the following equation (Eq. 2.4),

$$f_i = \vec{q_j^T}\,\vec{r_i} \tag{2.4}$$

Resulting from the combined operations of Eq. 2.2 and 2.4, multiplication by the inverted covariance matrix in the numerator in Eq. 2.2 'whitens' the data, removing spectral cross-correlation in the background clutter. The denominator standardizes the filter so that the CTMF image will have a variance of 1 when the signal is absent.

The CTMF score for each pixel within a class is standardized by subtracting the mean CTMF score for the class and dividing by the standard deviation of the class. This results in a mean CTMF score of 0 and standard deviation of 1 for the class; the standardization procedure continues for all j classes. Filtered pixels are then recomposed as a final output image that reduces noise and sensitivity to surface features while enhancing the gas signature.

When interpreting the CTMF image, scores greater than one indicate evidence of the gas signature, which can be quantified by the 'number of sigmas' for the z distribution. However, sigmas only can be interpreted as literal probabilities if the background clutter is Gaussian (Funk et al. 2001). Because a CTMF specifically tuned for each k-means class is used, high CTMF scores for pixels from different k-means classes that appear as contiguous pixels in CTMF images can be interpreted as highly significant. These contiguous pixels represent gas anomalies that cross over multiple land cover types and can be evaluated for consistency with known or probable emissions sources and local wind direction.

The example shown in Fig. 2.4 illustrates some of the challenges in detecting a gas signal over heterogeneous surfaces. For radiance or reflectance measured in two spectral bands, pixels representing the scene background clutter are shown as open circles and one pixel with gas signal added (Band 1 decrease due to absorption in this band) is included as a filled red circle. Fig. 2.4a shows a projection of the data cloud containing all pixels by the Clutter

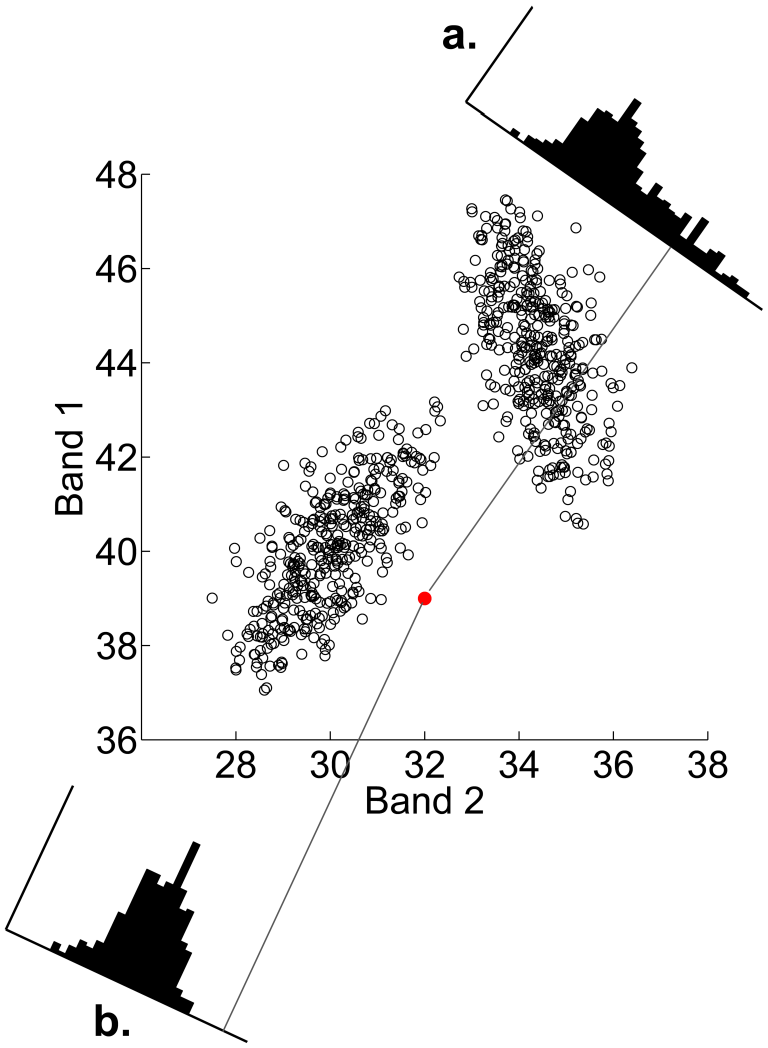

Figure 2.4. For radiance (or reflectance) in two spectral channels, background clutter of the scene is shown as open circles and one pixel with gas signal added (decrease in Band 1 due to absorption) as filled red circle. (a) Projection of data cloud containing all pixels (dark and bright) by the Clutter Matched Filter (CMF) so that the pixel with the added signal will be most readily detected, but does not stand out as highly significant. (b) Projected data for only dark pixels using the Cluster-Tuned Matched Filter (CTMF) technique, resulting in the pixel with added gas signal standing out as highly significant.

Matched Filter (CMF) so that the pixel with the added gas signal will be most readily detected, but the pixel containing the gas signal does not stand out as highly significant. In Fig. 2.4b, the background clutter is first partitioned into two clusters consistent with two classes of surface materials, brighter pixels in the upper right and darker pixels in the lower left. The Cluster-Tuned Matched Filter (CTMF) is applied to the dark pixel cluster and the projected data for

only darker pixels causes the pixel with added gas signal to stand out as highly significant. By classifying an image using k-means clustering and reducing within-class variance, a CTMF should improve performance over traditional matched filters by creating a matched filter that is specifically tuned for each cluster (Funk et al. 2001).

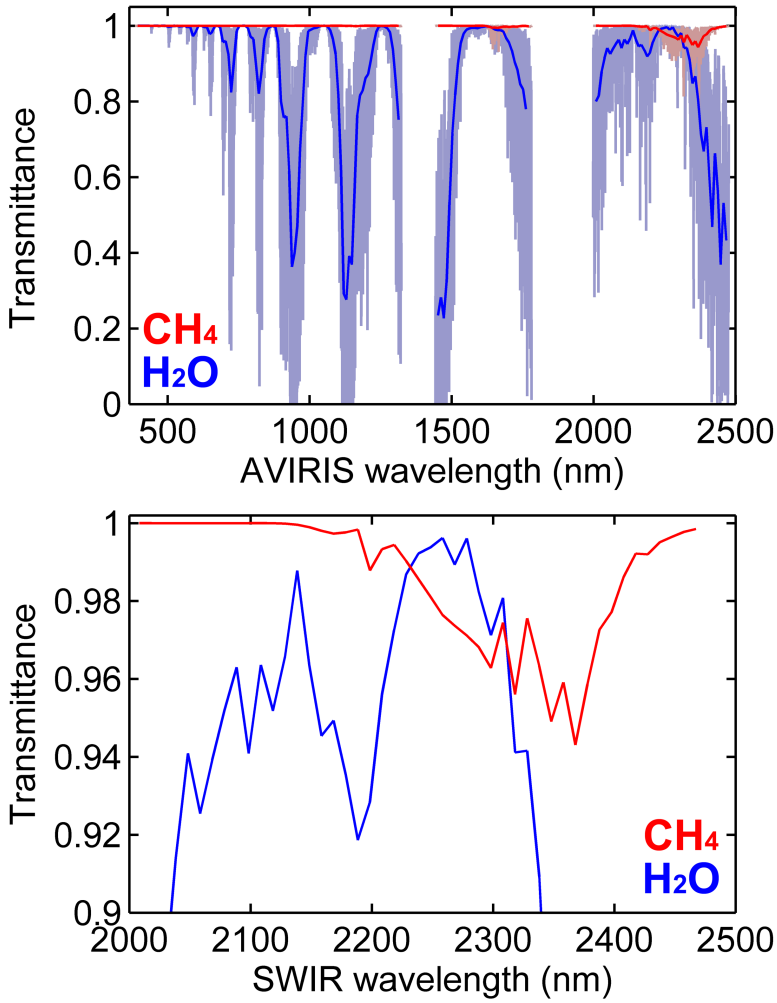

Figure 2.5. (top) CH_4 and H_2O transmittance spectra excluding bands with strong water vapor absorptions for the Los Angeles scenes generated using Modtran 5.3 parameterized for a mid-latitude summer model atmosphere and 4.0 km sensor altitude. Transmittance is shown in high resolution for CH_4 (light red) and H_2O (light blue) and convolved to AVIRIS wavelengths for CH_4 (dark red) and H_2O (dark blue). (bottom) SWIR region.

2.3.4 Input parameters for Cluster-Tuned Matched Filter

Two factors govern the performance of the CTMF – the number of clusters identified and the gas signal percent (p), which scales the gas transmittance spectrum by a percentage of the standard deviation of the image (Eq. 2.3). To determine an appropriate number of clusters for the k-means algorithm, a key objective is to maximize the number of clusters needed to discriminate land cover classes and reduce within-class variance, while maintaining enough pixels in each cluster to ensure adequate sample size and that the variance in the gas signal remains less than the variance of the image clusters. This is particularly important given that the CTMF calculation (Eq. 2.2) explicitly removes the background clutter, assuming that the gas signal is independent. In this study, the number of clusters was increased iteratively while maintaining a minimum of 1,000 pixels in each cluster, resulting in 36 clusters for the entire COP scene.

For the COP scene, the CH_4 signal percent (p) was determined empirically by varying the scalar between 0.0001 and 1.00 using the 36 cluster k-means result. A visual comparison between results obtained using extreme values showed appreciable differences, but it became difficult to distinguish between the remaining results. Overall, a CH_4 signal percent of 0.002 produced anomalies that appeared the most clearly defined.

Radiance images were initially used for the Los Angeles scenes, however, CTMF anomalies were more clearly defined using the surface reflectance images due to improved classification of the heterogeneous urban environment by the k-means algorithm. For flight line r_04, k-means class images generated for different numbers of clusters were analyzed and indicated that 321 clusters maximized the number of clusters while maintaining cluster size

above 1,000 pixels for the surface reflectance image. The CH_4 signal percent was varied between 0.0001 and 1.00, but identifying the optimal result remained challenging so 0.002 was used for consistency with the COP example.

2.3.5 Segmentation and classification

In order to reduce noise and isolate contiguous pixels with high CTMF scores, a segmentation approach based on 8−connectivity was used by defining a score threshold and minimum number of pixels for the segments. An iterative process was used to determine the appropriate threshold and minimum population that preserved regions of contiguous pixels without resulting in too many small segments. Next, a mask of the segments was applied to the reflectance scene, resulting in an image that contained reflectance spectra only for segmented regions.

To distinguish true CH_4 anomalies from false positives, reflectance spectra from the segmented regions were classified using MESMA (Multiple-Endmember Spectral Mixture Analysis) (Roberts et al. 1998). MESMA is particularly well suited for the spectral diversity of urban environments because it permits the number and types of endmembers to vary on a per-pixel basis (Roberts et al., 2012). 'Viper-tools,' an ENVI add on (www.vipertools.org), was used to generate the spectral library that was used in the classification.

A spectral library was generated from endmembers obtained in the field using an Analytical Spectral Device (ASD Inc., Boulder, Colorado) full range spectrometer that samples between 350 and 2,500 nm and image endmembers from the AVIRIS scene. The Endmember Average Root Mean Square Error (EAR) method was utilized to optimize the endmembers for the spectral library by creating the smallest number of spectra for each land cover class

while maximizing the separation between surfaces (Dennison and Roberts 2003). EAR uses MESMA to calculate the average error for a given endmember in modeling spectra within a land cover class; endmembers with lower within class average root mean square error (RMSE) are representative endmembers for a given land cover class. Endmembers were organized into two MESMA classes: surfaces prone to false positives (confusers) and probable CH_4 anomalies. These endmembers were used to unmix the segmented reflectance image and generate a classification image indicating which anomalies are probable CH_4 anomalies or likely false positives.

2.4 Results

2.4.1 Cluster-Tuned Matched Filter

2.4.1.1 Coal Oil Point

CTMF results obtained using 36 clusters and a CH_4 signal percent of 0.002 produced anomalies with a maximum CTMF score of 43.8 (positive values as CH_4 anomalies), minimum of -48.5, mean of 0.0, and standard deviation of 1.0 for the entire COP radiance image. A subset of CTMF results is shown in Fig. 2.6d for a region of high sunglint as well as dark ocean pixels, with a maximum radiance measured in $\mu W cm^{-2} sr^{-1} nm^{-1}$ at 2,100 nm of 6.466 (sensor saturation), minimum of 0.026 (0% reflectance), and mean of 2.779 (95.7% reflectance) within the image subset. In Fig. 2.6d, high CTMF scores represent large sigma values that indicate rotated pixels that are far from the expected value of 0 (Fig. 2.4b) and are very likely to contain elevated CH_4 concentrations. Bright pixels clearly indicate positive CH_4 anomalies consistent with a southwesterly wind measured at the nearby West Campus Station (2.3 ms^{-1} from 236°).

These anomalies emanate from known seeps, including the Trilogy Seep (TRI), IV Super

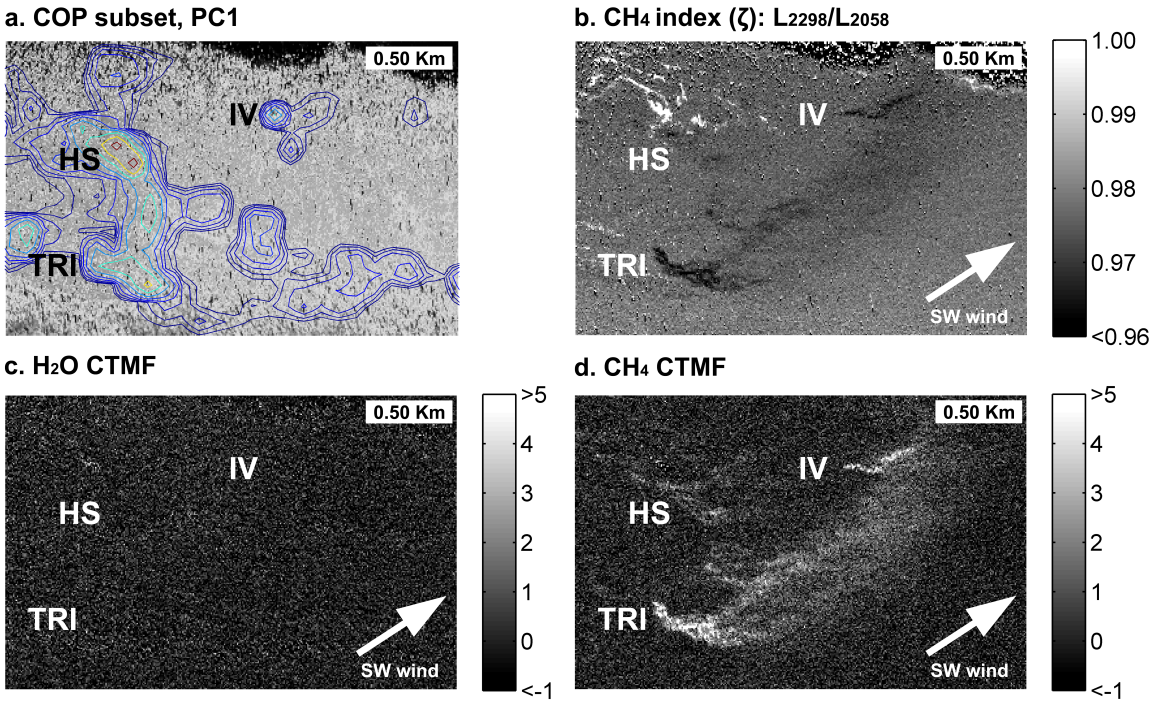

Figure 2.6. (a) PC1 for COP subset shown in Fig. 2.2c overlain with sonar contours (Leifer et al. 2010) indicating known seeps, including the Trilogy Seep (TRI), IV Super Seep (IV), and Horseshoe Seep (HS). (b) AVIRIS CH_4 index, ζ ($\vec{L}_{2298}/\vec{L}_{2058}$), indicating elevated CH_4 (dark pixels) corresponding with known seep locations. (c) For the same region, CTMF results for water vapor show no H_2O anomalies. (d) CTMF results for CH_4 with positive values denoting CH_4 anomalies (bright pixels) consistent with results obtained using CH_4 index.

Seep (IV), and Horseshoe Seep (HS), as shown by sonar return contours of subsurface bubble plumes in Fig. 2.6a (Leifer et al. 2010). These CH_4 anomalies also closely resemble results obtained using the AVIRIS CH_4 index, ζ ($\vec{L}_{2298}/\vec{L}_{2058}$), developed by Bradley et al. (2011). In Fig. 2.6b, AVIRIS CH_4 index results for the same region are shown, with elevated CH_4 indicated by lower values (dark pixels) caused by reduced radiance in the numerator ($\vec{L}_{2298}$) due to increased absorption by CH_4 relative to CO_2 absorptions ($\vec{L}_{2058}$). In Fig. 2.6c, CTMF results for water vapor show no H_2O anomalies, indicating the anomalies present in Fig. 2.6d are due to CH_4. Using visual assessment, we verified that CH_4 anomalies were not present in any of the principal components of the AVIRIS scene and have included the first principal component of the subset in Fig. 2.6a.

2.4.1.2 Los Angeles

For the entire reflectance scene for flight line r_04, the CTMF image had a maximum score of 17.0, minimum of -17.0, mean of 0.0, and standard deviation of 1.0. The CTMF algorithm was also applied to scene r_03 using input parameters previously defined for r_04, resulting in a maximum score of 16.9 and minimum of -13.8. CTMF results indicate a number of well defined CH_4 anomalies coinciding with locations of known or probable CH_4 emission sources. For the overlapping portion of scene r_03 and r_04 (Fig. 2.2), the location of well defined CH_4 anomalies remained consistent in CTMF results from either scene. Visual assessment was used to verify that CH_4 anomalies were not present in principal components of the scene and results compared with CTMF results for water vapor as an additional means of validation. For this study we focus on image subsets containing the most prominent anomalies located at the Inglewood Oil Field and near the La Brea Tar Pits.

The first area of interest is located at the southern edge of the Inglewood Oil Field (Fig. 2.2b, Inglewood subset). For scene r_04, the true color subset shown in Fig. 2.7a has a maximum surface reflectance of 47.6%, minimum of 3.3%, and mean of 26.7% measured at 2,100 nm. For the same region, a plume-like feature is clearly visible in the CTMF result for CH_4 (Fig. 2.7e) while the k-means class image (Fig. 2.7b) indicates that the anomalies cross over multiple classes and thus different land cover types, including soil as well as green and non-photosynthetic vegetation. This is more clearly emphasized in Fig. 2.7c, where the k-means class is plotted for each pixel along the transect shown in Fig. 2.7b. For the same transect shown in Fig. 2.7e, the CH_4 CTMF results are best fit using a robust Gaussian curve (Matlab Curve Fitting Toolbox, Mathworks, Natick, Massachusetts). CTMF results for H_2O

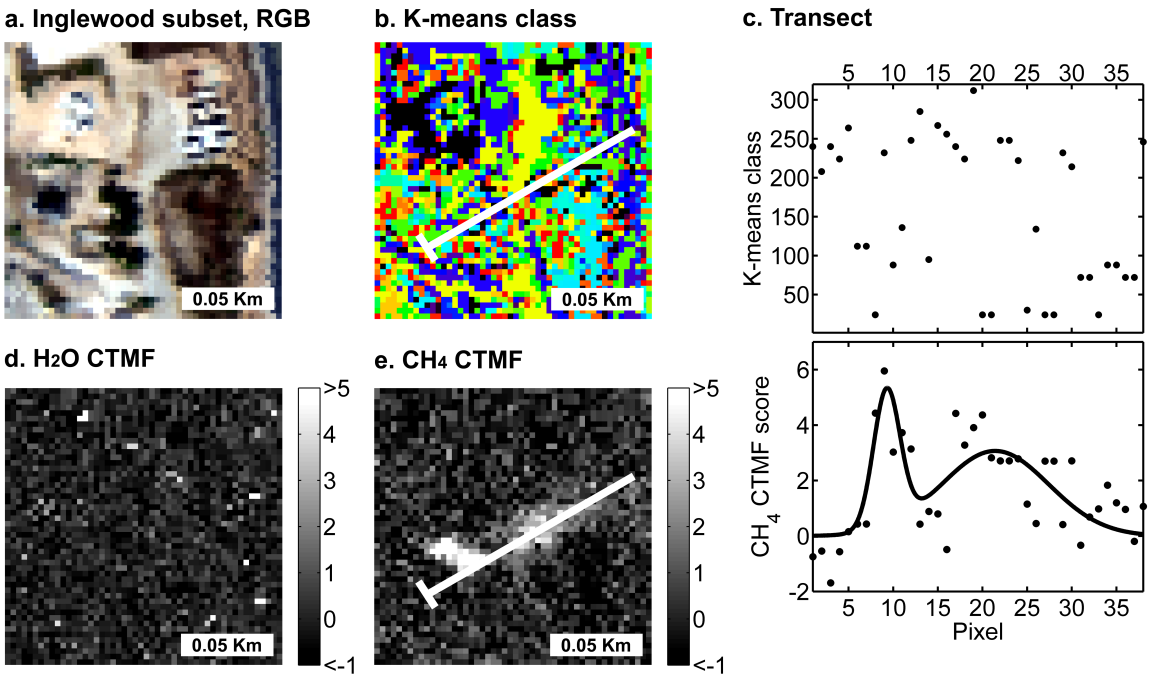

Figure 2.7. (a) Inglewood subset shown in true color (RGB) for flight line r_04. (b) For the same region, k-means class image indicates numerous land cover classes. (c) Along transects shown in b and e, the class and CH_4 CTMF score for each pixel is shown, indicating that the CH_4 anomalies cross over multiple land cover classes. (d) CTMF results for water vapor show no H_2O anomalies. (e) CTMF results for CH_4 with positive values denoting CH_4 anomalies (bright pixels).

are shown in Fig. 2.7d and indicate no H_2O anomalies in the image subset.

Two AVIRIS flight lines were acquired over this location approximately 6.5 minutes apart and CH_4 anomalies clearly change between the earlier scene, r_03 (Fig. 2.8b), and the later scene, r_04 (Fig. 2.8d). For presentation, CTMF results are provided for both scenes using a median filter with a 2 by 2 pixel kernel (Fig. 2.8b and 2.8d, left), while the original results are displayed with identical transects (T1 and T2 in Fig. 2.8b and 2.8d, right). To compare changes in the anomalies between scenes, CH_4 CTMF results for transects were best fit using robust Gaussian curves. Transect 1 (T1 in Fig. 2.8c) crosses a portion of the scene with the highest CTMF scores and comparison of best fit curves indicates the anomalies in the later scene (r_04) exhibits a greater amplitude and extent (R^2=0.89, RMSE=1.10) than r_03 (R^2=0.78,

RMSE=0.89).

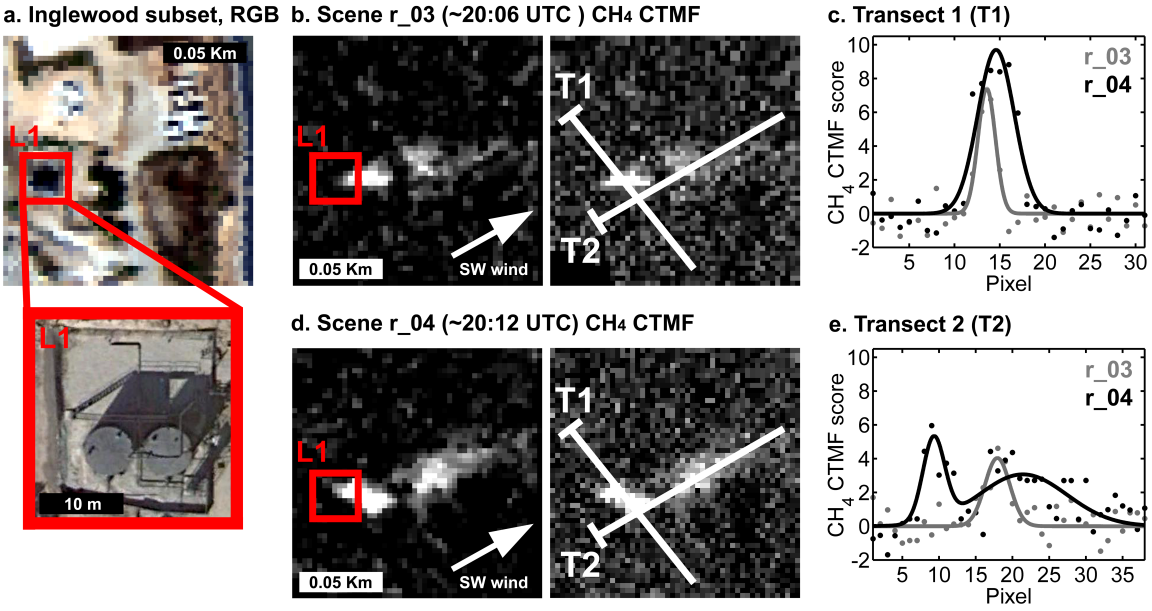

Figure 2.8. (a) Inglewood subset shown in true color with close-up of hydrocarbon storage tanks (Location L1) from 14 Nov. 2009 (Google Earth 2012). (b) CTMF results for CH_4 with positive values denoting CH_4 anomalies for flight line r_03. Left, using median filter with 2 by 2 pixel kernel and on right, original results. (d) CTMF results for r_04. For r_03 and r_04, identical transects are shown on the right. (c) Results for Transect 1 (T1) were best fit using robust 1st order Gaussian curves. (e) Transect 2 (T2) varies significantly between r_03, with 1st order fit, and r_04, with a 2nd order Gaussian fit.

In Fig. 2.8d, Transect 2 (T2) first crosses over the southern edge of the observed CH_4 anomalies, next a stand of trees, and finally a region where CTMF scores appear to gradually decrease. Fig. 2.8e shows a second order fit for Transect 2 of r_04 (R^2=0.54, RMSE=1.30), with values greatest towards the southwest, markedly decreasing in the vicinity of the trees, and gradually decreasing to the northeast. This is consistent with local meteorological data indicating a 2.2 ms^{-1} southwesterly wind at the time of image acquisition (weatherunderground.com 2012). It is unclear whether the trees are obscuring the CH_4 signal due to liquid water absorption and low reflectance in the SWIR, or if the spatial patterns are the result of an intermittent release. Transect 2 for r_03 was modeled with a first order Gaussian fit (R^2=0.54, RMSE=0.88), clearly indicating significant change in the plume profile during the

6.5 minutes between the two flight lines. This is consistent with a gas plume rather than a stationary surface material causing a false positive. Google Earth imagery from 14 November 2009, acquired one year after the AVIRIS flights, was used to resolve surface features, including what appears to be two hydrocarbon storage tanks located immediately upwind of the anomalies (Location L1 in Fig. 2.8a) (Google Earth 2012). Given the CH_4 plume is likely near the surface, the changing appearance between scenes cannot be explained by differing view geometries, which would cause a small spatial shift rather than a significant change in the shape of the anomalies.

Eight kilometers north of the Inglewood subset, several CH_4 anomalies are observed in the region surrounding the La Brea Tar Pits (Fig. 2.2b, Mid-Wilshire subset). A subset of the scene is shown in Fig. 2.9a, with a maximum surface reflectance of 53.8%, minimum of 0.3%, and mean of 14.1% measured at 2,100 nm within the image subset. Prominent CH_4 anomalies are visible on the eastern edge of the La Brea Tar Pits, a hydrocarbon and water mixture known to produce large CH_4 bubbles tens of centimeters in diameter (Fig. 2.9e, Location L1). On the opposite corner of Wilshire Boulevard and Curson Avenue, CH_4 anomalies are located in a courtyard bounded by two multi-story office buildings (Fig. 2.9e, Location L2). These buildings are documented as continuously venting CH_4 (Chilingar and Endres 2005). The CH_4 appears to accumulate in the courtyard, where it would be almost completely surrounded by the six-story office complex. These anomalies extend through the north entrance of the courtyard, remain faintly visible immediately north of the office complex, and are consistent with CH_4 advection by southwesterly winds.

Closer inspection of CH_4 CTMF results indicates the courtyard anomalies cross over mul-

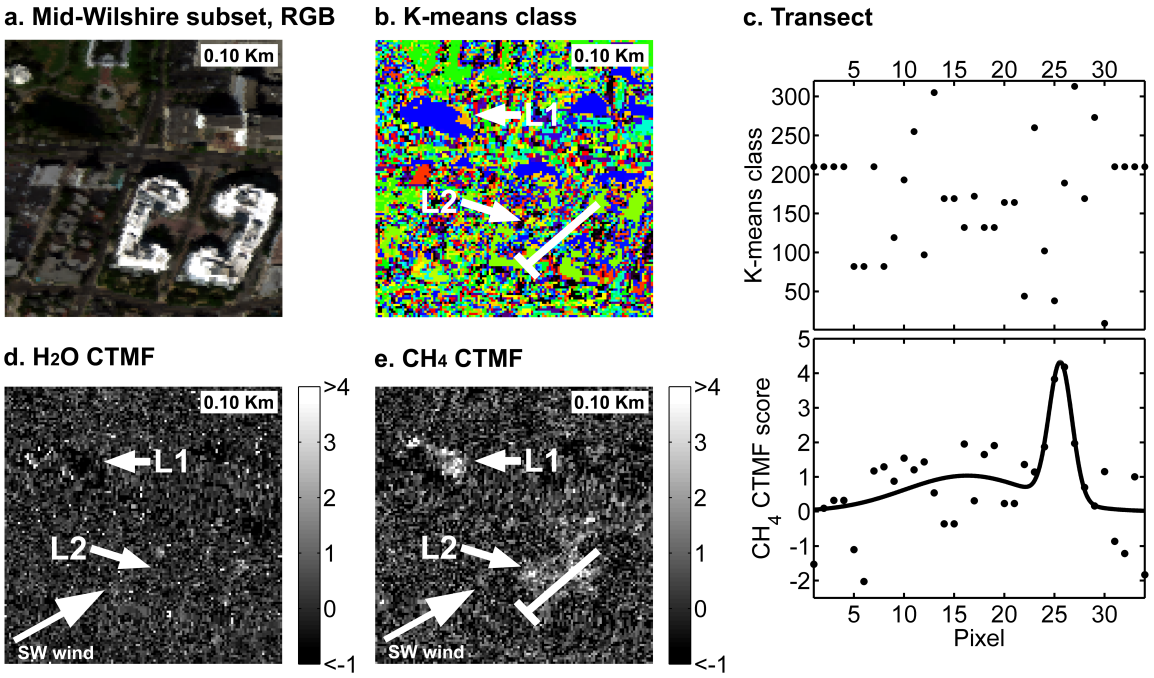

Figure 2.9. (a) Mid-Wilshire subset for flight line r_04 shown in true color. (b) For the same region, the k-means class image indicates numerous land cover classes. (c) Along transects shown in b and e, the class and CTMF score for each pixel is shown, indicating that the CH_4 anomalies cross over multiple land cover classes. (d) CTMF results for water vapor show no H_2O anomalies. (e) CTMF results for same area with positive values denoting CH_4 anomalies. Location 1 (L1) indicates eastern edge of La Brea Tar Pits, a known CH_4 source, and Location 2 (L2) a courtyard bounded by a multi-story office complex with continuous CH_4 venting.

tiple k-means classes (Fig. 2.9b), including impervious and green vegetation land cover types. This is clearly indicated in Fig. 2.9c by comparing the k-means class for each pixel along the transect shown in Fig. 2.9b. CH_4 CTMF scores for the same transect are also shown and indicate elevated values to the northeast. While prominent CH_4 anomalies are located at a known source at the La Brea Tar Pits and probable region of elevated CH_4 in the courtyard, CTMF results for water vapor do not indicate H_2O anomalies at these locations (Fig. 2.9d).

Continuous air samples were collected between 3:00 and 4:00 LT on 22 February 2012 using a cavity ring-down greenhouse gas sensor (G2301, Picarro, Santa Clara, California) (Farrell et al. 2013) to characterize CH_4 emissions for the region surrounding the La Brea Tar

Pits. In Fig. 2.10, CH_4 measurements are shown for a region similar to the Mid-Wilshire subset shown in Fig. 2.9, with concentrations between 3.066 ppm and 45.508 ppm with a mean of 6.44 ppm. Winds were calm at the time of sampling and measurements near the courtyard's south entrance show an approximately Gaussian shape with a 45.508 ppm maximum. This is consistent with CH_4 accumulating in the courtyard from continuous CH_4 venting by the office complex and escaping through the courtyard's south entrance. These results can be compared with CH_4 anomalies shown in Fig. 2.9e that extend through the courtyard's north entrance and are consistent with CH_4 advection by 2.2 ms^{-1} southwesterly winds when the AVIRIS image was acquired on 18 September 2008.

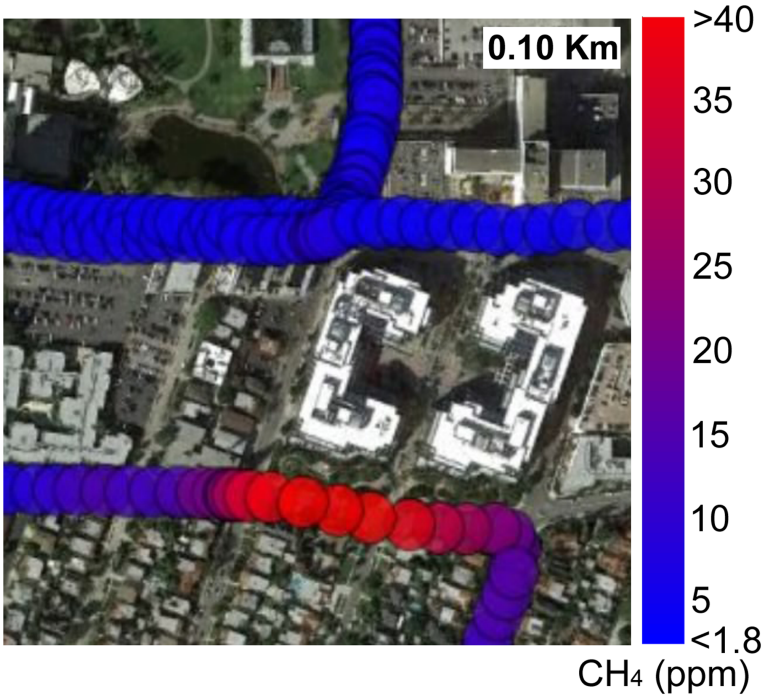

Figure 2.10. In situ CH_4 measurements near the La Brea Tar Pits (2 s time average) indicate concentrations between 3.066 and 45.508 ppm for this scene subset (Google Earth 2012). A pronounced increase in concentration occurs immediately south of the office complex with peak measurements near the south entrance of the courtyard.

2.4.2 Noise and false positives

CTMF results consistently appear noisy and attempts to reduce 'speckle' by varying input parameters, such as the number of clusters and CH_4 signal percent, were largely unsuccessful. As a means of optimizing results, Moran's Spatial Statistics were used to assess local homogeneity (Cliff and Ort 1981), but values remained nearly identical despite varying both the number of clusters and the CH_4 signal percent. The Moran's index appears primarily influenced by noise and false positives present in CTMF results, rather than subtle variations in CH_4 anomalies.

Although well defined anomalies located at and downwind from known or probable CH_4 sources were identified, apparent false positives also occurred and result from surfaces with strong absorptions at the same wavelengths as CH_4. In Fig. 2.11, reflectance spectra for surfaces prone to false positives (confusers) are shown (Spectra S2 through S11) indicating SWIR absorptions consistent with those present in CH_4 transmittance spectrum S1. Confusers included oil-based paints (S2 through S6) and a number of roofs exhibiting a strong absorption feature for calcite (CO_3) at 2,338 (Fig. 2.11, S7).

Apparent false positives generally appeared as contiguous pixels with a shape that mimics an underlying surface feature, for example individual rooftops within CH_4 CTMF results. This suggests that the AVIRIS spectral resolution limits the ability of the CTMF algorithm to accurately resolve between a pure CH_4 signature and land cover types with strong absorption features between 2,200 and 2,500 nm. Despite this, the percentage of pixels within each k-means class exhibiting high CTMF scores remained small across classes, for example 0.01 to 1.27% of pixels within each class exhibited scores greater than 3 for Los Angeles scene r_04.

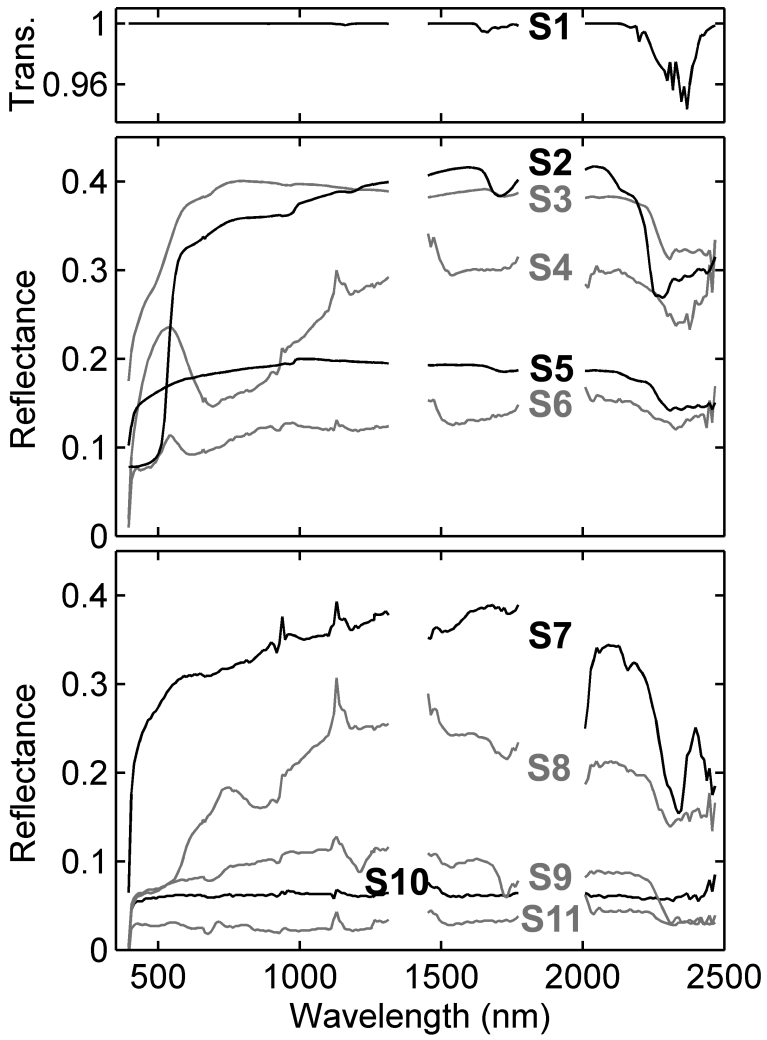

Figure 2.11. Reflectance spectra for surfaces prone to false positives (confusers) are shown (Spectra S2 through S11) indicating absorptions consistent with those present in CH_4 transmittance spectrum S1. Absorptions between 2,048 and 2,467 nm for oil-based paints (S2 through S6) and at 2,338 nm for calcite (S7) explain false positive characterization.

One class containing shade pixels had a higher value of 2.40% suggesting a slight bias towards dark surfaces, however no systematic bias towards the remaining classes was observed.

2.4.3 Segmentation and classification

In order to reduce noise and isolate CH_4 anomalies for Los Angeles scene r_04, segmentation using a CTMF score threshold greater than 1.5 and minimum population size of 55 pixels ($\sim$500 m^2) resulted in 16 segments totaling 1,331 pixels (0.04% of the original pixels within

the AVIRIS scene). To distinguish true CH_4 anomalies from false positives, reflectance spectra from the segmented regions were classified using MESMA. From a spectral library containing 1,089 field spectra obtained between 23 May and 25 June 2001 for the Santa Barbara urban area (Herold et al. 2004), spectra with the lowest 2 or 3 EAR scores for each of the 58 land cover classes were selected. The resulting 164 field spectra then were used to unmix the segmented reflectance scene using a two endmember model consisting of a bright endmember and photometric (spectrally flat) shade, fractional constraints between 0 and 100%, and a root mean square error (RMSE) constraint below 5.0%.

Portions of the segmented reflectance image remained unclassified, so image endmembers were used to supplement the spectral library. Regions of interest (ROIs) were created in the original reflectance image and located outside those areas defined by the segmented reflectance image. For each ROI, the spectrum with the lowest EAR was added to the spectral library as an image endmember. In a few instances, appropriate endmembers could not be found outside of segmented regions so spectra obtained within segments were used. For example, accurate classification of the hydrocarbon and water mixture of the La Brea Tar Pits (Fig. 2.11, S11) only was possible by choosing endmembers at this location. Similarly, image endmembers were selected for suspected false positives caused by three surfaces of unknown composition with strong absorptions in the SWIR: a blue awning (likely a painted metal surface), a running track (likely a rubberized material), and what appears to be plastic sheeting used as an erosion barrier (Fig. 2.11, S4, S8, and S9 respectively).

These field spectra and image endmembers then were organized into two MESMA classes: confusers and probable CH_4 anomalies. A complete list of land cover categories for either

class is shown in Table 2.1, with surfaces prone to false positives (confusers) including oil-based paints, calcite, and surfaces of unknown composition (blue awning, running track, and erosion barrier). Fresh asphalt is another likely confuser, with possible hydrocarbon absorptions in the SWIR resulting from tar. Therefore, the La Brea Tar Pits, a hydrocarbon and water mixture with fresh tar visible on the surface, was included as a potential confuser. The remaining land cover categories were included in the probable CH_4 anomalies class and made up of impervious surfaces not prone to false positives, green and non-photosynthetic vegetation, and soils.

MESMA class	Land cover categories	Number pixels	Percent in segmented image
Probable CH_4 anomalies	Impervious (concrete, brick, tile, etc.)	460	34.56%
	Non-photosynthetic vegetation	187	14.05%
	Green vegetation	170	12.77%
	Soil	95	7.14%
Confusers	Unknown composition	186	13.97%
	Hydrocarbon/water mixture	102	7.66%
	Oil-based paints	80	6.01%
	Calcite	44	3.31%
	Asphalt	7	0.53%
Unclassified pixels		0	0.00%
Total pixels in segmented image		1331	100.00%

Table 2.1. Classification results of segmented reflectance image for flight line r_04 indicating land cover categories for two MESMA classes: probable CH_4 anomalies and confusers.

These spectra were then used to unmix the segmented reflectance image resulting in a

classification using 109 successful models. Field spectra and image endmembers that modeled only a small portion of the scene were removed, reducing the library to 93 spectra. This final spectral library was used to unmix the scene and generated a classification image with 0 unclassified pixels.

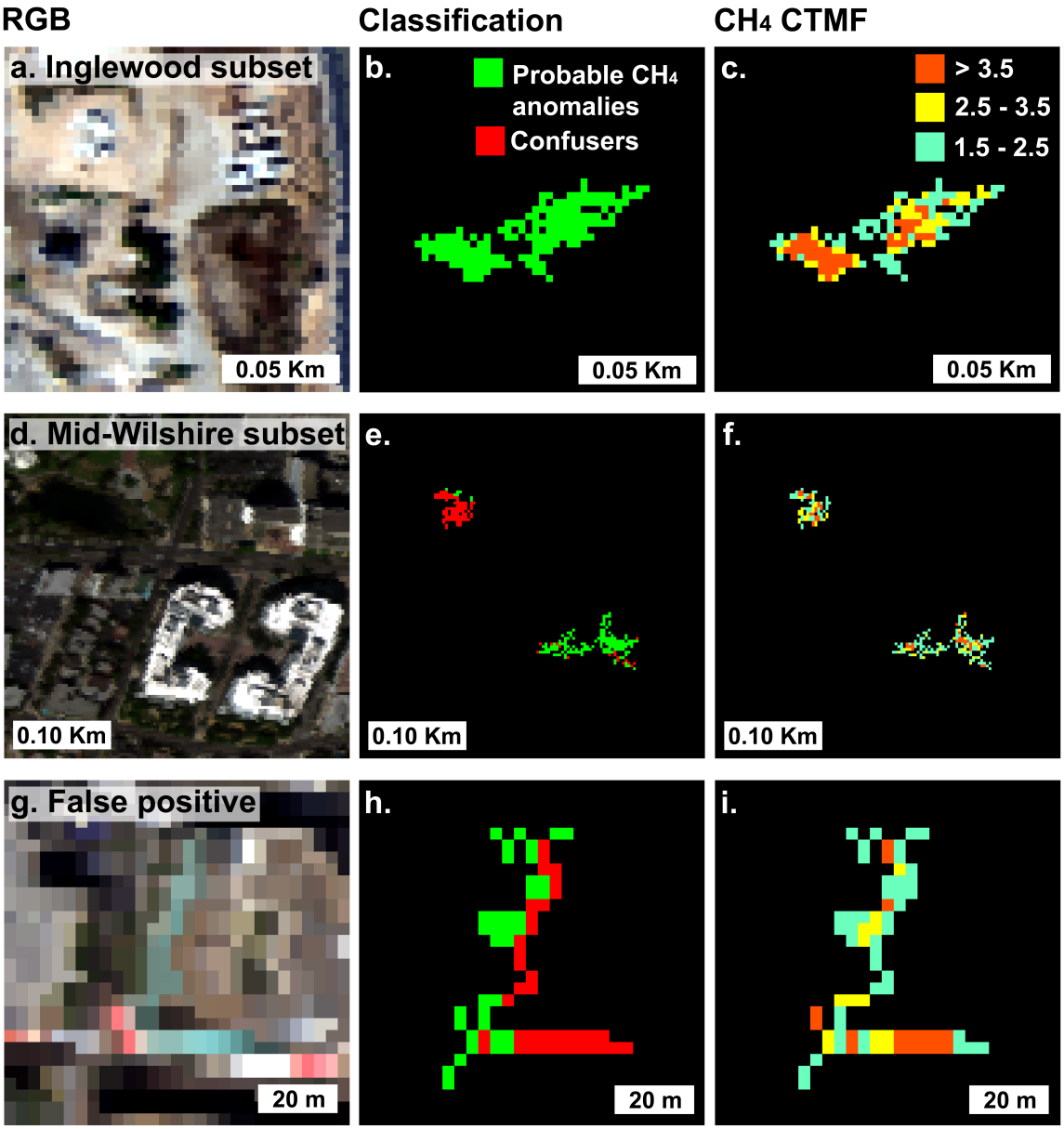

Figure 2.12. True color subsets, classification results of segmented reflectance images, and CH_4 CTMF scores are displayed for flight line r_04. (a, b, c) Inglewood subset. (d, e, f) Mid-Wilshire subset. (g, h, i) Subset with contiguous pixels classified as endmembers from the confusers class, indicating segment is a likely false positive.

The classification of the segmented reflectance image for the Inglewood subset is shown in Fig. 2.12b, with confusers indicated in red and probable CH_4 anomalies in green. This region is composed of surfaces that make up the probable CH_4 anomalies class, including soil as well as green and non-photosynthetic vegetation, while no confusers were detected. In Fig. 2.12c, CH_4 CTMF scores are displayed with highest scores in orange (greater than 3.5), intermediate values as yellow (2.5 to 3.5), and low scores in cyan (1.5 to 2.5). This indicates true CH_4 anomalies consistent with southwesterly winds and emission from or near the hydrocarbon storage tanks located at L1 in Fig. 2.8a. For reference, the original reflectance image for the same subset is included in Fig. 2.12a. For the segmented portion shown in Fig. 2.12c, surface reflectance measured at 2,100 nm had a maximum of 41.6%, minimum of 3.9%, and mean of 25.2%.

To classify the La Brea Tar Pits, it was necessary to select image endmembers directly from this location, which were included in the confusers class due to the presence of oil and tar. As a result, the anomalies at the eastern edge of the La Brea Tar Pits mostly are classified as confusers (Fig. 2.12e). Oil and fresh tar have SWIR absorption features that could cause false positives in CTMF results, however, CH_4 bubbles tens of centimeters in diameter also are present at this location. Accordingly, these anomalies are likely caused by combined absorption features resulting from CH_4 gas and liquid hydrocarbons.

Most of the courtyard anomalies appear as the probable CH_4 anomalies class and mainly include impervious surfaces like brick and pavement as well as green vegetation (Fig. 2.12e). However, confusers do exist along the edge of the heavily shaded portion of the courtyard, including calcite, asphalt, as well as green and white paint endmembers. Because the clas-

sification was limited to two endmember models, these are likely the result of mixed pixels that were misclassified as confusers. Therefore, elevated CH_4 CTMF scores in the courtyard likely represent true CH_4 anomalies and are consistent with continuous CH_4 venting by the surrounding office complex and the very elevated CH_4 concentrations up to 45.508 ppm measured at the south courtyard entrance.

For the segmented portion shown in Fig. 2.12f, surface reflectance had a maximum of 31.6%, minimum of 0.4%, and mean of 8.9% measured at 2,100 nm. Most of the anomalies at the La Brea Tar Pits occur for dark spectra (around 5% reflectance at 2,100 nm) compared to the considerably brighter surfaces that make up the courtyard. Therefore, the CTMF technique is capable of detecting CH_4 anomalies across a wide range of surface reflectance.

Fig. 2.12h provides the classification result for an image subset located approximately 1.0 km north of the La Brea Tar Pits. The confusers classification includes contiguous pixels corresponding to the blue awning in Fig. 2.12g, which likely is a painted metal surface with strong SWIR absorptions (Fig. 2.11, S4). In this example, it appears that many pixels classified as probable CH_4 anomalies may result from poor modeling of mixed pixels using two endmember models. Examining reflectance spectra adjacent to pixels classified as confusers reveals strong absorption features similar to those present in the confusers pixels. This is consistent with an edge effect caused by mixed pixels and indicates this segment is a likely false positive. In a different location, a similar edge effect was observed for mixed asphalt pixels, which systematically exhibited high CH_4 CTMF scores.

A summary of classification results of the segmented reflectance image r_04 are presented in Table 2.1. For the probable CH_4 anomalies class, the impervious land cover category made

up 460 pixels (34.56%) of the total 1,331 pixels within the segmented scene, followed by non-photosynthetic vegetation (14.05%), green vegetation (12.77%), and soil (7.14%). For the confusers class, 13.97% of the scene was of unknown composition and classified using image endmembers from the blue awning, running track, and erosion barrier. Image endmembers from the hydrocarbon/water mixture were used to classify the La Brea Tar Pits (7.66% of the scene), while the remaining land cover categories for the confusers class included oil-based paints (6.01%), calcite (3.31%), and asphalt (0.53%). Of the total 1,331 pixels within the segmented scene, 68.52% of pixels were classified as endmembers corresponding to the probable CH_4 anomalies class and 31.48% as the confusers class.

2.5 Discussion

The observed CH_4 anomalies for COP and the Mid-Wilshire neighborhood of Los Angeles suggest significant natural CH_4 seepage in these regions. COP is one of the largest natural marine seeps in the world, with total atmospheric CH_4 emissions estimated at 100,000 m^3/day (Hornafius et al. 1999). The Mid-Wilshire area has well documented CH_4 seepage, including CH_4 bubbles in the La Brea Tar Pits, CH_4 gas bubbling from between cracks in paved surfaces after rains (Gurevich et al. 1993), and additional building codes requiring CH_4 mitigation such as gas detectors in addition to active and passive venting systems (Chilingar and Endres 2005). The CTMF technique shows promise for detecting CH_4 from natural geological seepage, which contributes an estimated 30 Tg CH_4 yr^{-1} globally to the atmosphere from marine seepage (Kvenvolden and Rogers 2005) and between 20 and 40 Tg CH_4 yr^{-1} for natural terrestrial seepage (Etiope et al. 2009).

The CTMF approach also demonstrates potential for detection of fugitive CH_4 emissions,

a term describing largely unmonitored CH_4 releases associated with petroleum production and industrial processes that are poorly constrained (Howarth et al. 2011). CH_4 anomalies consistent with fugitive emissions were detected at the Inglewood Oil Field immediately downwind of two hydrocarbon storage tanks. Storage tanks are a major source of CH_4, emitting an estimated 212 Gg for the United States in 2009 (EPA 2011a). American natural gas storage tanks have an emission factor of 5.8×10^{-3} Gg CH_4 per (106) m^3 gas stored (IPCC 2000) and condensate tank batteries have been documented to emit between 141 and 14,158 m^3 natural gas and light hydrocarbon vapors each day (EPA 2010).

For the Los Angeles Basin, CH_4 emissions are poorly constrained and statewide inventories appear to underestimate urban CH_4 emissions (Wunch et al. 2009). Natural CH_4 seepage is well documented in this region (Chilingar and Endres 2005) and there are a number of potential sources of fugitive emissions. These include natural gas pipelines, the Inglewood Gas Plant, improperly sealed wells (Pipkin and Proctor 1992), the Playa del Rey Oil Field which is currently being used for natural gas storage (Chilingar and Endres 2005), as well as a number of refineries in the El Segundo neighborhood and near the Port of Long Beach. Isotopic analysis by Townsend-Small et al. (2012) indicates the majority of CH_4 emissions in Los Angeles are from fossil fuel sources, including natural seepage from geological formations as well as fugitive emissions. Therefore, the combination of airborne imaging spectrometry and the CTMF technique offers the potential to detect concentrated natural and fugitive emissions in areas where sources may be unknown or poorly quantified.

Significant CH_4 sources have been documented by Farrell et al. (2013) across much of the Los Angeles Basin, while the lowest values were located in the coastal Rancho Palos Verde

area (1.993 ppm) and at the base of the San Bernadino Mountains. All concentrations in the Los Angeles Basin were elevated compared to the Mojave Desert, where average values were 1.860 ppm. Particularly high concentrations were observed near the La Brea Tar Pits (45.508 ppm), Marina del Rey (4.740 ppm), and at the Port of Long Beach (3.676 ppm) near a number of hydrocarbon storage tanks. These high concentrations suggest that unaccounted natural CH_4 seepage and fugitive emissions in the 'bottom-up' California Air Resources Board (CARB) emissions inventory might explain some of the discrepancy between the CARB estimate of 3.0 MMT CO_2 E year^{-1} and the 'top-down' estimate of 4.2 MMT CO_2 E year^{-1} by Hsu et al. (2010).

Water vapor has absorption features in the SWIR, but cannot account for any of the observed CTMF anomalies for CH_4. In this study, CH_4 and H_2O transmittance spectra with distinct absorptions across AVIRIS bands (Fig. 2.5) were used independently to generate CTMF results for CH_4 and H_2O. Although elevated water vapor levels could be co-located with CH_4 at all locations, CTMF results for water vapor indicate no contiguous H_2O anomalies at any location within the examined AVIRIS scenes.

CTMF results included a number of false positives that resulted from surfaces with strong absorptions similar to CH_4 absorption features, including oil-based paints and calcite. False positives generally appeared as contiguous pixels with a spatial shape that mimicked an underlying surface feature, for example individual rooftops. This suggests that the AVIRIS spectral resolution limits the ability of the CTMF to accurately resolve between a pure CH_4 signature and land cover types with strong absorption features between 2,200 and 2,500 nm.

For AVIRIS scene r_04, a segmentation approach was used to reduce 'speckle' and isolate

contiguous pixels with high CTMF scores, resulting in 16 segments. By applying a MESMA classification to reflectance spectra from these segments, segments were assigned to either a probable CH_4 anomalies or confusers class. As a result, anomalies located in close proximity to hydrocarbon storage tanks and in the office courtyard were assigned as true CH_4 anomalies. Despite being classified mostly as the confusers class, anomalies at the eastern edge of the La Brea Tar Pits were likely caused by absorption features resulting from the combination of CH_4 gas, oil, and tar present at this location.

While the CTMF approach is well suited for detecting anomalies, it does not provide concentrations necessary to calculate fluxes or generate maps of gas concentrations. However, a sensitivity analysis using synthetic images and Modtran 5.3 radiative transfer simulations currently is under development to determine the relationship between CTMF scores and CH_4 concentrations as well as the minimum detectable gas concentrations. This will permit a greater understanding of the limitations of the CTMF technique, including what types of emissions might go undetected. Residual based techniques using radiative transfer simulations are also being investigated as a means of quantifying gas concentrations (Roberts et al. 2010). Evaluating the accuracy of these concentrations is an important prerequisite for creating maps of gas concentrations and estimating fluxes from individual point sources to better constrain regional emissions.

Given the high radiative forcing per CH_4 molecule and an abundance of point sources, targeting reductions in anthropogenic CH_4 is a particularly efficient means of mitigating its effects. High resolution mapping could permit emission monitoring from anthropogenic sources including wastewater treatment facilities, landfills, fossil fuel production, as well as

sources of increasing concern like fugitive CH_4 emissions from leaking natural gas pipelines (Murdock et al. 2008) and hydraulic fracturing (Howarth et al. 2011). Recently, there has been concern over possible positive feedbacks between increased surface temperature and CH_4 released at high latitudes by melting permafrost (Woodwell et al. 1998), subsea permafrost (Shakhova et al. 2010), and from CH_4 hydrate destabilization (Kvenvolden 1988). Therefore, developing remote sensing techniques to detect local emissions for terrestrial and marine environments could be particularly useful in monitoring potential increases in CH_4 emissions resulting from global warming.

2.6 Conclusions

High spatial resolution mapping of CH_4 over marine and terrestrial emission sources was performed using a CTMF technique applied to AVIRIS data. Prominent anomalies consistent with CH_4 emission from sonar-quantified seep bubble locations in the Coal Oil Point seep field were detected in addition to multiple anomalies located at known or probable emission sources in Los Angeles. The combined operations of segmentation of CTMF results followed by MESMA classification provides a means of semi-automatically discriminating between true CH_4 anomalies and false positives. Given that the CTMF results were quite consistent despite variations in input parameters, this technique is particularly well suited for application over large areas to detect CH_4 emissions from concentrated point sources.

With little modification, the CTMF algorithm could permit detection of additional greenhouse gasses with distinct absorption features, including CO_2 and N_2O (Thorpe et al. 2012; Dennison et al. 2013). The next generation AVIRIS sensor (AVIRIS-NG) should be better suited for gas detection given it has a 5 nm spectral sampling and an improved signal-to-noise ra-

tio (Hamlin et al. 2011). Further, proposed missions with AVIRIS-like sensors mounted on satellites including HyspIRI, EnMAP, Prisma, HYPXIM, and HISUI may be well-suited for detecting emissions and could greatly improve mapping of regional emissions due to its high areal coverage and potential for repeat temporal coverage.

2.7 Acknowledgments

The authors thank Joseph P. McFadden and anonymous reviewers for their insightful comments. This research was supported in part by a NASA North American Carbon Program (NACP) research grant (NNX07AC89G), a NASA California Space Grant, and the National Science Foundation, ATM Rapid Response program. AVIRIS imagery used in this study was kindly provided by the Jet Propulsion Laboratory (JPL).

Chapter 3

Retrieval techniques for airborne imaging of methane concentration using high spatial and moderate spectral resolution: Application to AVIRIS

A. K. Thorpe[1,2], C. Frankenberg[2], D. A. Roberts[1]

[1]Department of Geography, University of California, Santa Barbara, Santa Barbara, CA

[2]Jet Propulsion Laboratory, California Institute of Technology, Pasadena, CA

This chapter was published in Atmospheric Measurements Techniques and is referenced as Thorpe et al. (2014).

3.1 Abstract

Two quantitative retrieval techniques were evaluated to estimate methane (CH_4) enhancement in concentrated plumes using high spatial and moderate spectral resolution data from the Airborne Visible/Infrared Imaging Spectrometer (AVIRIS). An iterative maximum a posteriori differential optical absorption spectroscopy (IMAP-DOAS) algorithm performed well for an ocean scene containing natural CH_4 emissions from the Coal Oil Point (COP) seep field near Santa Barbara, California. IMAP-DOAS retrieval precision errors are expected to equal between 0.31 to 0.61 ppm CH_4 over the lowest atmospheric layer (height up to 1.04 km), corresponding to about a 30 to 60 ppm error for a 10 m thick plume. However, IMAP-DOAS results for a terrestrial scene were adversely influenced by the underlying land cover. A hybrid approach using singular value decomposition (SVD) was particularly effective for terrestrial surfaces because it could better account for spectral variability in surface reflectance. Using this approach, a CH_4 plume was observed extending 0.1 km downwind of two hydrocarbon storage tanks at the Inglewood Oil Field in Los Angeles, California with a maximum near surface enhancement of 8.45 ppm above background. At COP, the distinct plume had a maximum enhancement of 2.85 ppm CH_4 above background, and extended more than 1 km downwind of known seep locations. A sensitivity analysis also indicates CH_4 sensitivity should be more than doubled for the next generation AVIRIS sensor (AVIRIS-NG) due to improved spectral resolution and sampling. AVIRIS-like sensors offer the potential to better constrain emissions on local and regional scales, including sources of increasing concern like industrial point source emissions and fugitive CH_4 from the oil and gas industry.

3.2 Introduction

Atmospheric methane (CH_4) is a long-lived greenhouse gas with an instantaneous radiative forcing 21 times greater than carbon dioxide (CO_2) on a per molecule basis (IPCC 2007). In the late preindustrial Holocene (1000 to 1800 A.D.), mean concentrations were 695 ppb (Etheridge et al. 1998) and global concentrations have increased to around 1,800 ppb in 2013 (NOAA 2013). While anthropogenic sources made up an estimated 4 to 34% of pre-industrial emissions (IPCC 2007; Houweling et al. 2000), between 60 and 70% of emissions are presently anthropogenic (Lelieveld et al. 1998). Furthermore, ice core records have indicated CH_4 concentrations are closely tied to atmospheric temperature records, while present-day concentrations have not been observed for the previous 420,000 years (Wuebbles and Hayhoe 2002).

While the global CH_4 budget is relatively well constrained ($550 \pm 50\,\mathrm{Tg\,CH_4\,yr^{-1}}$), there is considerable uncertainty regarding partitioning between individual natural and anthropogenic source types and locations (IPCC 2007). Major sources of anthropogenic CH_4 emissions include the energy, industrial, agricultural, and waste management sectors. In the United States, 50% of anthropogenic CH_4 emissions are from the energy sector, including natural gas and oil systems, coal mining, and stationary/mobile combustion (EPA 2011b). Global fugitive CH_4 emissions from natural gas and oil systems are of increasing concern, estimated at 1,354.42 million metric tonnes $CO_2\,\mathrm{E\,yr^{-1}}$ ($64.50\,\mathrm{Tg\,CH_4\,yr^{-1}}$) and expected to increase 35% by 2020 (EPA 2006a). Recent studies also suggest official inventories are underestimated, for example, top-down estimates indicate fugitive CH_4 emissions are between 2.3 and 7% of CH_4 produced annually for the Denver-Julesburg Basin, Colorado (Petron et al. 2012). In the Los Angeles Basin, CH_4 emissions appear underestimated (Wunch et al. 2009)

and unaccounted sources appear to be fugitive and natural CH_4 emissions (Wennberg et al. 2012).

Significant natural CH_4 sources include wetlands, termites, and geological seeps (IPCC 2007). Globally, geological seeps are highly uncertain but estimated to contribute between 20 to 40 Tg CH_4 yr^{-1} for terrestrial environments (Etiope et al. 2009) and about 40 Tg CH_4 yr^{-1} for marine seepage (Kvenvolden and Rogers 2005). In addition, increased surface and ocean temperatures associated with global warming may increase CH_4 emissions from melting permafrost (Woodwell et al. 1998) and CH_4 hydrate destabilization (Kvenvolden 1988).

3.3 Airborne measurements of methane

Aircraft measurements of gas concentrations are useful because they offer the potential to measure local/regional variations in gas concentrations and complement ongoing efforts at coarser spatial resolutions, such as spaceborne sensors. These airborne measurements can improve greenhouse gas emissions inventories and offer the potential for detection and monitoring of emissions (NRC 2010).

Research and commercial aircraft equipped with in situ gas measurement provides some sense of CH_4 variability at local and regional scales (ARCTAS 2010; Schuck et al. 2012). The nadir-viewing Fourier transform spectrometer (FTS) included as part of the NASA Carbon in Arctic Reservoirs Vulnerability Experiment (CARVE) (Miller and Dinardo 2012) and spectrometers like MAMAP (Methane Airborne MAPper) (Gerilowski et al. 2011) also offer the potential to measure local emissions. For example, MAMAP detected elevated CH_4 concentrations from coal mine ventilation shafts near Ibbenbüren, Germany, allowing for an inversion estimate that agreed closely with emission rates reported from mine operators (Krings

et al. 2013). However, these non-imaging spectrometers have a small field of view (FOV) and are limited to flying transects across local gas plumes rather than mapping plumes in their entirety.

By combining large image footprints and fine spatial resolution, airborne imaging spectrometers are well suited for mapping local CH_4 plumes. The Airborne Visible/Infrared Imaging Spectrometer (AVIRIS) has a 34° FOV and measures reflected solar radiance at the nadir viewing geometry across 224 channels between 350 and 2,500 nm (Green et al. 1998). Strong CH_4 absorption features present between 2,000 and 2,500 nm can be observed at a 10 nm spectral resolution and full width half maximum (FWHM). These absorptions are clearly shown in Fig. 3.1a by transmittance spectra calculated for CH_4 using Modtran 5.3 (Berk et al. 1989), parameterized for a mid-latitude summer model atmosphere and nadir-looking sensor at 8.9 km altitude. High resolution transmittance is shown in red in Fig. 3.1a and convolved to AVIRIS wavelengths in Fig. 3.1b, while water vapor (H_2O) transmittance has been included in blue to indicate spectral overlap with CH_4.

These shortwave infrared (SWIR) absorptions have permitted mapping of concentrated gas plumes in both marine and terrestrial environments using AVIRIS. For bright sun glint scenes at the Coal Oil Point (COP) marine seep field in the Santa Barbara Channel, California, Roberts et al. (2010) developed a spectral residual approach between 2,000 and 2,500 nm and Bradley et al. (2011) a band ratio technique using the 2,298 nm CH_4 absorption band and 2,058 nm carbon dioxide (CO_2) absorption band. However, these techniques are not suited for terrestrial locations that have lower albedos and have spectral structure in the SWIR. A Cluster-Tuned Matched Filter (CTMF) technique is capable of mapping CH_4 plumes from ma-

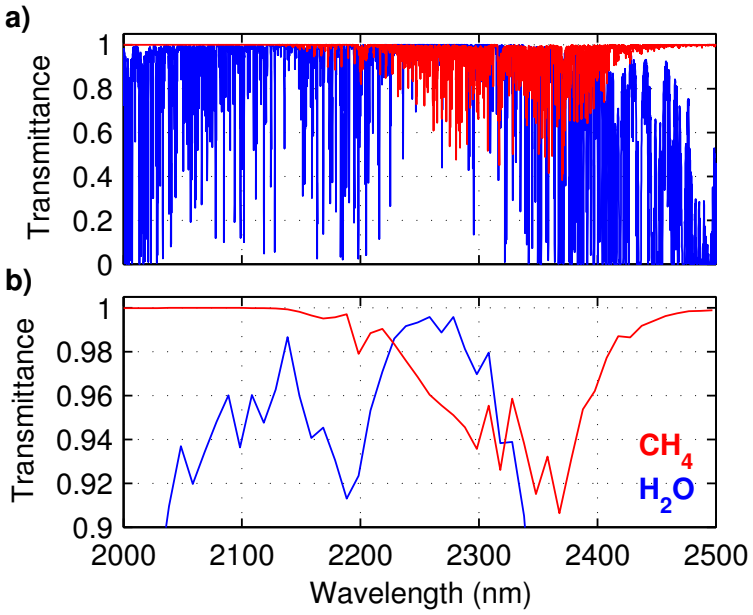

Figure 3.1. (a) High resolution CH_4 and H_2O transmittance. (b) Transmittance convolved to the 10 nm AVIRIS spectral resolution.

rine and terrestrial sources (Thorpe et al. 2013) as well as CO_2 from power plants (Dennison et al. 2013); however, this method does not directly quantify gas concentrations.

The logical next step is to focus on quantification and uncertainty estimation using techniques originally developed for satellite sensors such as differential optical absorption spectroscopy (DOAS) (Platt 1994). In this study, an iterative maximum a posteriori differential optical absorption spectroscopy (IMAP-DOAS) (Frankenberg et al. 2005b) algorithm was adapted for gas detection in AVIRIS imagery. In addition, a hybrid approach using singular value decomposition (SVD) and IMAP-DOAS was also developed as a complementary method of quantifying gas concentrations within complex AVIRIS scenes.

3.4 Basic principles of IMAP-DOAS

Retrieval algorithms for absorbing species in the SWIR require radiative transfer modeling of solar radiation along the light path to the sensor and must be capable of simulating changes

in radiation due to differing abundances of absorbers. These techniques permit comparison of simulated at sensor radiance with a known abundance of absorbers with measured radiance provided by the sensor. Differential optical absorption spectroscopy (DOAS) (Platt 1994) is one approach that has been used for a number of applications, including ground-based (Stutz et al. 2010), satellite (Schneising et al. 2012), and airborne measurement (Gerilowski et al. 2011). The underlying principle of DOAS is to isolate higher frequency features resulting from gas absorptions from lower frequency features that include surface reflectance as well as Rayleigh and Mie scattering (Bovensmann et al. 2011). To do so, a polynomial function accounting for low-frequency features is often used, which is described in further detail in Sect. 3.6.

Classical DOAS (Platt 1994) is based on the Lambert–Beer law and describes the relationship between incident intensity for the vertical column ($I_0(v)$) and measured intensity ($I(v)$) after passing through a light path (ds) containing an absorber:

$$I(v) = I_0(v) \cdot \exp\left(-\int \sigma(v,p,T)\, c(s)\, \mathrm{d}s\right) \tag{3.1}$$

Each absorber has an associated absorption cross section (σ) and number concentration of the absorber ($c(s)$, molecules m^{-3}). Eq. 3.1 is wavelength dependent and the absorption cross section varies with temperature (T) and pressure (p). If the atmospheric absorption features are fully resolved by the instrument and only weak absorbers are present, Eq. 3.1 can be linearized with respect to slant column density S:

$$\begin{aligned} \boldsymbol{\tau} &= \ln\left(\frac{I_0(v)}{I(v)}\right) \approx \sigma\left(v, \bar{p}, \bar{T}\right) \cdot \int c(s)\, \mathrm{d}s \\ &= \sigma(v,p,T) \cdot S \end{aligned} \tag{3.2}$$

where measured optical density ($\boldsymbol{\tau}$) is proportional to the product of the absorption cross section and the retrieved S, the path integral of the concentration of the absorber along the light path. S is related to the vertical column density (V), the integral of the concentration along the vertical from the surface to the top of atmosphere, by way of the air mass factor (A), where $A = S/V$. In the SWIR, scattering in the atmosphere is generally low (Buchwitz and Burrows 2003; Dufour and Breon 2003) and for our applications, the impact of scattering is far lower than the retrieval precision error. Thus, it can be neglected and $A = 1/\cos(\text{SZA}) + 1/\cos(\text{LZA})$, where SZA is the solar zenith angle and LZA is the line-of-sight zenith angle. However, scattering could become non-negligible in some examples, including industrial plumes that contain heavy aerosol loading or dark surfaces with low SZA.

For a single absorber measured with a moderate spectral resolution and ignoring scattering, a theoretical slant optical density ($\boldsymbol{\tau}_\lambda^{\text{meas}}$) can be calculated as follows:

$$\boldsymbol{\tau}_\lambda^{\text{meas}}(x) = -\ln\left(< \exp\left(-x \cdot A \cdot \boldsymbol{\tau}_\lambda^{\text{ref}}\right) >\right) \tag{3.3}$$

where the reference vertical optical density ($\boldsymbol{\tau}_\lambda^{\text{ref}}$) is scaled by both the air mass factor (A) as well as a retrieved scaling factor (x) and $< \cdot >$ denotes convolution with the instrument function. In addition to scaling $\boldsymbol{\tau}_\lambda^{\text{meas}}$, x can be used to estimate gas concentrations relative to those concentrations present within the reference atmosphere.

However, moderate spectral resolution spectrometers cannot fully resolve individual absorption lines and must convolve light using an instrument line shape (ILS) function wider than individual absorption lines. If absorptions are strong, this results in a nonlinear relationship between the measured optical density ($\boldsymbol{\tau}$) and the retrieved slant column density of

the absorber (S) shown in Eq. 3.2 (Frankenberg et al. 2005b). In the 2,300 nm region, strong H_2O and CH_4 absorption lines are saturated within their line cores. These factors render Eq. 3.2 nonlinear and cause classical DOAS algorithms to fail, requiring iterative procedures to account for the induced nonlinearity.

To address the strong sensitivity of the shape of spectral absorption lines to temperature and pressure as well as unresolved absorption lines (Platt and Stutz 2008), the weighting function modified differential optical absorption spectroscopy (WFM-DOAS) retrieval algorithm was developed (Buchwitz et al. 2000). WFM-DOAS introduced weighting functions to linearize the problem of a linearization point in the expected slant column density using vertical profiles of all absorbers as well as pressure and temperature profiles. It has been used to estimate column amounts of CO (carbon monoxide), CO_2, and CH_4 using Scanning Imaging Absorption Spectrometer for Atmospheric Chartography (SCIAMACHY) data, which have a spectral resolution between 0.2 and 1.5 nm (Buchwitz et al. 2005b). A modified WFM-DOAS algorithm is used with the airborne MAMAP, which has a SWIR grating spectrometer for measuring CH_4 and CO_2 absorptions between 1,590 and 1,690 nm with a 0.82 nm FWHM (Gerilowski et al. 2011). In addition to detecting elevated CH_4 concentrations from coal mines (Krings et al. 2013), MAMAP has been used to measure both CH_4 and CO_2 emissions from power plants (Krings et al. 2011).

Frankenberg et al. (2005b) developed the IMAP-DOAS algorithm, which uses optimal estimation theory to adjust the slant column densities of multiple gasses until total optical density fits the observed measurement. IMAP-DOAS considers the shape of the spectral absorption lines, as they vary with temperature and pressure in multiple atmospheric layers,

and convolves absorption lines using the instrument line shape function. This technique is based on a simple non-scattering radiative transfer scheme, which allows very fast retrievals and is well suited for processing of AVIRIS imagery. For the 2,300 nm range, where Rayleigh scattering can be ignored and aerosol optical depths are low, this assumption in IMAP-DOAS is valid, given errors induced by neglected scattering in AVIRIS scene are typically much lower (0 to 2%) than precision errors in retrieved column estimates (>3%). Additional details of the IMAP-DOAS algorithm and retrieval method are presented in Sect. 3.6.

While IMAP-DOAS has been used with SCIAMACHY data to estimate global column-averaged mixing ratios for CH_4 (Frankenberg et al. 2005a, 2011) and CO (Frankenberg et al. 2005c), this study is the first to use aircraft measurements. Moderate resolution spectrometers like AVIRIS require large fitting windows, and disentangling surface spectral features from atmospheric absorptions becomes more complicated using fitting routines such as WFM-DOAS and IMAP-DOAS. High resolution spectrometers can circumvent this problem since atmospheric absorption lines are narrow and surface properties, which vary on a scale greater than 5 to 10 nm, can be fitted using polynomial functions. In this case, reflectance spectra of terrestrial surfaces (not including narrow atmospheric features) can usually be represented by a low order polynomial as a function of wavelength. For the 10 nm spectral resolution and FWHM of AVIRIS, distinguishing surface features from atmospheric absorptions will be more difficult. Therefore, we developed an alternative hybrid approach using both IMAP-DOAS and SVD of surface reflectance properties at background CH_4 concentrations.

3.5 Study sites and AVIRIS data

Two AVIRIS scenes were used in this study, both acquired in California in 2008. The first scene was acquired over the COP marine seep field near Santa Barbara from an 8.9 km altitude, resulting in an image swath of ~5.4 km and a ground instantaneous field of view (IFOV) of ~7.5 m. The scene was acquired on 19 June 2008 at approximately 19:55 UTC (12:55 PDT) with a 11.4° solar zenith resulting in high sun glint. COP is one of the largest natural seeps with total atmospheric CH_4 emissions estimated at 100,000 m^3 day^{-1} (0.024 Tg CH_4 yr^{-1}) (Hornafius et al. 1999). A 308 by 191 pixel image subset was used for the IMAP-DOAS and SVD algorithms, covering 3.31 km^2 centered on the COP seep field (34°23′46.59″ N, 119°52′4.47″ W).

The second scene covered the Inglewood Oil Field, located in Los Angeles in an area that has active oil and gas extraction (DOGGR 2010b). The AVIRIS scene was acquired at approximately 21:12 UTC (14:12 PDT) on 18 September 2008 at 4.0 km altitude, resulting in a swath width of ~2.7 km, ground IFOV of ~3 m, and a 38.1° solar zenith. For this scene, a 161 by 172 pixel image subset (0.25 km^2 centered at 33° 59′28.68″ N, 118°21′34.59″ W) was selected because it contains a CH_4 plume detected using a CTMF technique, with hydrocarbon storage tanks as a probable emission source (Thorpe et al. 2013).

3.6 IMAP-DOAS retrieval method

The IMAP-DOAS retrieval relies on layer optical properties of absorbing species calculated for a realistic temperature/pressure and trace gas concentration profile for a given location. In addition, instrument line shape and flight parameters are used with geometric radiative transfer calculations to simulate at-sensor radiances and Jacobians with respect to trace gas abundances for each atmospheric layer. In the following, we describe input parameters

and additional details of the IMAP-DOAS retrieval.

3.6.1 IMAP-DOAS input parameters

For the two 2008 AVIRIS scenes, temperature, pressure, and H_2O volume mixing ratio (VMR) profiles acquired from the National Centers for Environmental Prediction/National Center for Atmospheric Research (NCEP/NCAR) Reanalysis project were extracted for the appropriate date and time for either location (Kalnay et al. 1996). The NCEP data are provided on a 2.5° latitude × 2.5° longitude grid every 6 h with 17 pressure levels between 10 and 1,000 mb. Prior profiles of CH_4 and N_2O are based on the U.S. standard atmosphere obtained from the radiative transfer models LOWTRAN/MODTRAN (Kneizys et al. 1996). These profiles were scaled to reflect the VMR for CH_4 and N_2O using the 2008 mean VMR provided from the NOAA Mauna Loa station, United States (NOAA 2013). For both gasses, the percent increase of the 2008 mean VMR compared to the U.S. standard atmosphere at 0 km altitude was calculated and used to update the VMR up to 25 km altitude. Finally, we computed vertical optical depths for 10 atmospheric layers at 100 mb intervals between 0 and 1,000 mb.

For AVIRIS, the strongest CH_4 absorptions occur between 2,200 to 2,400 nm (Fig. 3.1). Spectral parameters for CH_4, H_2O, and N_2O were used from the HITRAN database (Rothman et al. 2009). We used a classical Voigt spectral line shape to calculate CH_4, H_2O, and N_2O vertical optical densities for each of the 10 atmospheric layers.

Given that the two AVIRIS scenes were acquired at different flight altitudes and SZA, geometric air mass factors (AMF) had to be calculated for each of the 10 layers to account for either one- (above sensor) or two-way (below sensor) transmission through each layer. For example, the COP flight was at 8.9 km altitude with a solar zenith angle of 11.4°, placing

the aircraft approximately at the boundary between atmospheric layer 3 and 4 (Fig. 3.2). In this simplified setup, the AMF for layers 1 to 3 (above the aircraft) is calculated as $1/\cos(11.4°) = 1.02$, while for layers 4 to 10, an AMF of 2.02 ($1/\cos(11.4°) + 1/\cos(0.0°)$) accounts for two-way transmission. Similar calculations were performed for the Los Angeles scene, which was acquired with a SZA of 38.1° at 4.0 km altitude, placing the aircraft approximately at the boundary between layer 5 and 6.

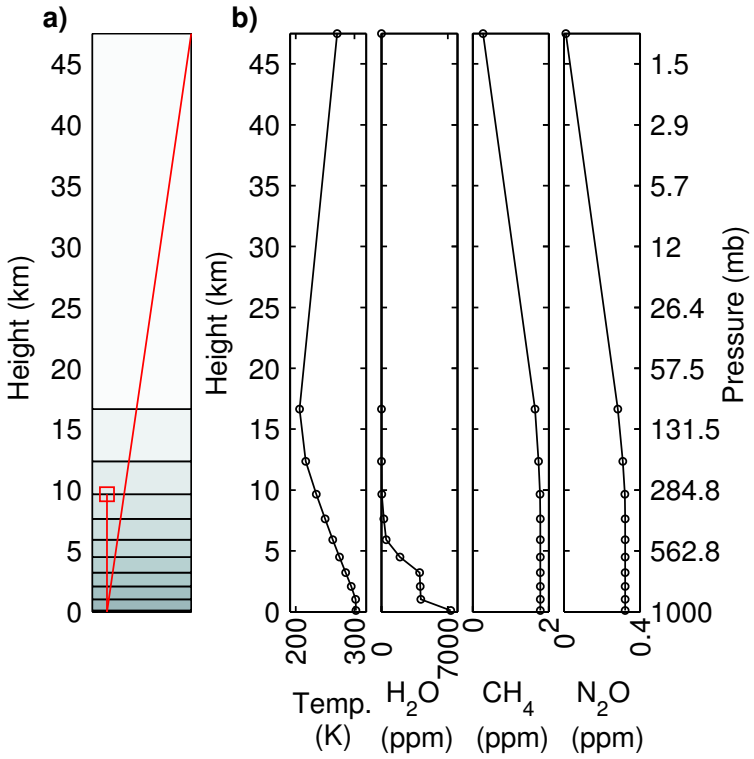

Figure 3.2. (a) 10 atmospheric layers were used for retrievals (layer 1 at the top). For the COP scene, the aircraft was placed between layer 3 and 4 (red square). The slant and vertical light paths (red lines) were used to scale optical densities appropriately. (b) Profiles of temperature and VMR of H_2O, CH_4, and N_2O for the boundaries of each layer (black circles).

Additional input parameters for the IMAP-DOAS algorithm are shown in Fig. 3.3, including the AVIRIS radiance data, spectral resolution of the sensor, signal-to-noise ratio (SNR) estimate, and the full width at half maximum of the instrument lineshape (FWHM = 10.42 nm,

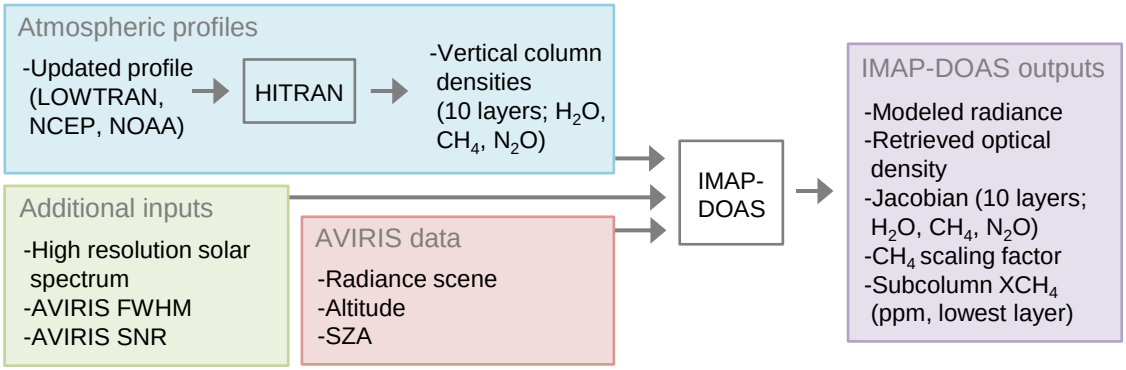

Figure 3.3. Processing steps for IMAP-DOAS CH_4 retrieval.

assuming a Gaussian line-shape). An average FWHM and an average SNR were calculated for bands included within the fitting window, while the high resolution solar transmission spectrum was generated using a solar line list (Geoffrey Toon, personal communication, 2013).

The optimal choice of a fitting window for the IMAP-DOAS CH_4 retrievals was determined iteratively. We began using all spectral bands between 2,100 and 2,500 nm corresponding to strong CH_4 absorptions, but observed strong correlations with surface features. This is likely related to spectrally smooth convolved transmissions from 2,200 to 2,300 nm and above 2,370 nm. As we decreased the size of the fitting window to focus on the more high-frequency CH_4 features, the spectral variability associated with AVIRIS bands at either end of the fitting window was reduced and results improved. The fitting window selected for this study used 9 bands between 2,278 and 2,358 nm, including three prominent absorption features visible in CH_4 Jacobians shown in Fig. 3.4a.

3.6.2 Forward model and optimal estimation

Using 10 atmospheric layers and the gasses CH_4, H_2O, and N_2O results in a state vector with 30 rows ($\vec{x}_n$). A forward radiative transfer model at high spectral resolution was used

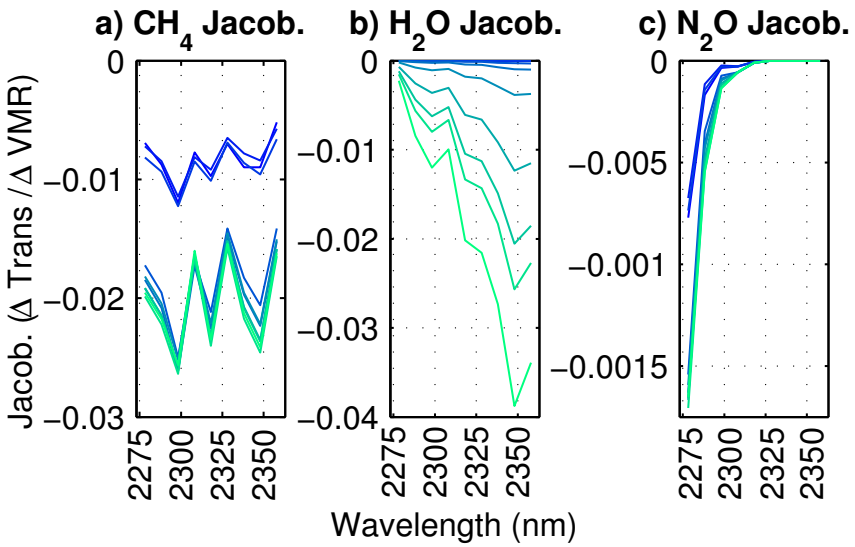

Figure 3.4. (a) CH_4 Jacobian for each of the 10 atmospheric layers with colors transitioning from dark blue at the highest layer (layer 1) to light green for the lowest layer (layer 10). The CH_4 Jacobians with smaller magnitudes (dark blue) are for layers above the flight altitude. The same color scheme is used for the H_2O Jacobians (b) and N_2O Jacobians (c).

to calculate modeled radiance at each wavelength using the equation below:

$$\vec{F}^{\text{hr}}(\vec{x}_i) = \vec{I}_0^{\text{hr}} \cdot \exp\left(-\sum_{n=1}^{30} \vec{A}_n \cdot \boldsymbol{\tau}_n^{\text{ref}} \cdot \vec{x}_{n,i}\right) \cdot \sum_{i=0}^{k} a_k \lambda^k \tag{3.4}$$

where $\vec{F}^{\text{hr}}(\vec{x}_i)$ is the forward modeled radiance at the ith iteration of the state vector, $\vec{I}_0^{\text{hr}}$ is the incident intensity (solar transmission spectrum), $\vec{A}_n$ is the AMF for each n number of atmospheric state vector elements (30 rows, specified for each of the 10 layers and repeated for each gas), $\boldsymbol{\tau}_n^{\text{ref}}$ is the reference total optical density for each n number of atmospheric state vector elements (including optical densities of CH_4, H_2O, and N_2O), $\vec{x}_{n,i}$ is the trace gas related state vector at the ith iteration, which scales the prior optical densities of CH_4, H_2O, and N_2O in each n layer (30 rows), a_k are polynomial coefficients to account for low-frequency spectral variations.

The high resolution modeled radiance is then convolved with the ILS and sampled to the center wavelengths of each AVIRIS spectral band. This results in a low resolution modeled

radiance at the ith iteration of the state vector ($\vec{F}^{\mathrm{lr}}(\vec{x}_i)$), calculated using a known $\boldsymbol{\tau}_n^{\mathrm{ref}}$ scaled by $\vec{x}_{n,i}$.

In addition to the scaling factors for CH_4, H_2O, and N_2O in each n layers ($\vec{x}_n$), the state vector contains the spectral shift (not shown here) as well as a low order polynomial function (a_k) to account for the broadband variability in surface albedo (see Frankenberg et al. 2005b).

At each iteration i, a Jacobian matrix is calculated where each column represents the derivative vector of the sensor radiance with respect to each element of the state vector ($\vec{x}_i$).

$$\mathbf{K}_i = \left.\frac{\partial \vec{F}^{\mathrm{lr}}(\vec{x})}{\partial \vec{x}}\right|_{\vec{x}_i} \tag{3.5}$$

The forward model and the Jacobian Matrix can be used to optimize the state vector at the ith iteration as follows (Rodgers 2000):

$$\begin{aligned}\vec{x}_{i+1} = \vec{x}_{\mathrm{a}} + \left(\mathbf{K}_i^T \mathbf{S}_\varepsilon^{-1} \mathbf{K}_i + \mathbf{S}_{\mathrm{a}}^{-1}\right)^{-1} \mathbf{K}_i^T \mathbf{S}_\varepsilon^{-1} \\ \cdot \left[\vec{y} - \vec{F}^{\mathrm{lr}}(\vec{x}_i) + \mathbf{K}_i(\vec{x}_i - \vec{x}_{\mathrm{a}})\right]\end{aligned} \tag{3.6}$$

where $\vec{x}_{\mathrm{a}}$ is the a priori state vector (30 rows), $\vec{x}_i$ is the state vector at the ith iteration (30 rows), $\mathbf{S}_\varepsilon$ is the error covariance matrix, $\mathbf{S}_{\mathrm{a}}$ is the a priori covariance matrix, $\vec{y}$ is the measured AVIRIS radiance, $\vec{F}^{\mathrm{lr}}(\vec{x}_i)$ is the forward model evaluated at $\vec{x}_i$, and $\mathbf{K}_i$ is the Jacobian of the forward model at $\vec{x}_i$.

The a priori state vector was set to 1 for each gas at each layer, while the a priori covariance matrix was set to constrain the fit to the lowest atmospheric layer (height up to 1.04 km) where high variance is expected. To achieve this, very tight prior covariances were set for all atmospheric layers except the lowermost one, which is basically unconstrained. This assumption is reasonable given that the COP and Inglewood scenes contain CH_4 emission from

ground sources that are not expected to extend above this atmospheric layer. CH_4 concentrations were calculated by multiplying the CH_4 state vector at the last iteration (CH_4 scaling factor) by the VMR for the lowest layer of the reference atmosphere (Fig. 3.2).

3.7 Basic principles of SVD

SVD transforms a large number of potentially correlated vectors into a smaller set of uncorrelated (orthogonal) vectors, denoted as singular vectors (Press et al. 2007; Rodgers 2000). It is closely related to principal component analysis (PCA) and offers the potential for reduced computation time by efficiently summarizing high dimensional data. It has been used in a number of remote sensing applications, including cloud detection using the Michelson Interferometer for Passive Atmospheric Sounding (MIPAS) (Hurley et al. 2009), retrieving aerosol optical densities of mineral dust using the Infrared Atmospheric Sounding Interferometer (IASI), and retrieval of terrestrial chlorophyll fluorescence using the Fourier Transform Spectrometer (FTS) on board the Greenhouse gases Observing SATellite (GOSAT) platform (Guanter et al. 2012).

For this study, we constructed an $m \times n$ matrix $\mathbf{L}$, where m is the number of spectral bands (for the CH_4 fit window) and n is the number of radiance spectra in a specific AVIRIS scene. This can be expressed as

$$\mathbf{L} = \mathbf{U}\boldsymbol{\Lambda}\mathbf{V}^T \tag{3.7}$$

where the $m \times m$ matrix $\mathbf{U}$ contains the left singular vectors and the $n \times n$ matrix $\mathbf{V}$ contains the right singular vectors in their respective columns. $\boldsymbol{\Lambda}$ is an $m \times n$ rectangular diagonal matrix containing the m singular values of $\mathbf{L}$ on its diagonal. These singular values are essentially eigenvalues that correspond to the m columns of $\mathbf{U}$, which are analogous to eigenvectors.

Each of the n columns of $\mathbf{V}$ is essentially a principal component of the scene, with each successive column capturing increasingly less signal variability. Therefore, $\mathbf{L}$ can be recomposed as a linear combination of singular vectors scaled by the singular values (Murtagh and Heck 1987).

3.8 SVD retrieval method

For each AVIRIS image subset, the radiance scene was first standardized by fitting a first order polynomial to each radiance spectrum and dividing it by the polynomial fit. Next, a mean radiance spectrum was calculated from the standardized data and the IMAP-DOAS retrieval was performed on the mean spectrum to generate the CH_4 Jacobian for the lowest layer ($\mathbf{K}_{CH_4}$) (Fig. 3.5). This standardization was performed to ensure that the computed CH_4 Jacobian is representative for all pixels; without it, calculations of Jacobians for each continuum level would be required. As an alternative to standardization, a SVD in log-space could be considered since optical depths are linear with respect to changing concentrations in the vicinity of the linearization point.

Using Eq. 3.7, the SVD was performed on each image subset using the standardized radiance ($m \times n$ matrix $\mathbf{L}$, where m is the number of spectral bands and n is the number of radiance spectra). Due to computing limitations, the economy version of the SVD was calculated using MATLAB (Mathworks, Natick, Massachusetts, USA). This resulted in $\mathbf{U}_{\text{econ}}$ maintaining a dimension of $m \times m$ (left singular vectors in m columns), but reduced matrix dimensions for $\mathbf{V}_{\text{econ}}$ and $\boldsymbol{\Lambda}_{\text{econ}}$ ($n \times m$ and $m \times m$, respectively).

The first c columns of $\mathbf{U}_{\text{econ}}$ ($\mathbf{U}_{\text{select}}$, an $m \times c$ matrix where the optimal selection of c is described below) and the CH_4 Jacobian ($\mathbf{K}_{CH_4}$, an $m \times 1$ matrix) are concatenated to generate

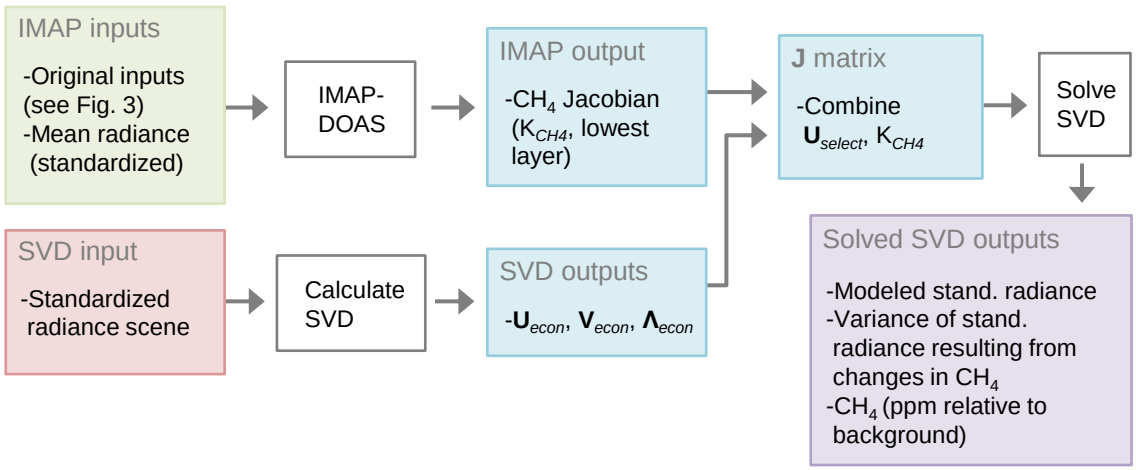

Figure 3.5. Processing steps for the SVD retrieval method. The IMAP-DOAS retrieval is performed on a mean radiance for the image subset to generate the CH_4 Jacobian for the lowest layer. The SVD is used to calculate $\mathbf{U}_{\text{econ}}$, $\mathbf{V}_{\text{econ}}$, and $\boldsymbol{\Lambda}_{\text{econ}}$, while $\mathbf{U}_{\text{select}}$ is combined with the CH_4 Jacobian to generate the $\mathbf{J}$ matrix. $\mathbf{J}$ is used to determine the portion of each radiance spectra associated with the CH_4 Jacobian (i.e., absorptions due to CH_4) and can be used to estimate CH_4 concentrations.

a matrix $\mathbf{J}$ (dimensions of $m \times c+1$). The basic principle is to reflect the general variability in spectral radiances by a linear combination of the first c eigenvectors and the CH_4 Jacobian, which relates to deviations from background concentrations since the background radiance is already modeled using the linear combination of eigenvectors. A similar technique was used to retrieve terrestrial chlorophyll fluorescence using the FTS on board GOSAT (Guanter et al. 2012). The linear combination of eigenvectors is an empirical way to compute the forward model radiance, which can include many detector and surface albedo features that the IMAP-DOAS approach cannot easily handle.

Using linear least squares, we can now find a vector $\vec{W}$ that minimizes the cost function involving the measured radiance spectra $\vec{y}$:

$$\left|\left|\vec{y} - \mathbf{J}\vec{W}\right|\right|^2 \tag{3.8}$$

$\vec{W}$ represents the contribution of each column of $\mathbf{J}$ to the measured radiance. The modeled

radiance $\vec{F}$ can be calculated by multiplying $\mathbf{J}$ by the weights $\vec{W}$:

$$\vec{F} = \mathbf{J}\vec{W} \tag{3.9}$$

resulting in a modeled radiance that can be compared to the measured radiance for each spectrum.

The previous equation can be rewritten as the sum of the background and CH_4 component of the radiance as follows:

$$\vec{F}\left(\vec{W}, \mathbf{J}\right) = \sum_{k=1}^{c} \mathbf{J}_k \cdot \vec{W}_k + \mathbf{J}_{c+1} \cdot \vec{W}_{c+1} \tag{3.10}$$

where the left term represents the background radiance modeled as a linear combination of the first c eigenvectors of $\mathbf{J}$ ($\mathbf{J}_k$) multiplied by the corresponding weights $\vec{W}_k$. The right term is the CH_4 component of the scene, the product of $\mathbf{J}_{c+1}$ (the CH_4 Jacobian, $\mathbf{K}_{CH_4}$) and its corresponding weight $\vec{W}_{c+1}$ (denoted as RCH_4). In Eq. 3.10, the fit coefficients are c and $\vec{W}$. RCH_4 indicates how much of the observed radiance for each spectrum can be associated with the CH_4 Jacobian (i.e., changes in absorptions due to CH_4) and can be used to both estimate CH_4 concentrations as well as its uncertainties. Similar to the IMAP-DOAS approach, RCH_4 for each pixel is multiplied by the VMR for the lowest layer of the reference atmosphere and results in an estimated CH_4 concentration in ppm above/below the average.

The same 9 bands between 2,278 and 2,358 nm that made up the IMAP-DOAS retrieval window were initially used for the hybrid SVD approach. In an iterative process, additional bands between 2,218 and 2,457 nm were included to better account for high-frequency variation present in the scenes. A portion of the scene was selected for a homogeneous land cover and the standard deviation of the RCH_4 results for different fitting windows was calculated.

A 16-band fitting window (2,278 to 2,428 nm) was selected because it produced the lowest standard deviation in RCH_4 and thereby minimized noise in results.

Using these 16 bands, the hybrid SVD retrieval was performed iteratively by increasing the c columns of $\mathbf{U}_{\text{econ}}$ used to generate $\mathbf{U}_{\text{select}}$. This resulted in 16 SVD retrievals, which were assessed by minimizing the standard deviation of the RCH_4 results for the portion of the scene selected to represent homogeneous land cover. This technique was used to determine the optimal number of columns of $\mathbf{U}_{\text{econ}}$ to use with the SVD retrieval for the COP and Inglewood scenes.

3.9 Results for IMAP-DOAS sensitivity study

To investigate the expected IMAP-DOAS retrieval errors for the 9-band fitting window between 2,278 and 2,358 nm, the covariance $\hat{S}$ was calculated using the following equation:

$$\hat{S} = \left(\mathbf{K}^T \mathbf{S}_{\varepsilon}^{-1} \mathbf{K} + \mathbf{S}_{\text{a}}^{-1}\right)^{-1} \tag{3.11}$$

where the diagonal of $\hat{S}$ corresponds to the covariance associated with CH_4, H_2O, and N_2O at each of the 10 atmospheric layers. $\mathbf{S}_{\varepsilon}$ is the error covariance matrix, a diagonal matrix representing expected errors resulting from shot-noise and dark current that is calculated using the SNR for the AVIRIS sensor.

The precision error of the IMAP-DOAS retrieval algorithm is calculated by multiplying the square root of the corresponding diagonal entry of $\hat{S}$ (the standard deviation of the CH_4 fit factor) by 1.78 ppm CH_4, the 2008 mean VMR provided from the NOAA Mauna Loa station, United States (NOAA 2013). These errors were calculated for a number of hypothetical sensors with varying spectral resolution and FWHM across a range of SNR (Fig. 3.6). As expected, the IMAP-DOAS error decreases as SNR increases and as the spectral resolution and

FWHM become finer. The black line (10 nm spectral resolution and FWHM) approximates the AVIRIS sensor and the SNR for bands used in the IMAP-DOAS retrieval was conservatively estimated between 100 and 200 using an AVIRIS instrument model for low albedo surfaces (Robert Green, personal communication, 2013). Using scene parameters similar to the COP flight (8.9 km altitude, 11.4° solar zenith), this corresponds to an error of between 0.31 to 0.61 ppm CH_4 over the lowest atmospheric layer (up to 1.04 km) shown in Fig. 3.2a. Given that about 10% of the total column is within the lowest layer, this error is considerable and roughly corresponds to an error of 30 to 60 ppb in column-averaged CH_4 over the total atmospheric column.

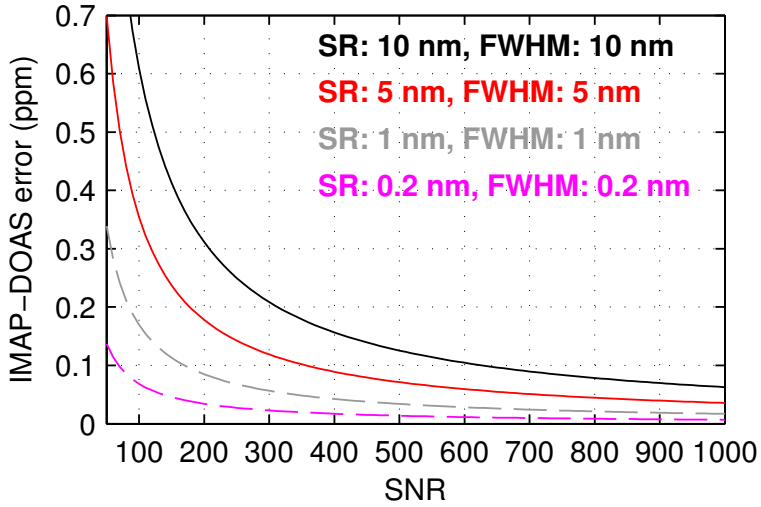

Figure 3.6. Estimated IMAP-DOAS retrieval errors (ppm CH_4) for four hypothetical sensors, each with the spectral resolution (SR) equal to the FWHM. Errors are relative to lowest atmospheric layer (height up to 1.04 km) and decline with increased signal-to-noise ratio (SNR).

3.10 Results for IMAP-DOAS

3.10.1 COP

For the COP subset shown in Fig. 3.7a, measured radiance for the first band of the IMAP-DOAS retrieval window at 2,278 nm had a minimum of 0.1158, maximum of 6.436 (sensor

saturation), and mean of $2.0516\,\mu W cm^{-2} sr^{-1} nm^{-1}$. Sensor saturation occurs only for a small portion of the scene where the full well of the detector is saturated for multiple channels in the SWIR. Sonar return contours of subsurface CH_4 bubble plumes are overlain and correspond to known seep locations (Leifer et al. 2010). In Fig. 3.7b, the CH_4 scaling factor is shown for the lowest atmospheric layer (height up to 1.04 km) and a CH_4 enhancement is clearly visible, consistent with emission from seep locations and the $2.3\,m\,s^{-1}$ southwesterly wind measured at the nearby West Campus Station. The standard deviation of the residual (the difference between measured and modeled radiance) was also calculated to evaluate the ability of IMAP-DOAS to model radiance. This result is shown in Fig. 3.7c and has a similar visual appearance to Fig. 3.7a, indicating a strong albedo influence.

CH_4 concentrations were calculated by multiplying the retrieved CH_4 scaling factor by the VMR for the lowest atmospheric layer (1.78 ppm CH_4). In Fig. 3.7d, ppm CH_4 for the lowest layer is shown (subcolumn XCH_4), excluding 740 bright pixels (greater than $5\,\mu W cm^{-2} sr^{-1} nm^{-1}$ in the fitting window) associated with high standard deviation of the residuals. These results indicate enhancements in the lowest layer up to 2.5 times concentrations present in the reference atmosphere, equivalent to 4.46 ppm CH_4 averaged across the distance from the ocean surface to 1.04 km. However, there appears to be a positive bias in these results, given concentrations for locations upwind of the plume appear higher than the expected background concentration of 1.78 ppm. Therefore, the subcolumn XCH_4 results appear overestimated. This observed bias will be further addressed in Sect. 3.12.

In Fig. 3.7, locations L1 and L2 correspond to the measured and modeled radiance plotted in Fig. 3.8. At location L1 (Fig. 8a), the measured radiance (black) is nearly horizontal for

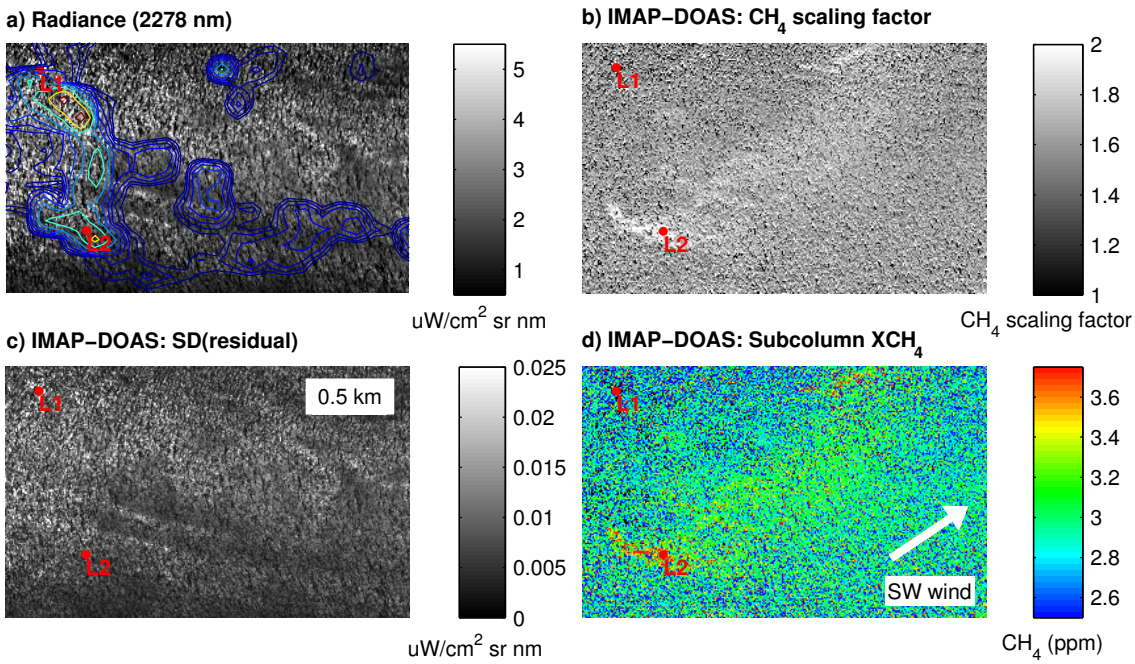

Figure 3.7. (a) Measured radiance at 2,278 nm, showing strong variability in brightness. Sonar return contours (Leifer et al. 2010) are overlain and correspond to known seep locations. (b) For the same image subset, CH_4 scaling factor for the lowest atmospheric layer (layer 10) indicates a CH_4 plume consistent with the local wind direction. (c) The standard deviation of the residuals (measured minus modeled radiance) depends strongly on brightness (a). (d) Subcolumn XCH_4 (ppm CH_4 for the lowest layer), excluding bright pixels (greater than 5 $\mu W cm^{-2} sr^{-1} nm^{-1}$ in the fitting window) associated with high standard deviation of the residuals. For two spectra (indicated by locations L1 and L2), measured and modeled radiance are provided in Fig. 3.8.

wavelengths between 2,278 and 2,328 nm, indicating sensor saturation due to high sun glint. This causes considerable disagreement with the modeled radiance (red), as indicated by the residual radiance shown in the bottom plot; this pixel was excluded from the results shown in Fig. 3.7d. For Fig. 3.8b (location L2), the radiance is considerably lower and there is better agreement between measured and modeled radiance, resulting in a retrieved concentration of 2.18 ppm CH_4 for this pixel. This radiance was detrended in Fig. 3.8c and the CH_4 Jacobian for the lowest layer is overlain to indicate the location of CH_4 absorptions at 2,298, 2,318, and 2,348 nm.

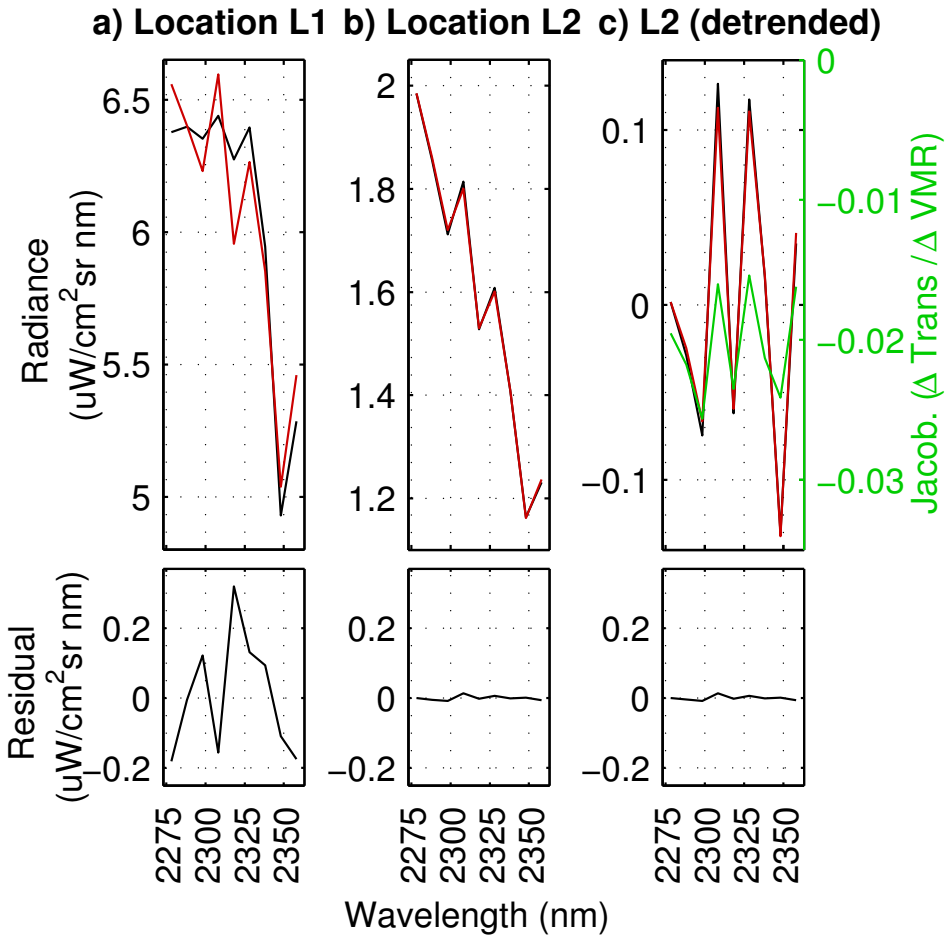

Figure 3.8. (a) For location L1 (see Fig. 3.7), the measured radiance (black) indicates sensor saturation due to high sun glint between 2,278 and 2,328 nm. This causes considerable disagreement with the modeled radiance (red), as indicated by the residual radiance shown in the bottom plot. (b) There is better agreement for location L2. (c) The radiance shown in (b) was detrended and the CH_4 Jacobian for the lowest layer overlain (green) to indicate the location of CH_4 absorptions at 2,298, 2,318, and 2,348 nm.

3.10.2 Inglewood

The Inglewood subset (Fig. 3.9a) is highly heterogeneous, with a maximum measured radiance of 0.8033, minimum of 0.0192, and mean of $0.2800\,\mu W cm^{-2} sr^{-1} nm^{-1}$ at 2,278 nm. A road crosses the scene from north to south, separating the Inglewood Oil Field on the left from a residential neighborhood on the right. In this complex urban environment, the low order polynomial in the IMAP-DOAS algorithm is unable to account for some of the high-

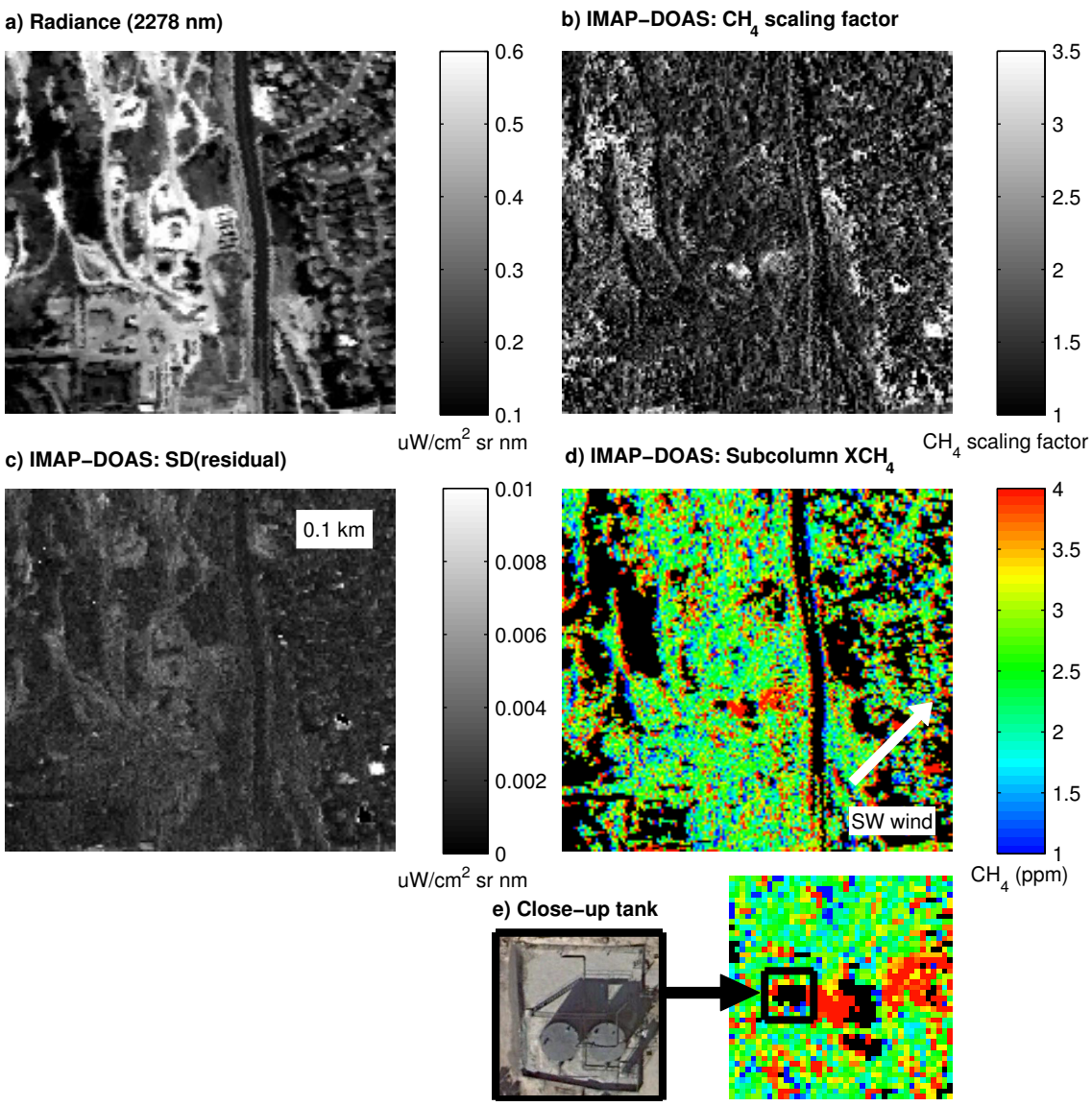

Figure 3.9. (a) Radiance at 2,278 nm, showing a portion of the Inglewood Oil Field. (b) For the same image subset, CH_4 scaling factor for the lowest atmospheric layer (layer 10) appears heavily influenced by land surface type. (c) Standard deviation of the residuals also appears influenced by land cover. (d) Subcolumn XCH_4 (ppm CH_4 for the lowest layer), excluding dark pixels (less than 0.1 $\mu W cm^{-2} sr^{-1} nm^{-1}$ in the fitting window). (e) Close-up of hydrocarbon storage tanks upwind of observed plume (Google Earth 2013).

frequency spectral variability that interferes with CH_4 absorptions. Therefore, the CH_4 scaling factor results for the lowest atmospheric layer are heavily influenced by the land surface type (Fig. 3.9b). For example, the road appears clearly visible and high CH_4 scaling factors occur for individual structures within the neighborhood. Dark spectra also appear to have

erroneously high CH_4 scaling factors, including heavily vegetated areas in the northwest and southeast of the scene.

For the lowest atmospheric layer, subcolumn XCH_4 results are shown in Fig. 3.9d, excluding dark pixels less than 0.1 $\mu W cm^{-2} sr^{-1} nm^{-1}$ in the fitting window. While background concentrations are expected around 1.78 ppm CH_4, observed background concentrations appear biased upward, between 2 and 3 ppm. Despite the noisy results, a feature of elevated CH_4 is visible in the center of the image with maximum concentrations in excess of 5.5 ppm. This CH_4 plume is consistent with a 2.2 $m\,s^{-1}$ southwesterly wind measured nearby at the time of image acquisition (http://weatherunderground.com, 2012). Using higher resolution Google Earth imagery acquired one year after the AVIRIS flight, two hydrocarbon storage tanks were identified immediately upwind and are the probable emission source (Fig. 3.9e).

3.11 Results for SVD

3.11.1 COP

While the IMAP-DOAS technique permitted CH_4 retrievals for the more homogeneous marine location, high-frequency variation present in the terrestrial example interferes with CH_4 absorptions and makes mapping more challenging. To permit retrievals for terrestrial locations, a hybrid approach using SVD and IMAP-DOAS was used to first account for high-frequency variation present in the scene and determine what variance of the standardized radiance resulted from changes in CH_4.

In Fig. 3.10, all 16 columns of $\mathbf{U}_{\text{econ}}$ are shown in addition to the CH_4 Jacobian ($\mathbf{K}_{CH_4}$). Following the iterative method described in Sect. 3.8, 4 of the total 16 columns of $\mathbf{U}_{\text{econ}}$ were used to generate $\mathbf{U}_{\text{select}}$ and account for over 99.99% of the variance. Next, $\mathbf{U}_{\text{select}}$ and $\mathbf{K}_{CH_4}$

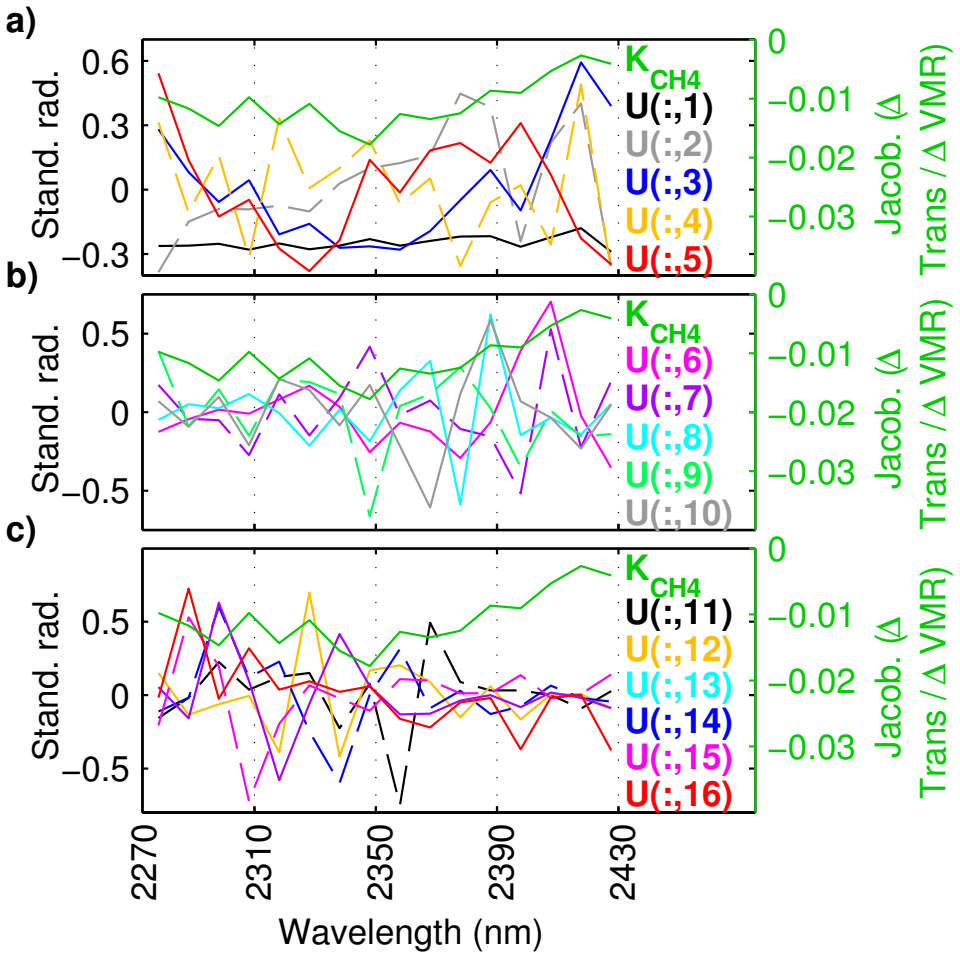

Figure 3.10. Singular vectors contained in $\mathbf{U}_{\text{econ}}$ for COP scene with CH_4 Jacobian ($\mathbf{K}_{CH_4}$) plotted for reference. (a) $\mathbf{U}_{\text{econ}}$ columns 1 to 5. (b) Columns 6 to 10. (c) Columns 11 to 16.

were concatenated to generate the **J** matrix, which is used for modeling radiance (see Eq. 3.9).

In Fig. 3.11b, the weights (RCH_4) associated with the column of **J** that corresponds to the CH_4 Jacobian are shown (see Eq. 3.9). Within the scene, expected background values are 0 and the distinctive CH_4 plume is similar to the IMAP-DOAS results (Fig. 3.7b). In Fig. 3.11d, ppm CH_4 relative to background is shown, excluding 323 pixels (0.55% o f total scene) associated with standard deviation of the residuals greater than 0.0075 (Fig. 3.11c; a unitless value given the SVD was performed on standardized radiance). CH_4 concentrations exceed 3 ppm above background within the plume, gradually decrease downwind, and approach expected

background concentrations.

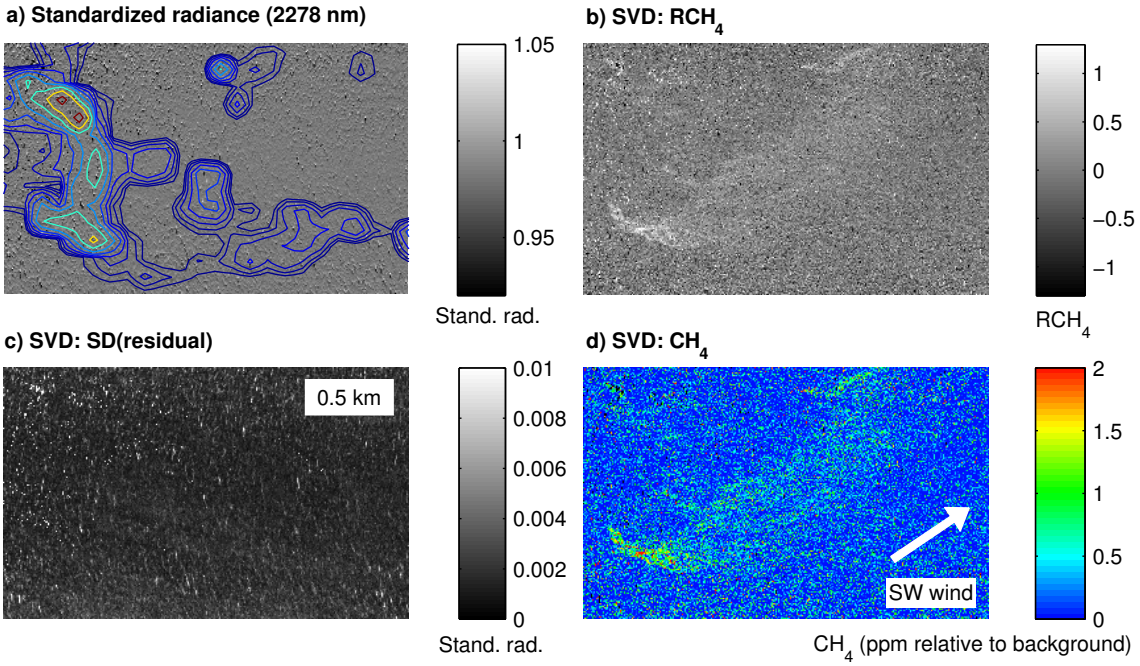

Figure 3.11. (a) Standardized radiance used for calculating SVD at COP (showing only 2,278 nm). (b) For the same image subset, RCH_4 results clearly indicate CH_4 plume. (c) The standard deviation of the residuals (measured minus modeled radiance). (d) ppm CH_4 relative to background, excluding pixels with greater than 0.0075 standard deviation of the residual (a unitless value given the SVD was performed on standardized radiance).

3.11.2 Inglewood

Using the iterative method described in Sect. 3.8, 9 columns of $\mathbf{U}_{\text{econ}}$ were selected to generate $\mathbf{U}_{\text{select}}$ for the Inglewood scene. The RCH_4 results (Fig. 3.12b) more clearly distinguish the CH_4 plume compared to the IMAP-DOAS results (Fig. 3.9b); however, the SVD standard deviation of the residuals indicates higher errors for vegetated surfaces (Fig. 3.12c). Excluding pixels with greater than 0.0075 standard deviation of the residual, retrieved concentrations relative to background are shown in Fig. 3.12d. Expected background concentrations are observed throughout much of the scene and CH_4 concentrations are highest for the western portion of the plume (in excess of 4 ppm above background).

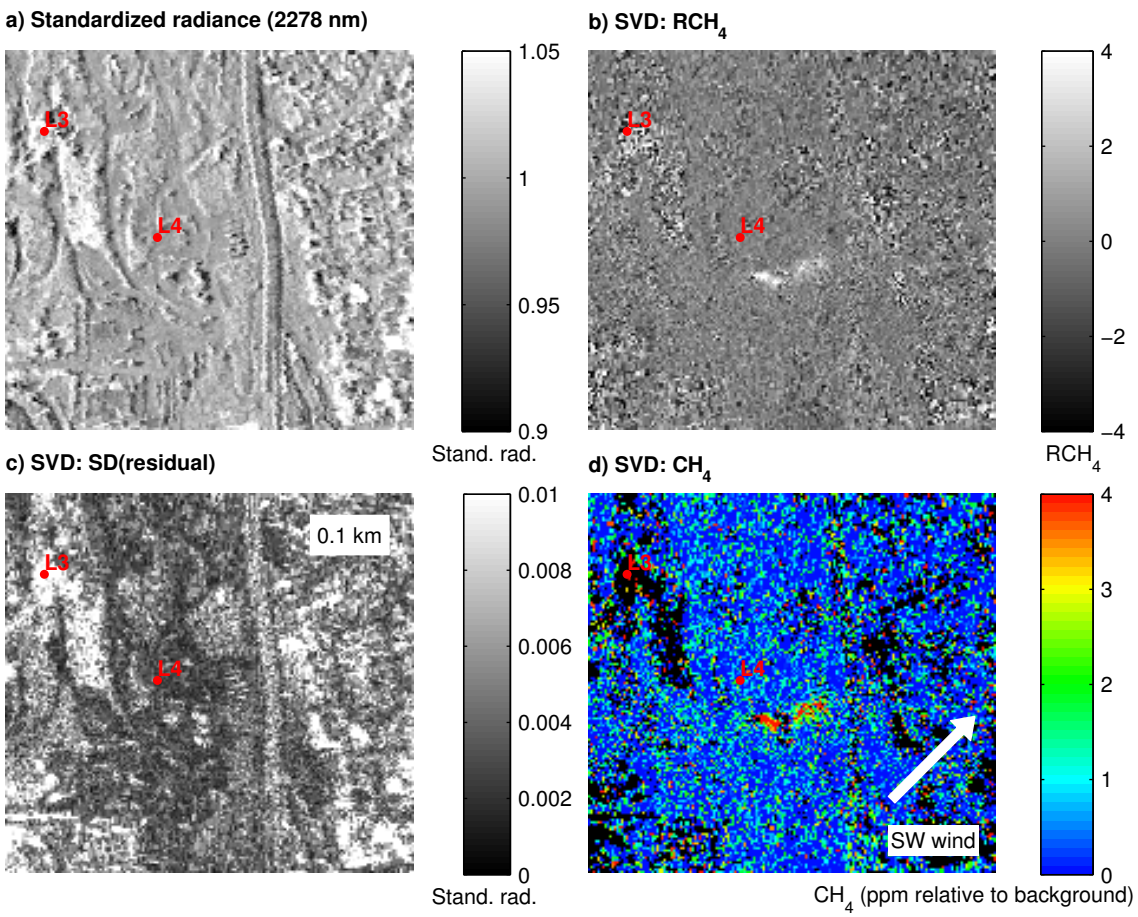

Figure 3.12. (a) Standardized radiance used for calculating SVD for Inglewood subset (showing only 2,278 nm). (b) For the same image subset, RCH_4 results indicate CH_4 plume at the center of the scene. (c) The standard deviation of the residuals (measured minus modeled radiance). (d) ppm CH_4 relative to background, excluding pixels with greater than 0.0075 standard deviation of the residual (a unitless value given the SVD was performed on standardized radiance). For two spectra (indicated by locations L3 and L4), measured and modeled radiance are provided in Fig. 3.13.

In Fig. 3.12, locations L3 and L4 correspond to the measured and modeled radiance plotted in Fig. 3.13. At location L3 (Fig. 3.13a), there is considerable disagreement between the measured (black) and modeled radiance (red), as indicated by the residual. L3 is located in a vegetated region and because the standard deviation of the residual exceeds 0.0075, this pixel was excluded from the results shown in Fig. 3.12d. In contrast, there is good agreement for L4, which is made up of bare soil with an estimated concentration of 0.38 ppm CH_4 above

background (Fig. 3.13b).

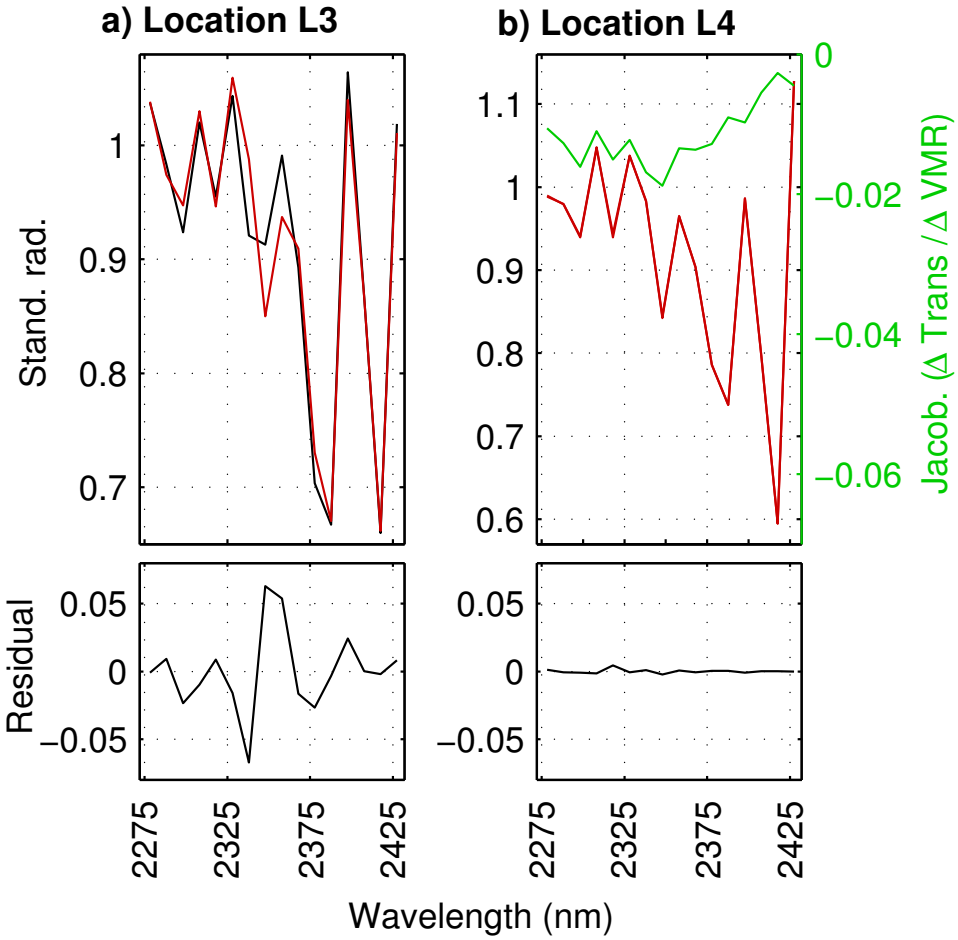

Figure 3.13. (a) The modeled (red) and measured standardized radiance (black) for location L3, which corresponds to a dark spectrum with an average radiance of $0.0376\,\mu Wcm^{-2}sr^{-1}nm^{-1}$. L3 is located in a distinct region with high values for the standard deviation of the residuals (see Fig. 3.12c) and was excluded from the results shown in Fig. 3.12d. (b) For location L4, there is better agreement between modeled and measured radiance (average $0.5187\,\mu Wcm^{-2}sr^{-1}nm^{-1}$. The CH_4 Jacobian for the lowest layer is overlain (green) to indicate the location of CH_4 absorptions.

As described in Sect. 3.10.2, high standard deviation of the residuals were observed for dark pixels in IMAP-DOAS results for the Inglewood scene (Fig. 3.9c). In Fig. 3.9d, dark pixels less than $0.1\,\mu Wcm^{-2}sr^{-1}nm^{-1}$ in the fitting window were excluded from IMAP-DOAS results, which included vegetated surfaces. For the hybrid approach using SVD and IMAP-DOAS, pixels with greater than 0.0075 standard deviation of the residual were excluded from

the results shown in Fig. 3.12d, also corresponding to vegetation within the scene. The average radiance at 2,278 nm for those pixels with greater than 0.0075 standard deviation of the residual for the hybrid approach (Fig. 3.12d, black pixels) was only $0.1368\,\mu W cm^{-2} sr^{-1} nm^{-1}$, compared to the $0.3129\,\mu W cm^{-2} sr^{-1} nm^{-1}$ average for the remaining pixels in the scene. Dark pixels and their corresponding low SNR cause lower single measure precision and are thus problematic for both the IMAP-DOAS and the hybrid approach.

3.12 Discussion

3.12.1 Comparison of retrieval results

The IMAP-DOAS and hybrid SVD approach were capable of quantifying CH_4 concentrations from plumes over marine and terrestrial environments. For both techniques, agreement between measured and modeled radiance was poorest at albedo extremes, for example saturated pixels at COP and dark, vegetated surfaces at Inglewood. SVD results indicate near surface enhancements relative to background; absorptions resulting from background CH_4 concentrations in the scene are contained in $\mathbf{U}_{\text{select}}$ and the retrieval used the CH_4 Jacobian from the lowest layer of the atmospheric model. Similarly, the IMAP-DOAS retrieval also provides ppm CH_4 enhancements averaged over the lowest atmospheric layer (up to 1.04 km).

For the IMAP-DOAS results from COP and Inglewood, an average background ppm CH_4 concentration was calculated for the portion of the scene selected to represent homogeneous land cover (see Sect. 3.8). To account for the observed positive bias in subcolumn XCH_4 (see Sect. 3.10), this average concentration was subtracted from subcolumn XCH_4, resulting in ppm CH_4 relative to background. However, different portions of each scene were excluded from IMAP-DOAS and SVD results due to observed biases. For example, pixels were excluded

from IMAP-DOAS results at Inglewood using an albedo threshold (Fig. 3.9d), while a standard deviation of the residual threshold was applied to SVD results (Fig. 3.12d). To permit comparison between results, only those pixels not excluded from either the IMAP-DOAS or SVD results are shown in Figs. 3.14 and 3.15.

These results were also compared with an independent technique, the Cluster-Tuned Matched Filter (CTMF) that was applied to both scenes (Figs. 3.14c and 3.15c). The CTMF is trained with a gas transmittance spectrum as a target to calculate CTMF scores for each image pixel where scores greater than one indicate significant evidence of the gas signature (Funk et al. 2001). Because the CTMF uses the inverse of the scene's covariance structure to remove large-scale noise to isolate the gas signal, it is best suited for detecting concentrated sources rather than background concentrations. A detailed description of the CTMF algorithm including results from both the COP and Inglewood image subsets is available in Thorpe et al. (2013). The CTMF does not provide an estimate of gas concentrations; rather, it provides an image of gas anomalies that can be evaluated for consistency with probable emissions sources and local wind direction. In contrast, IMAP-DOAS and the hybrid SVD approach provide CH_4 concentrations as well as uncertainty estimates.

At COP, there is good spatial agreement between the observed plumes obtained with the IMAP-DOAS (Fig. 3.14a), hybrid SVD (Fig. 3.14b), and CTMF (Fig. 3.14c) approaches (Thorpe et al. 2013). IMAP-DOAS CH_4 concentrations are generally higher (mean 0.12, standard deviation 0.43 ppm relative to background) than the SVD results (mean −0.01, standard deviation 0.63 ppm relative to background). The location of an identical transect is shown for the IMAP-DOAS (Fig. 3.14a, green line), SVD (Fig. 3.14b, cyan), and CTMF results (Fig. 3.14c,

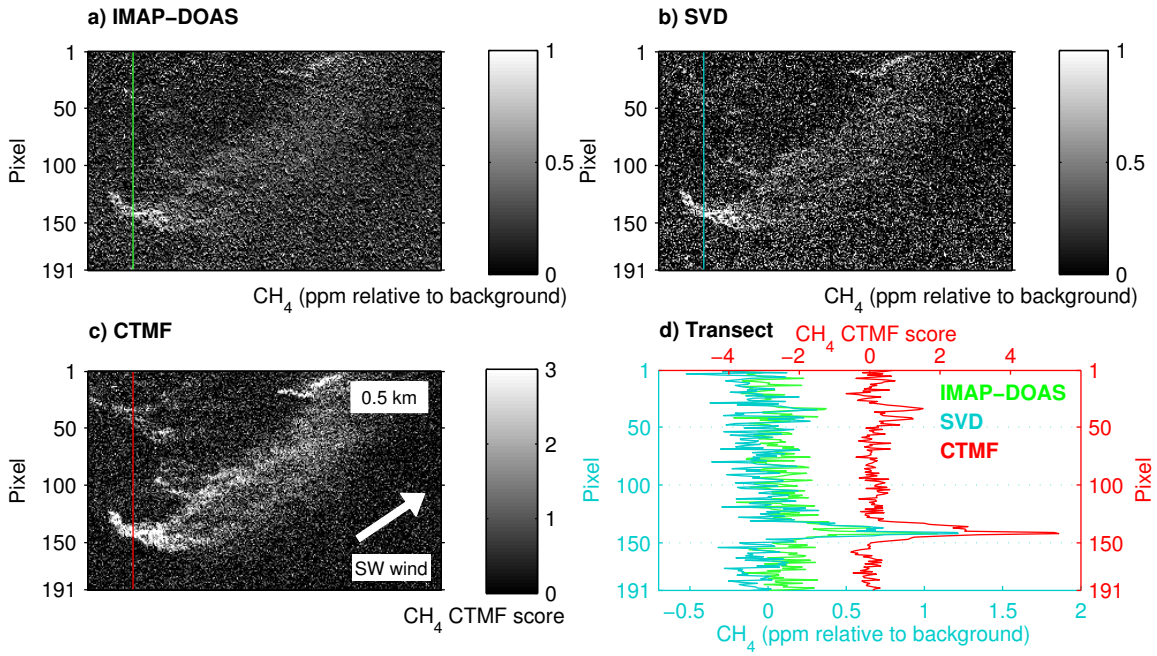

Figure 3.14. For the same COP subset, there is good agreement between results obtained using three techniques: (a) IMAP-DOAS, (b) SVD, and (c) Cluster-Tuned Matched Filter (CTMF). (d) The location of a vertical transect is shown for the IMAP-DOAS (green line), SVD (cyan), and CTFM results (red); values along the transect are shown for IMAP-DOAS (green), SVD (cyan), and CTMF (red). At each point along the transect, an average value was calculated for 21 pixels centered on the transect in the horizontal direction. IMAP-DOAS and SVD transects share the cyan figure axes, while the CTMF transect was offset for clarity and corresponds to the red figure axes.

red). At each point along the transect, an average value was calculated for 21 pixels centered on the transect in the horizontal direction. The average values along the transect are plotted in Fig. 3.14d and indicate concentrations for IMAP-DOAS (green), which are generally higher than for the SVD approach (cyan) with both transects sharing the cyan figure axes. Where the transect intersects the plume, there is good agreement in the pronounced peak in values from the three techniques, including CTMF results (red) that were offset for clarity and correspond to the red figure axes. While the CTMF technique appears better suited for detecting diffuse portions of the plume (Fig. 3.14c), it does not provide CH_4 concentrations.

Using the hybrid SVD approach, the maximum observed concentration within the scene

was 2.85 ppm CH_4 above background, located at a region of subsurface CH_4 bubble plumes, as shown by the sonar return contours (Fig. 3.11a). Averaged over the lowest atmospheric layer (a distance of 1.04 km), this maximum concentration will increase when scaled for a smaller atmospheric column. For example, concentrations increase to 590 ppm CH_4 above background if all enhancements are within a 5 m atmospheric column. Near surface concentrations are likely much higher; Leifer et al. (2006a) measured up to 2×10^4 ppm CH_4 at 5 m height using a flame ion detector.

For Inglewood, the CH_4 plume is clearly visible in IMAP-DOAS (Fig. 3.15a), hybrid SVD (Fig. 3.15b), and CTMF (Fig. 3.15c) results (Thorpe et al. 2013). CH_4 concentrations for IMAP-DOAS are generally higher (mean 0.13 and standard deviation 1.03 ppm relative to background) than the hybrid SVD results (mean −0.04 and standard deviation 1.60 ppm relative to background). Overall there is good spatial agreement for the observed CH_4 plume obtained using these three distinct techniques.

Similar to the COP comparison, the location of an identical transect is shown for the IMAP-DOAS, SVD, and CTMF results. An average was calculated at each point along the transect (for 9 pixels centered on the transect in the vertical direction) and plotted in Fig. 3.15d, indicating two locations with enhanced CH_4 between the 70th and 100th pixels. For this portion of the transect, there is considerable disagreement between the IMAP-DOAS (Fig. 3.15d, green line) and SVD concentrations (blue). This discrepancy can be partly attributed to the influence of the choice of the number of columns of $\mathbf{U}_{\text{econ}}$ used to generate $\mathbf{U}_{\text{select}}$ (see Sect. 3.8). For the transect shown in Fig. 3.15d, 9 columns of $\mathbf{U}_{\text{econ}}$ were used, resulting in a mean concentration along the transect of 0.4141 ppm CH_4 relative to background. Selecting 10 columns

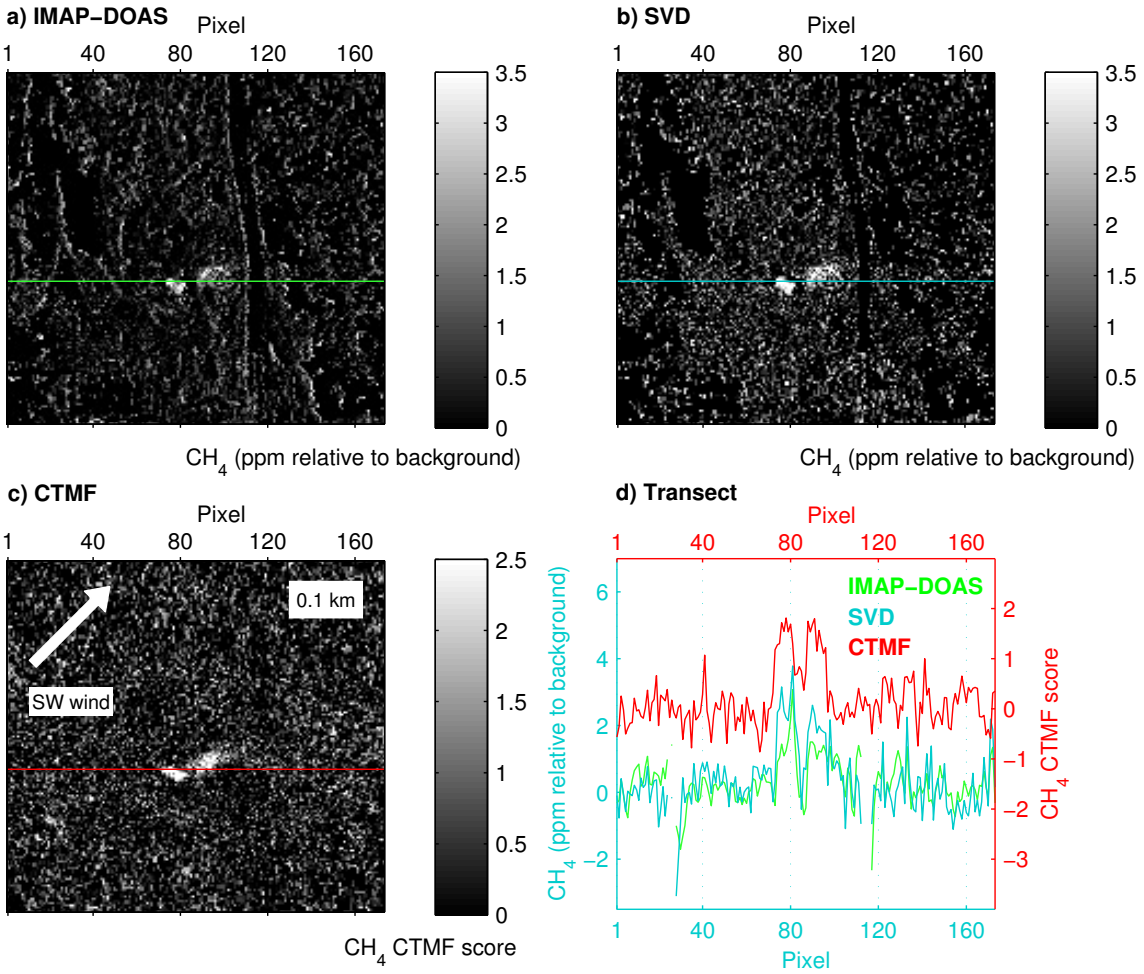

Figure 3.15. For the same Inglewood subset, there is good agreement between results obtained using three techniques: (a) IMAP-DOAS, (b) SVD, and (c) Cluster-Tuned Matched Filter (CTMF). (d) The location of a horizontal transect is shown for the IMAP-DOAS (green line), SVD (cyan), and CTMF results (red); values along the transect are shown for IMAP-DOAS (green), SVD (cyan), and CTMF (red) approach. At each point along the transect, an average value was calculated for 9 pixels centered on the transect in the vertical direction. IMAP-DOAS and SVD transects share the cyan figure axes, while the CTMF transect was offset for clarity and corresponds to the red figure axes.

of $\mathbf{U}_{\text{econ}}$ decreased the mean concentration along the transect to 0.3664 ppm relative to background with a standard deviation of the difference between transects obtained using 9 and 10 columns equal to 0.2959 ppm. In contrast, using 8 columns of $\mathbf{U}_{\text{econ}}$ results in a mean concentration of 0.4144 ppm relative to background, and the standard deviation of the difference between transects obtained using 9 and 8 columns is reduced to 0.1508 ppm relative

to background. This indicates that retrieved CH_4 concentrations obtained using the SVD approach is influenced by the choice of $\mathbf{U}_{\text{select}}$ because higher-order singular vectors can start correlating with the computed CH_4 Jacobian.

For the SVD approach at Inglewood using 9 columns of $\mathbf{U}_{\text{econ}}$, the maximum within the CH_4 plume was 8.45 ppm above background with concentrations decreasing downwind of the hydrocarbon storage tanks (Fig. 3.12d). Such enhancements are feasible given tanks represent large emission sources; natural gas storage tanks can emit between 4.3 and 42.0×10^{-4} Gg CH_4 per (10^6) m^3 gas withdrawals per year (IPCC 2000) and tank venting represented approximately 14.4% (212 Gg CH_4) of the total U.S. CH_4 emissions from petroleum systems in 2009 (EPA 2011a).

3.12.2 Potential for AVIRIS-NG and future sensors

While CH_4 retrievals are promising using AVIRIS, the next generation sensor (AVIRIS-NG) will have a 5 nm spectral resolution and FWHM, which should significantly improve CH_4 sensitivity. An IMAP-DOAS retrieval error between 0.31 to 0.61 ppm CH_4 over the lowest atmospheric layer (height up to 1.04 km) is expected for an AVIRIS scene acquired at 8.9 km altitude, 11.4° solar zenith, and with a SNR conservatively set between 100 and 200 (Fig. 3.6, black line). This corresponds to about a 32 to 63 ppm retrieval error for a 10 m thick plume or 322 to 634 ppm for a 1 m thick plume. For a similar AVIRIS-NG scene, the IMAP-DOAS retrieval error would be reduced to between 0.18 to 0.35 ppm over the lowest atmospheric layer for the same range of SNR (Fig. 3.6, red line); however, retrieval errors remain significant. In addition, SNR for AVIRIS-NG should be considerably improved, further reducing retrieval errors.

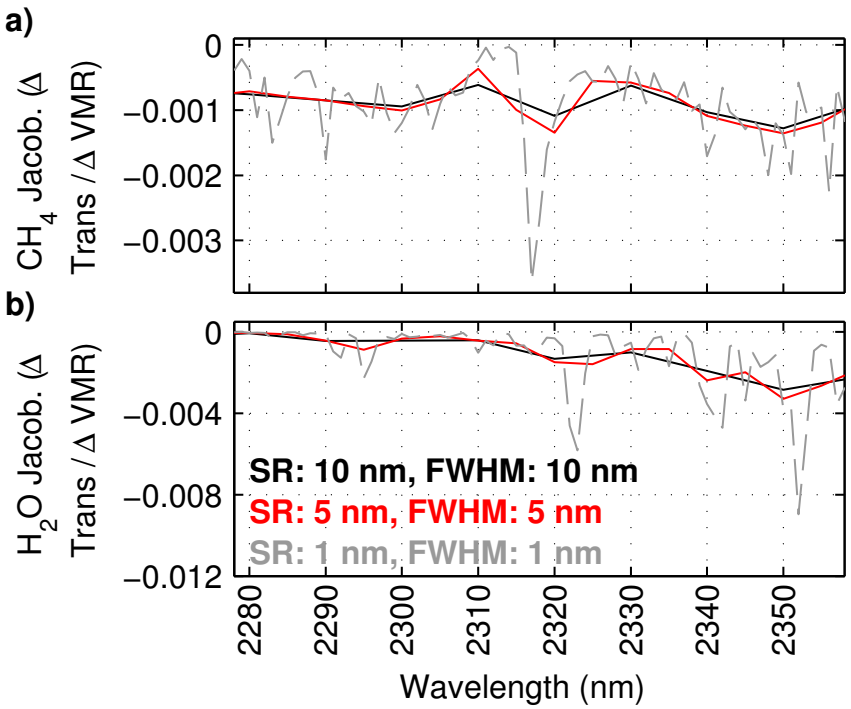

Figure 3.16. (a) For the lowest layer of the atmopsheric model (height up to 1.04 km), the CH_4 Jacobian calculated for AVIRIS-NG (red) indicates improved sensitivity compared to the CH_4 Jacobian for AVIRIS (black). Even greater sensitivity can be achieved using a finer spectral resolution (SR) and FWHM (dashed grey). (b) H_2O Jacobians calculated for the same three sensors.

To further assess this increased sensitivity, CH_4 Jacobians were calculated for AVIRIS-NG and AVIRIS for a 5% CH_4 enhancement over the lowest atmospheric layer. In Fig. 3.16a, the AVIRIS CH_4 Jacobian (black line) has a $-4.7 \times 10^{-4} \Delta\ \mu W cm^{-2} sr^{-1} nm^{-1} / \Delta$ VMR amplitude between a peak at 2,310 nm and the CH_4 absorption at 2,320 nm. For AVIRIS-NG (red line) this amplitude is $-9.8 \times 10^{-4} \Delta\ \mu W cm^{-2} sr^{-1} nm^{-1} / \Delta$ VMR roughly representing a doubling of CH_4 sensitivity compared with AVIRIS. However, additional improvements should result from a greater number of detector pixels and the improved SNR of AVIRIS-NG. Sensors with a finer spectral resolution and FWHM offer the potential for even greater sensitivity, as shown by the grey line in Fig. 3.16a for a spectral resolution and FWHM of 1 nm and reduced IMAP-DOAS retrieval errors indicated by the grey dashed line in Fig. 3.6.

3.13 Conclusions

In this study, two retrieval techniques were used to measure CH_4 enhancements for concentrated plumes over marine and terrestrial locations in AVIRIS data. The IMAP-DOAS algorithm performed well for the homogenous ocean scene containing the COP seeps, and retrieval errors are estimated between 0.31 to 0.61 ppm CH_4 over the lowest atmospheric layer (height up to 1.04 km). For the Inglewood subset, IMAP-DOAS results became heavily influenced by the underlying land cover, while the hybrid SVD approach was particularly effective given that it could better account for spectrally variable surface reflectance. Using the hybrid SVD approach for the COP and Inglewood plumes, maximum near surface concentrations were 2.85 and 8.45 ppm CH_4 above background, respectively. An additional benefit of the hybrid SVD approach is that it requires less than half the computational time than that of the IMAP-DOAS retrieval.

Given a 5 nm spectral resolution and FWHM, CH_4 sensitivity should be more than doubled for AVIRIS-NG. This might permit CH_4 retrievals for weaker absorption features centered at 1,650 nm, as well as CO_2 retrievals for absorptions at 1,572, 1,602, and 2,058 nm. However, both the AVIRIS and AVIRIS-NG sensors were not designed for detecting gas plumes, and sensitivity could likely be dramatically improved using a spectrometer designed exclusively for mapping gas plumes. For example, an imaging spectrometer with 0.05 nm spectral resolution and 0.15 nm FWHM would have an IMAP-DOAS error around 18 times smaller than AVIRIS.

While non-imaging spectrometers such as MAMAP have increased CH_4 sensitivity compared to AVIRIS and AVIRIS-NG, they are currently limited to flying transects across local

gas plumes due to a small field of view. In contrast, airborne imaging spectrometers combine large image footprints and fine spatial resolution necessary to map local CH_4 plumes in their entirety; however, they have considerably higher expected errors for retrieved CH_4 concentrations.

In this study, the observed COP plume extended more than 1 km; however, the Inglewood plume was much smaller, extending only 0.1 km downwind. Such plumes with a small spatial extent are of increasing concern, including industrial point source emissions, leaking gas pipelines (Murdock et al. 2008), and fugitive CH_4 emissions (Howarth et al. 2011). Imaging spectrometers permit direct attribution of emissions to individual point sources, which is particularly useful given the large uncertainties associated with anthropogenic emissions, including fugitive CH_4 emissions from the oil and gas industry (Petron et al. 2012; EPA 2013; Allen et al. 2013), and the projected increase in these types of emissions (EPA 2006a). Therefore, AVIRIS-like sensors offer the potential to better constrain emissions on local and regional scales (NRC 2010), improve greenhouse gas budgets and partitioning between natural and anthropogenic sources, as well as complement data provided at coarser spatial resolutions.

3.14 Acknowledgments

NCEP Reanalysis data provided by the NOAA/OAR/ESRL PSD, Boulder, Colorado, USA, from their web site at http://www.esrl.noaa.gov/psd/. The authors would like to thank Debra Wunch for aiding in generating NCEP atmospheric profiles and for the continued support of Robert Green and the rest of the AVIRIS/AVIRIS-NG team at the Jet Propulsion Laboratory. In addition, we thank Joseph McFadden for his insightful comments. This work was supported by NASA Headquarters under the NASA Earth and Space Science Fellowship

Program grant NNX13AM95H. This work was undertaken in part at the Jet Propulsion Laboratory, California Institute of Technology, under contract with NASA as well as at the University of California, Santa Barbara.

Chapter 4

Mapping methane concentrations from a controlled release experiment using the next generation Airborne Visible/Infrared Imaging Spectrometer (AVIRIS-NG)

A. K. Thorpe[1,2], C. Frankenberg[2], A.D. Aubrey[2], D. A. Roberts[1], et al.

[1]Department of Geography, University of California, Santa Barbara, Santa Barbara, CA

[2]Jet Propulsion Laboratory, California Institute of Technology, Pasadena, CA

This chapter was submitted to Remote Sensing of Environment and is referenced as Thorpe et al. (submitted).

4.1 Abstract

Emissions estimates of anthropogenic methane (CH_4) sources are highly uncertain and many sources related to energy production are localized yet hard to quantify. Airborne imaging spectrometers like the next generation Airborne Visible/Infrared Imaging Spectrometer (AVIRIS-NG) are well suited for locating CH_4 point sources by covering large regions with the high spatial resolution necessary to resolve localized emissions. As part of a field campaign with controlled CH_4 releases at the Rocky Mountain Oilfield Testing Center (RMOTC) in Wyoming, U.S., a number of CH_4 plumes were clearly visible at multiple flux rates and flight altitudes. Images of plumes were in agreement with wind directions measured at ground stations and were consistently present for fluxes as low as 14.16 m^3/h, equivalent to 0.09 kt/year. In some cases plumes were detected as low as 3.40 m^3/h (0.02 kt/year), indicating that AVIRIS-NG has the capability of detecting a number of fugitive CH_4 source categories for natural gas fields. This controlled release experiment demonstrates how imaging spectrometers permit direct attribution of emissions to individual point source locations, which is particularly useful given the large uncertainties associated with anthropogenic emissions, including those from industry, gas transmission lines, and the oil and gas sectors.

4.2 Introduction

Atmospheric methane (CH_4) is an important greenhouse gas with a Global Warming Potential (GWP) 86 times that of carbon dioxide (CO_2) for a 20 year time interval (Myhre et al. 2013). The growth rate of global atmospheric CH_4 concentrations slowed between 1999 and 2006, but has increased since 2007 (Nisbet et al. 2014). The causes of these observed increases remain unclear and reflect uncertainty in the global CH_4 budget (Kirschke et al.

2013). Between 50-65% of the global CH_4 budget can be attributed to anthropogenic emissions (Ciais et al. 2013), however, there is considerable uncertainty regarding partitioning between individual anthropogenic source types and locations.

In the United States, major anthropogenic CH_4 sources listed by importance include livestock (enteric fermentation and manure management), natural gas systems (production, transmission, and storage), landfills, coal mining, and petroleum systems (EPA 2013). Numerous studies suggest bottom-up inventories for natural gas production and distribution are underestimated (Kort et al. 2008; Miller et al. 2013; Brandt et al. 2014). Multiple top-down estimates suggest fugitive CH_4 emissions from natural gas and oil production can be large, ranging between 2.3 to 7.0% of CH_4 produced annually for the Denver-Julesburg Basin, Colorado (Petron et al. 2012) and between 6.2 to 11.7% of average hourly natural gas production in the Uintah County oil and gas field (Karion et al. 2013). These estimates pertain to specific locations and times, while leak rates from different facilities should vary considerably. For example, additional studies suggest that fugitive CH_4 leakage is considerably lower (Alvarez et al. 2012; Allen et al. 2013; O'Sullivan and Paltsev 2012).

Airborne measurements are increasingly being used to study fugitive CH_4 emissions from the oil and gas industry. So far, these mostly comprise airborne in situ measurements of CH_4 using mass balance approaches (Karion et al. 2013), ethane (C_2H_6) to CH_4 enhancement ratios (Wennberg et al. 2012), and observations of alkanes used with high-resolution atmospheric transport models (Miller et al. 2013). Airborne spectrometers like MAMAP (Methane Airborne MAPper) can not provide the same level of accuracy and precision as in-situ data but offer the potential to detect and quantify fugitive CH_4 emissions (Gerilowski et al. 2011). For

example, MAMAP measurements of elevated CH_4 concentrations from coal mine ventilation shafts near Ibbenbüren, Germany permitted an inversion estimate in good agreement with reported emissions rates from mine operators (Krings et al. 2013). However, MAMAP is a non-imaging spectrometer with a small field of view (FOV) limited to flying transects across local gas plumes rather than mapping plumes in their entirety. Recently, thermal infrared imaging spectrometers such as MAKO (Tratt et al. 2014) and the Hyperspectral Thermal Emission Spectrometer (HyTES) (Hulley et al. in prep) have mapped CH_4 plumes over active oil and gas fields.

The Airborne Visible/Infrared Imaging Spectrometer (AVIRIS) (Green et al. 1998) was not designed for detecting gas plumes, but has been used for high resolution mapping of fugitive CH_4 emissions at the Inglewood Oil Field in Los Angeles, California (Thorpe et al. 2013). To measure CH_4 enhancements, the iterative maximum a posteriori differential optical absorption spectroscopy (IMAP-DOAS) algorithm (Frankenberg et al. 2005b) was modified for use with AVIRIS between 2,278 and 2,358 nm (Thorpe et al. 2014). To better account for highly variable surface reflectance, a hybrid approach using IMAP-DOAS and Singular Value Decomposition (SVD) was also developed (Thorpe et al. 2014). By combining large image swaths and fine spatial resolution, imaging spectrometers like AVIRIS permit direct attribution of emissions to individual point source locations.

Due to an improved 5 nm spectral resolution, the next generation sensor (AVIRIS-NG) has greater sensitivity to CH_4 (Dennison et al. 2013; Thorpe et al. 2014). To better understand the ability of AVIRIS-NG to detect and quantify CH_4 emissions, a controlled CH_4 release experiment using variable flux rates was performed with AVIRIS-NG overflights in June 2013.

This study evaluates which flux rates can be observed using both a non-quantitative matched filter algorithm and the quantitative hybrid retrieval using IMAP-DOAS and SVD.

4.3 Controlled release experiment

The controlled release experiment was performed at the Rocky Mountain Oilfield Testing Center (RMOTC), a U.S. Department of Energy (DOE) facility located approximately 50 km northeast of Casper, Wyoming. RMOTC extends across the 10,000 acres of the Naval Petroleum Reserve No. 3 (NPR-3) and was used as an energy testing center and for oil and gas production (Fig. 4.1). As of July 2014, testing at RMOTC has been officially completed and NPR-3 was sold by the U.S. DOE in January 2015.

The experiment was performed towards the north where there were fewer oil and gas wells and the influence of fugitive CH_4 emissions could be minimized (Fig. 4.1). Three controlled release sites were located nearly collinearly, including the northern most site (X-N), central site (X-C), and the southern site (X-S). Each site was separated by at least 1.5 km and ground elevation ranged between 1.51 and 1.58 km. The land cover was a mixture of grass-shrubland and was characterized by bare soil as well as green and senesced vegetation during late June when the controlled release occurred.

A total of 5 meteorological towers were used (Fig. 4.2d), one 15 m tower at site X-N and X-C and 3 towers at the flattest site X-S (2 at 15 m and 1 at 3 m). These towers were equipped with a suite of meteorological instrumentation, including high frequency (20 Hz) 3-D sonic anemometers at multiple heights (5, 9, and 13 m) and sensors for air temperature, relative humidity, as well as downwelling/upwelling long and short wave infrared radiation. For this study, observed plumes were evaluated for consistency with the wind speed and direction

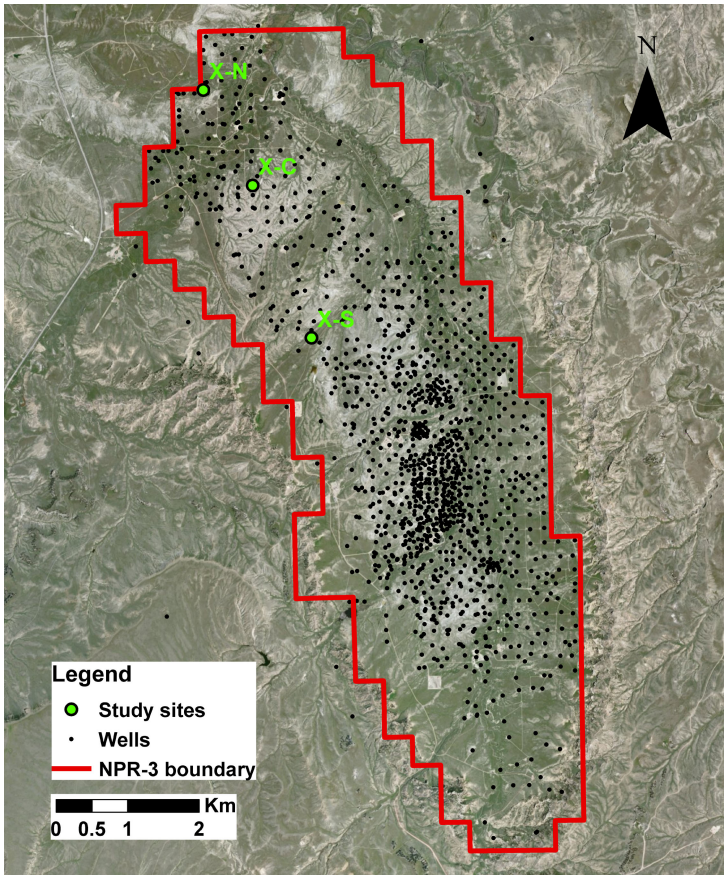

Figure 4.1. The Rocky Mountain Oilfield Testing Center is located approximately 50 km northeast of Casper, Wyoming. Outlined in red, it spans 10,000 acres of the Naval Petroleum Reserve No. 3 (NPR-3) and contains a number of oil and gas wells (black points). Three controlled release sites were located nearly collinearly (shown in green), including sites X-N, X-C, and X-S. Image data provided by RMOTC and the U.S. DOE.

obtained from the towers.

The experiment was performed over 7 days (20-26 June 2013) and for 6 flight days CH_4 was released at all sites, with metered flux rates ranging between 3.26 and 141.58 m^3/h (115 and 5,000 standard cubic feet per hour, scfh). For each of the 3 sites, a trailer tank contained the CH_4 (Fig. 4.2b), which was piped to a flow regulator to prevent icing due to adiabatic gas expansion and control the flux rate (Fig. 4.2b, device directly in front of trailer tank). Using a 7.6 cm diameter flexible rubber hose, the CH_4 was next piped to a 1 by 1 m square diffuser that was fabricated from metal pipes with holes every few inches to prevent buoyancy effects and

ensure the plume remained somewhat diffuse (Fig. 4.2c). This method was selected to prevent generating a 'CH_4 jet,' a more concentrated plume emitted at higher velocity that would occur using one narrow release point (i.e. using the rubber hose alone). Each morning the release points were oriented upwind of the towers and CH_4 releases began approximately 30 minutes before aircraft overflights.

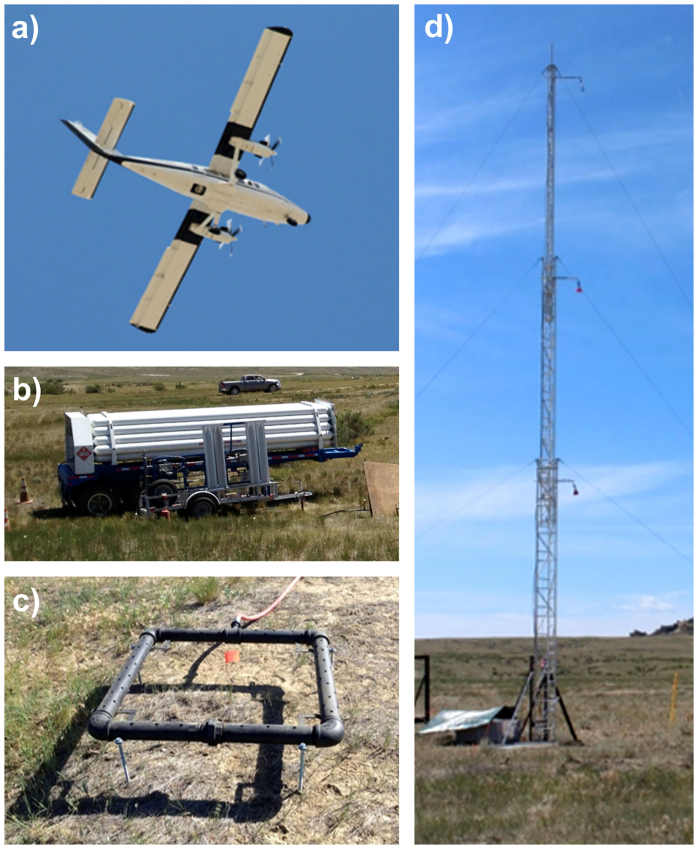

Figure 4.2. (a) Twin Otter aircraft used with AVIRIS-NG. (b) Trailer tank storing CH_4 at one of controlled release sites. (c) Controlled release using square diffuser. (d) Meteorological towers at site X-S equipped with suite of meteorological instrumentation that includes wind speed and direction.

In addition to AVIRIS-NG, the Hyperspectral Thermal Emission Spectrometer (HyTES) was flown, a 7.5-12 micron hyperspectral grating spectrometer using a quantum well infrared photodetector (Johnson et al. 2011). For most of the experiment AVIRIS-NG and HyTES

flew in separate Twin Otter aircraft in close succession at multiple altitudes ranging between 0.43 and 3.80 km above ground level (AGL). The Carbon in Arctic Reservoirs Vulnerability Experiment (CARVE) was also flown, which included a nadir-viewing Fourier Transform Spectrometer (FTS) as well as an onboard Picarro for CH_4 measurement (Miller and Dinardo 2012). Finally, additional in situ CH_4 sampling was performed using a commercial quadrotor equipped with the Compact Herriott Cell Analytical Spectrometer Experiment (CHASE), a tunable diode laser for CH_4 (Christensen et al., in prep). The analysis of this study focuses solely on AVIRIS-NG results.

4.4 AVIRIS-NG instrument and data processing

The next generation Airborne Visible/Infrared Imaging Spectrometer (AVIRIS-NG) is a push-broom imaging spectrometer with 598 across track elements of 1 milliradian instantenous field of view (FOV) covering a total FOV of 36°. AVIRIS-NG measures reflected solar radiance at the nadir viewing geometry at a 100 Hz readout rate across 427 channels between 380 and 2,510 nm with a spectral sampling of 5 nm and a full width at half maximum (FWHM) of approximately 6 nm (Hamlin et al. 2011). This pushbroom instrument was developed at the Jet Propulsion Laboratory (JPL) and is similar to the visible-to-shortwave infrared (VSWIR) imaging spectrometer used in the Carnegie Airborne Observatory next generation Airborne Taxonomic Mapping Systems (AToMS) (Asner et al. 2012). In addition, similar spectrometers are being used in the Airborne Observation Platform (AOP) by the National Ecological Observatory Network (NEON) (Kampe et al. 2010). This new class of imaging spectrometers is based on the design of the Airborne Visible/Infrared Imaging Spectrometer (AVIRIS), which provides 224 spectral channels at a 10 nm spectral resolution, measuring across-track with a

whisk-broom scanning mechanism.

During the flight campaign, a total of 55 flight lines were acquired with AVIRIS-NG at altitudes ranging between 0.43 and 3.80 km above ground level (AGL). While AVIRIS-NG can be flown at higher altitudes using an ER-2 aircraft, a Twin Otter aircraft was used for the controlled release experiment (Fig. 4.2a). CH_4 detection algorithms were applied to non-orthorectified AVIRIS-NG scenes, which are 598 pixels wide (cross track direction) and have an along track image dimension that depend on flight duration. Images were subsequently orthorectified and resulted in spatial resolutions ranging between 0.4 m per pixel for a flight at (0.43 km AGL with image swath width 0.28 km) to 3.6 m per pixel (3.80 km AGL with image swath of 2.47 km).

4.5 Hybrid IMAP/SVD methane retrieval

Quantifying CH_4 concentrations present within AVIRIS-NG scenes requires radiative transfer modelling of solar radiation along the light path to the sensor in the SWIR. One technique previously applied to AVIRIS for CH_4 retrievals uses the iterative maximum a posteriori differential optical absorption spectroscopy (IMAP-DOAS) algorithm (Frankenberg et al. 2005b; Thorpe et al. 2014). IMAP-DOAS uses the Lambert-Beer law and optimal estimation theory to adjust the slant column densities of multiple gasses until total optical density fits the observed measurement. This permits direct comparison of simulated at sensor radiance with a known abundance of absorbers to radiance measured by the imaging spectrometer.

As shown in previous work for moderate resolution spectrometers like AVIRIS, disentangling lower frequency features such as surface reflectance from higher frequency gas absorption features can be challenging using IMAP-DOAS (Thorpe et al. 2014). To address this, an

alternative hybrid approach using both IMAP-DOAS and singular value decomposition (SVD) of surface reflectance properties at background CH_4 concentrations was also developed for AVIRIS (Thorpe et al. 2014). SVD is closely related to Principal Component Analysis (PCA) and has been used in a number of remote sensing applications to reduce computation time by summarizing high dimensional data (Kluser et al. 2011; Guanter et al. 2012). SVD is based on the transformation of a large number of potentially correlated vectors into a smaller set of uncorrelated (orthogonal) vectors that are denoted as singular vectors (Press et al. 2007; Rodgers 2000).

For this study, the hybrid approach was modified for use with AVIRIS-NG. Based on a simple non-scattering radiative transfer scheme, IMAP-DOAS is used as a forward radiative transfer model at high spectral resolution using 10 atmospheric layers and the gases CH_4, H_2O, and N_2O to calculate modeled radiance at each wavelength. The high resolution modeled radiance is then convolved with the instrument lineshape function (ILS) and interpolated to the center wavelengths of each AVIRIS-NG spectral band. This generates a lower resolution modeled radiance at the ith iteration of the state vector ($\vec{F}^{\mathrm{lr}}(\vec{x}_i)$), calculated using a known reference total optical density $\boldsymbol{\tau}^{\mathrm{ref}}$ scaled by $\vec{x}_i$, the trace gas related state vector at the ith iteration. Additional details on the IMAP-DOAS portion of the hybrid retrieval can be found in Thorpe et al. (2014).

A Jacobian Matrix $\mathbf{K}_i$ is calculated for each iteration i, where each column represents the derivative vector of the sensor radiance with respect to each element of the state vector ($\vec{x}_i$) as follows

$$\mathbf{K}_i = \left.\frac{\partial \vec{F}^{\mathrm{lr}}(\vec{x})}{\partial \vec{x}}\right|_{\vec{x}_i} \tag{4.1}$$

The Jacobian Matrix and forward model is used to optimize the state vector at the ith iteration as described in Rodgers (2000).

An example of a high resolution CH_4 Jacobian is shown in Fig. 4.3a (light red), indicating weaker absorption features between 1,600 to 1,820 nm and stronger absorptions between 2,130 and 2,450 nm. The water vapor (H_2O) Jacobian is also shown in Fig. 4.3b (light blue) and indicates some spectral overlap with CH_4. AVIRIS-NG was not designed for CH_4 detection and because its relatively coarse spectral resolution is far wider than individual gas absorption features it cannot fully resolve the individual CH_4 absorption lines shown by the high resolution CH_4 Jacobian. As a result, CH_4 sensitivity is reduced compared to instruments with finer spectral resolutions and there are potential interferences with lower resolution surface albedo features. Convolved results using the AVIRIS-NG ILS function are also shown for CH_4 (Fig. 4.3a, dark red) and H_2O (Fig. 4.3b, dark blue). While CH_4 absorption features are weaker between 1,600 to 1,820 nm, reflected radiances are generally higher at shorter wavelengths as compared to the lower radiances present for strong absorptions between 2,130 and 2,450 nm (Fig. 4.3c).

For this study, the hybrid IMAP/SVD approach was applied individually to each spatial row (along track element) of the AVIRIS-NG detector independently prior to orthorectification. This minimizes striping effects due to small variability in detector characterization across the focal plane. Radiance was first standardized by fitting a first order polynomial to each radiance spectrum and dividing it by the polynomial fit. For each along track element e, a mean radiance spectrum was calculated from the standardized data and the IMAP-DOAS retrieval was performed on the mean spectrum to generate the CH_4 Jacobian ($\mathbf{K}_{CH4,e}$).

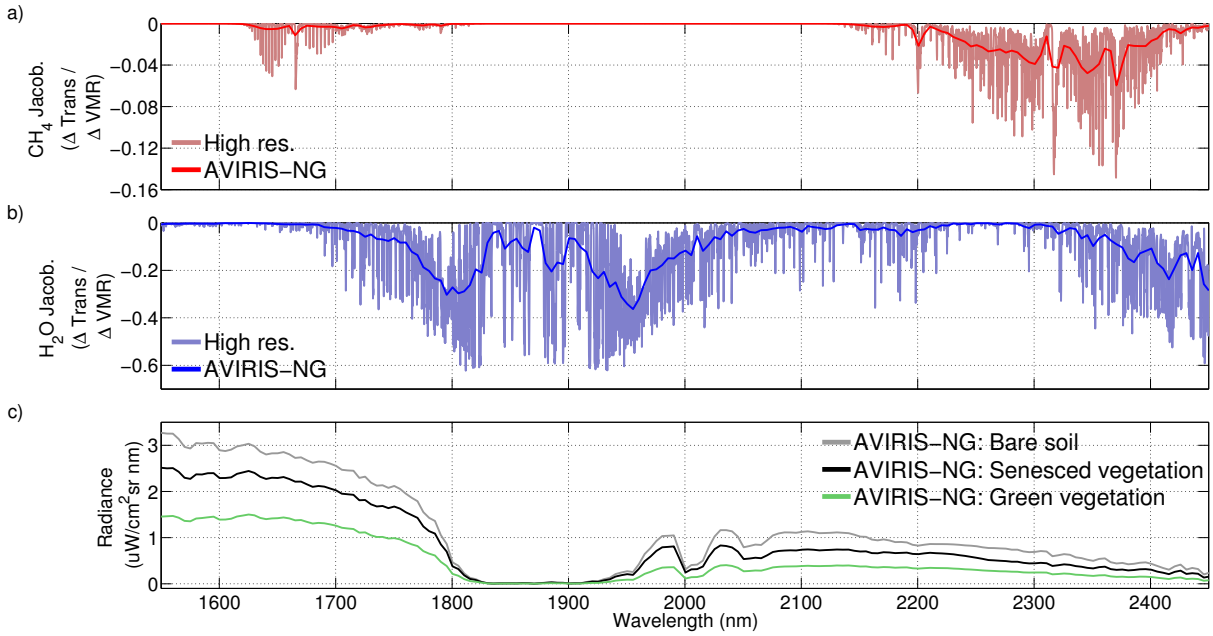

Figure 4.3. (a) Example of a high resolution CH_4 Jacobian (light red) and convolved results using the AVIRIS-NG ILS function (dark red). (b) High resolution H_2O Jacobian (light blue) and convolved results (dark blue). (c) Example AVIRIS-NG radiances for bare soil, senesced vegetation, and green vegetation.

We constructed an $m \times n$ matrix $\mathbf{L}_e$ for each along track element e, where m is the number of spectral bands (for the CH_4 fit window) and n is the number of radiance spectra in each along track element as follows

$$\mathbf{L}_e = \mathbf{U}_e \mathbf{\Lambda}_e \mathbf{V}_e^T \tag{4.2}$$

where the $m \times m$ matrix $\mathbf{U}_e$ contains the left singular vectors, the matrix $\mathbf{V}_e$ contains the right singular vectors in their respective columns, and matrix $\mathbf{\Lambda}_e$ contains the m singular values of $\mathbf{L}_e$ on its diagonal. $\mathbf{L}_e$ can be recomposed as a linear combination of singular vectors scaled by the singular values (Murtagh and Heck 1987).

$\mathbf{U}_{select}$, an $m \times c$ matrix using the first c columns of $\mathbf{U}_e$ (optimal selection of c is described below) and the CH_4 Jacobian ($\mathbf{K}_{CH4,e}$, an $m \times 1$ matrix) are concatenated to generate a matrix $\mathbf{J}_e$ (dimensions of $m \times c + 1$). Next, linear least squares can be used to find a vector $\vec{W}_e$ that

minimizes the cost function involving each of the measured radiance spectra $\vec{y}$ within each along track element e:

$$\left|\left|\vec{y} - \mathbf{J}_e \vec{W}_e\right|\right|^2 \tag{4.3}$$

where $\vec{W}_e$ represents the contribution of each column of $\mathbf{J}_e$ to the measured radiance. Modeled radiance $\vec{F}$ can be calculated as the sum of the background and CH_4 component of the radiance as follows:

$$\vec{F}\left(\vec{W}_e, \mathbf{J}_{e,k}\right) = \sum_{k=1}^{c} \mathbf{J}_{e,k} \cdot \vec{W}_{e,k} + \mathbf{J}_{e,c+1} \cdot \vec{W}_{e,c+1} \tag{4.4}$$

The left term represents the background radiance modeled as a linear combination of the first c eigenvectors of $\mathbf{J}_e$ ($\mathbf{J}_{e,k}$) multiplied by the corresponding weights $\vec{W}_{e,k}$. The right term is the CH_4 component of the scene, the product of $\mathbf{J}_{e,c+1}$ (the CH_4 Jacobian, $\mathbf{K}_{CH4,e}$) and its corresponding weight $\vec{W}_{e,c+1}$ (denoted as RCH_4).

RCH_4 indicates how much of the observed radiance for each spectrum can be associated with the CH_4 Jacobian (i.e. changes in absorption due to CH_4). RCH_4 is multiplied by the volume mixing ratio (VMR) for the lowest layer of the reference atmosphere to estimate the CH_4 concentration in ppm above/below background. This represents an empirical method of computing the forward model radiance, including many detector and surface albedo features that can be problematic for the IMAP-DOAS approach at coarse spectral resolutions (Thorpe et al. 2014).

The hybrid approach used a 29 band retrieval window between 2,278 and 2,423 nm similar to a previous study using AVIRIS (Thorpe et al. 2014). To determine the optimal number of c columns of $\mathbf{U}_e$ used to generate $\mathbf{U}_{select}$, the hybrid retrieval was performed iteratively by increasing the c columns. This resulted in 29 retrievals that were assessed by minimizing the

standard deviation of the RCH_4 results for the portion of the scene representing homogeneous landcover. While the retrieval was applied to non-orthorectified data, these results were subsequently orthorectified to generate a planimetrically correct image. Additional details on the hybrid retrieval can be found in Thorpe et al. (2014).

4.6 Matched filter detection

In addition to the hybrid retrieval, a non-quantitative matched filter technique was also applied to AVIRIS-NG scenes. The matched filter is well suited for detecting weak signals overlain on a cluttered background and has been used to detect simulated gas plumes in the thermal infrared (Funk et al. 2001; Theiler and Foy 2006). It generates a linear weighting function that produces high values when an unknown spectrum matches the shape of a known gas target spectrum and uses the inverse of the scene's covariance structure to remove large-scale noise (background clutter) while isolating the gas signal.

To generate the CH_4 target for this study, one CH_4 Jacobian was generated with IMAP-DOAS using an average radiance generated from an AVIRIS-NG scene (see Sect. 4.5, Eq. 4.1). The matched filter is 'matched' to both the gas signature as well as the background clutter and was calculated using the following equation applied to each along track element e of the non-othorectified AVIRIS-NG radiance images

$$\vec{q_e} = \frac{\mathbf{C}_e^{-1}\vec{b}}{\sqrt{\vec{b^T}\mathbf{C}_e^{-1}\vec{b}}} \tag{4.5}$$

where $\vec{q_e}$ is the matched filter and represents an m-dimensional vector of optimal weights, where m is the number of spectral channels. $\mathbf{C}_e^{-1}$ is the inverted $m \times m$ covariance matrix, $\vec{b}$ is the m-dimensional vector containing the CH_4 target spectrum (CH_4 Jacobian), and T is the transpose operator.

All 427 AVIRIS-NG spectral channels were used for the matched filter algorithm and radiance was first standardized by subtracting the mean and dividing by the standard deviation of the scene, both scalar values. For each image pixel, a matched filter score was calculated by multiplying the transpose of the matched filter by the standardized radiance. Scores greater than one indicate significant evidence of the gas signature, which can be quantified by the 'number of sigmas' for the z distribution. A detailed description of the matched filter algorithm is available in Funk et al. (2001) and Thorpe et al. (2013). Similar to the hybrid retrieval results, matched filter results were subsequently orthorectified to generate a planimetrically correct image.

The matched filter detection algorithm does not directly quantify gas concentration, and in previous studies has been used to provide an image of gas anomalies that can be evaluated for consistency with probable emissions sources and local wind direction (Thorpe et al. 2013; Thorpe et al. 2014). In this study, segmentation based on 8-connectivity was applied to the matched filter results to isolate contiguous pixels with matched filter scores greater than 2 (equivalent to 2 standard deviations) and minimum population size of 16 pixels. Segmented matched filter results were used to generate a mask that was applied to results from the hybrid retrieval. Because the matched filter CH_4 detection sensitivity appears greater than for the hybrid retrieval (Thorpe et al. 2014), this method allows for an improved means of isolating CH_4 plumes.

4.7 Results

4.7.1 Multiple fluxes and flight altitude examples

A total of 5 of the total 29 columns of $\mathbf{U}_e$ were used to generate $\mathbf{U}_{select}$ (see Sect. 4.5 for selection criteria). The weights (RCH_4) associated with the column of **J** that corresponds to the CH_4 Jacobian (i.e. changes in absorptions due to CH_4) were calculated first. Next, RCH_4 was multiplied by the VMR for the lowest layer of the reference atmosphere in order to estimate CH_4 concentration in ppm above/below background averaged over a 1 km subcolumn. For presentation, AVIRIS-NG CH_4 retrievals will be displayed as plumes overlain on true color images with enhancements shown in g/m^2 and ppm (for a 1 km layer).

An assessment of the plume shapes and orientations show consistency with the wind direction as measured by the meteorological towers at each site. Further, higher winds produce elongated plumes compared to the more compact appearance for lower wind speeds. For example, the three plumes shown in Fig. 4.4 indicate orientations that agree well with the wind speed and direction measured by nearby meteorological towers (white arrows). These examples were acquired approximately 7 minutes apart at location X-N for a 56.6 m^3/h (2,000 scfh) flux and a flight altitude of 0.58 km AGL (0.5 m pixel resolution). The plume in Fig. 4.4b (6.9 m/s wind) appears elongated (56.6 m maximum length, 5.5 m maximum width) compared to the more compact plume observed in Fig. 4.4c for a 1.9 m/s wind (50.1 m maximum length, 10.4 m maximum width). Further, the maximum observed concentration (9.06 ppm, 5.07 g/m^2 with the high wind case (2.96 ppm, 1.65 g/m^2). This is also consistent with accumulation of CH_4 due to low wind speed rather than more efficient advection of CH_4 (thus lower concentrations) for higher wind speeds.

In Fig. 4.4a, an apparent false positive is observed at the meteorological tower in the upper right portion of the scene. However, this does not occur in the 2 subsequent scenes. Therefore the false positive is not caused solely by the spectral properties on the meteorological tower. Given the shape and trajectory of the plume in Fig. 4.4a, this false positive may result from the combined effects of the increased brightness of the tower and elevated CH_4 concentrations downwind of the plume. In Fig. 4.4b, an apparent false positive also occurs for a white cotton sheet that was included as part of the experiment (center of scene). However, only the right hand portion of the sheet appears as a false positive in Fig. 4.4c. Similar to the meteorological tower example, this could result from the combined effects of the increased brightness and elevated CH_4 concentrations. These examples suggests a potential albedo bias in the CH_4 retrievals, which will be investigated in Sect. 4.7.2. In addition, techniques for mitigating false positives will also be discussed in in Sect. 4.7.2

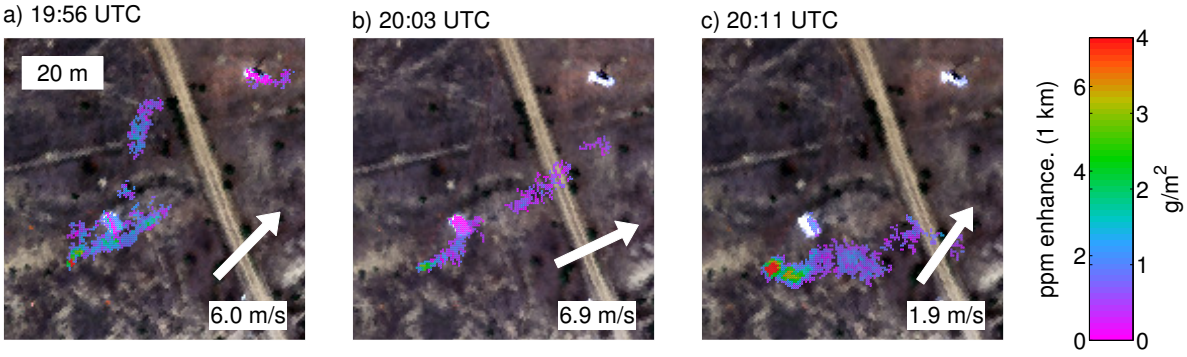

Figure 4.4. At site X-N with a 56.6 m^3/h (2,000 scfh) flux, AVIRIS-NG quantitative CH_4 retrievals are overlain on true color images. CH_4 enhancements are shown in g/m^2 and ppm (for a 1 km layer). For all scenes flight altitude was 0.58 km AGL, resulting in a pixel resolution of 0.5 m. Wind speed and direction (white arrow) were measured by nearby meteorological tower visible in the upper right portion of each scene. (a) At 19:56 UTC, plume appears consistent with the wind speed and direction, however, an apparent false positive is observed at the meteorological tower. (b) Plume appears elongated at higher wind speed (6.9 m/s) at 20:03 UTC compared to more compact appearance at lower wind speed (1.9 m/s) shown in (c) at 20:11 UTC.

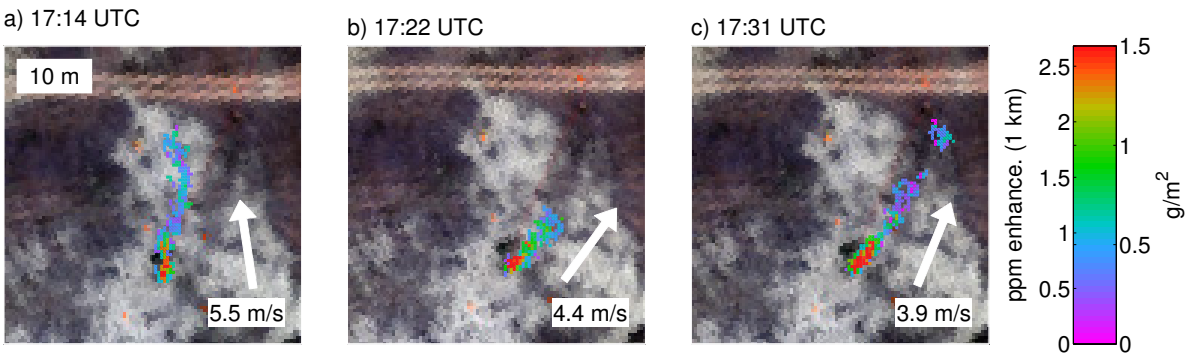

Figure 4.5. At site X-C with a 14.2 m^3/h (500 scfh) flux, AVIRIS-NG quantitative CH_4 retrievals are overlain on true color images. CH_4 enhancements are shown in g/m^2 as well as ppm (for a 1 km layer), and plumes appear consistent with the wind speed and direction measured by nearby meteorological towers (white arrows). For all scenes, flight altitude was 0.43 km above ground level (AGL) and the pixel resolution is 0.4 m. Plume shape and direction changes considerably between each scene imaged a few minutes apart. (a) 17:14 UTC. (b) 17:22 UTC. (c) 17:31 UTC.

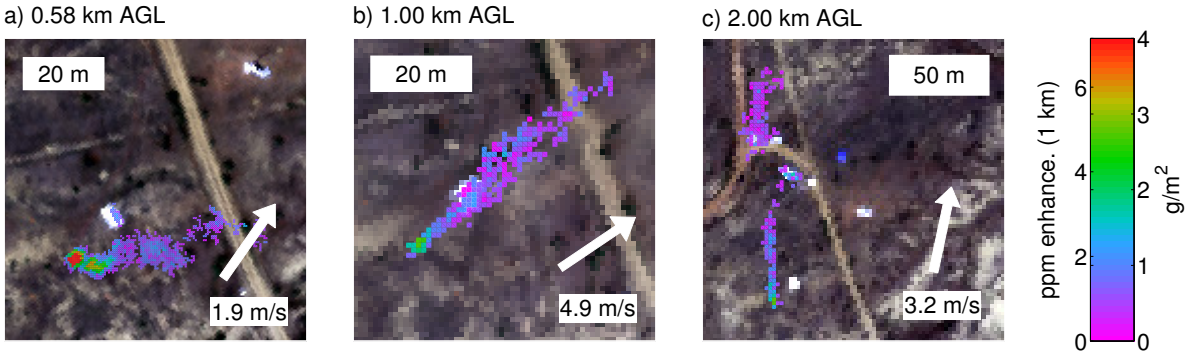

Figure 4.6. At site X-N with a 56.6 m^3/h (2,000 scfh) flux, AVIRIS-NG quantitative CH_4 retrievals are overlain on true color images for three flight altitudes. (a) 0.58 km AGL. (b) 1.00 km AGL. (c) 2.00 km AGL. CH_4 enhancements are shown in g/m^2 and ppm (for a 1 km layer). Plumes appear consistent with the wind speed and direction measured by nearby meteorological towers (white arrows). Detection at multiple flight altitudes is a prerequisite for monitoring large areas.

In Fig. 4.5, 3 plumes are visible at location X-C for a flux rate of 14.2 m^3/h (500 scfh). These scenes were acquired a few minutes apart at a flight altitude of 0.43 km AGL (0.4 m pixel resolution) and the plumes appear consistent with the wind speed and direction measured by nearby meteorological towers (Fig. 4.5, white arrows). For these examples, observed plume lengths are on the order of 10 to 20 m (Fig. 4.5) and the maximum observed concentration

is 2.66 ppm (1.49 g/m^2). As expected, these values are lower than those for the 3 higher flux examples (56.6 m^3/h, 2,000 scfh) show in Fig. 4.4. In addition, AVIRIS-NG consistently observed CH4 plumes at multiple flight altitudes. This is important because increasing flight altitude improves ground coverage, which would be an important prerequisite for monitoring large areas. In Fig. 4.6, plumes are shown at site X-N with a 56.6 m^3/h (2,000 scfh) flux for 0.58, 1.00, and 2.00 km AGL.

4.7.2 Residual and radiance analysis

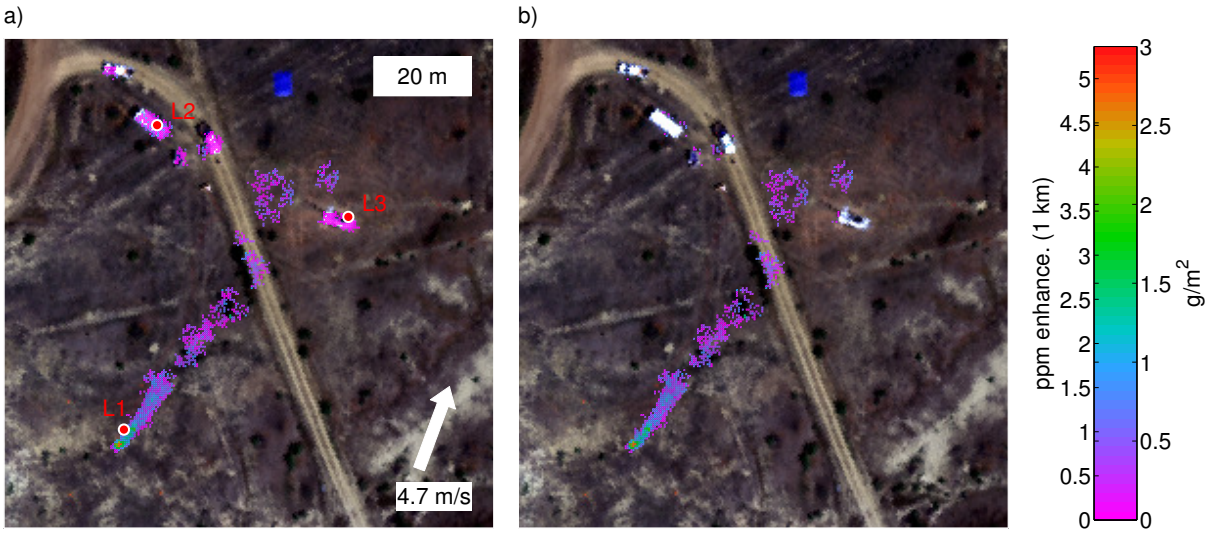

Figure 4.7. (a) CH_4 retrieval results for a 70.8 m^3/h (2,500 scfh) flux. AVIRIS-NG quantitative CH_4 retrievals are overlain on true color images and shown in g/m^2. L1 corresponds to a CH_4 enhancement downwind of release point, L2 to a false positive caused by trailer tank, and L3 to a second false positive caused by meteorological tower. Plume appears consistent with the wind speed and direction measured by nearby meteorological tower (white arrows). (b) False positives were reduced by using a residual mask to exclude poor fits.

As shown in Sect. 4.7.1, AVIRIS-NG consistently observed CH_4 plumes at multiple flux rates and altitudes, but false positives were also observed in some cases. To investigate methods for mitigating false positives, a residual analysis was performed for scenes acquired with a 70.8 m^3/h (2,500 scfh) flux at 0.43 km AGL (0.4 m pixel resolution). In Fig. 4.7a, CH_4 retrieval

results clearly indicate a plume and location L1 corresponds to a CH_4 enhancement downwind of the release point. In Fig. 4.8a, modeled (red) and measured standardized radiance (black) is shown for location L1 and the lower residual plot (measured minus modelled) indicates good agreement. However, false positives appear for the trailer tank (location L2) and meteorological tower (location L3). In Fig. 4.8b, measured and modelled radiance is shown for location L2 and the lower residual plot indicates disagreement in band 4 of the fitting window (2,296 nm). In Fig. 4.8c, the results shown for location L3 indicate the most significant disagreement between measured and modelled radiance at band 14 of the fitting window (2,346 nm).

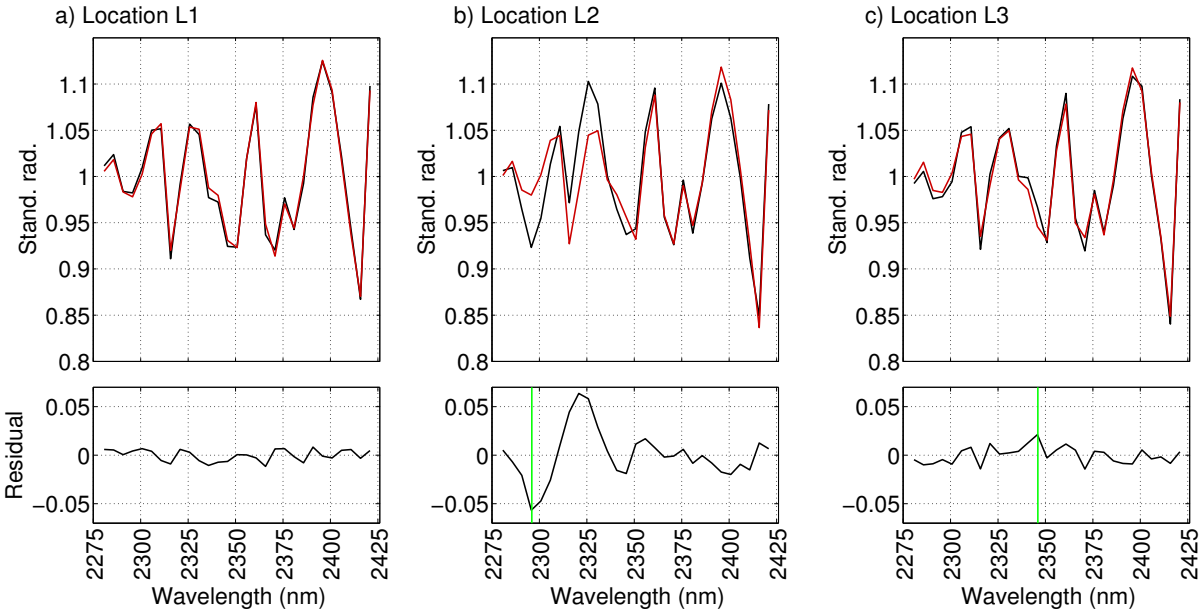

Figure 4.8. (a) The modeled (red) and measured (black) standardized radiance for location L1, which corresponds to a CH_4 enhancement downwind of release point (see Fig. 4.7a) and good agreement between modeled and measured radiance. Lower residual plot (measured minus modelled) further emphasizes agreement. (b) Location L2 corresponds to a false positive caused by trailer tank. Residual plot indicates disagreement for band 4 at 2,296 nm of standardized radiance (see green line). (c) For location L3, a second false positive caused by meteorological tower. Residual plot indicates disagreement for band 14 at 2,346 nm (see green line).

These characteristic features observed in residuals for surfaces that cause false positives

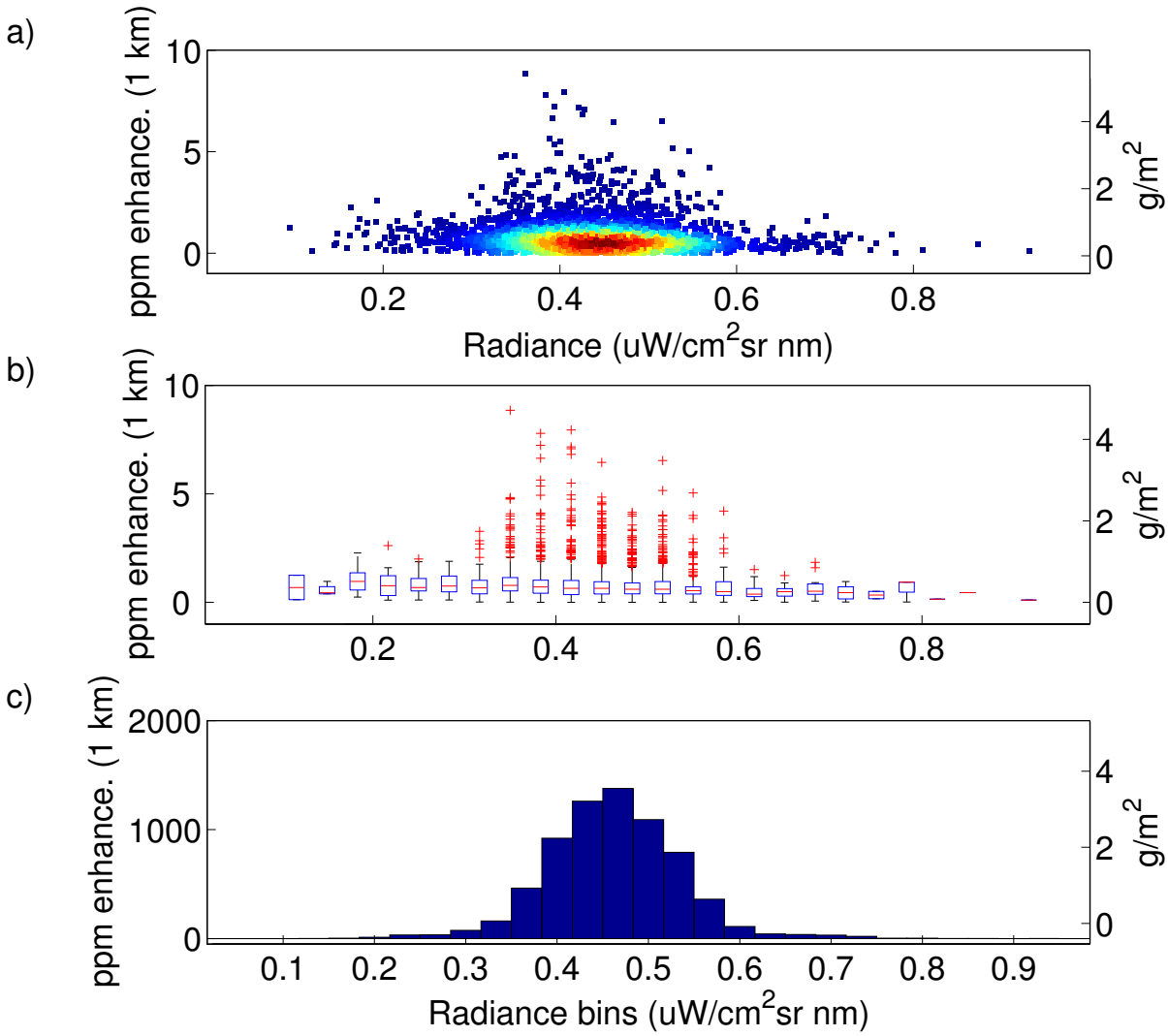

Figure 4.9. AVIRIS-NG retrieval results for 6 scenes have been combined to show the relationship between radiance level at band 1 of the fitting window (2,278 nm) and retrieved CH_4 concentrations. All retrievals were for 70.8 m^3/h (2,500 scfh) flux and a 0.43 km AGL flight altitude. (a) Scatterplot with a color overlay indicating that the highest density of points is around 0.45 $\mu W cm^{-2} sr^{-1} nm^{-1}$. (b) Boxplot generated for radiance bins and their associated CH_4 enhancement for each bin, with central red mark indicating the median (excluding outliers), the edges of the blue box are the 25th and 75th percentiles, and outliers are plotted as red crosses (which represent CH_4 enhancements). Median values across the entire range of radiance bins appears quite consistent and indicates that a significant retrieval bias is not present. (c) Histogram of aggregate results.

can be used to exclude poor fits and ultimately reduce false positives in the CH_4 results. To do so, an image mask was generated by first isolating pixels that either had residual values below -0.02 for band 4 (2,296 nm of standardized radiance) or above 0.015 for band 14 (2,346

nm). This isolated regions of false positives for the trailer tank and meteorological tower respectively. Next, a buffer of 1 pixel was applied to ensure the edges of false positives were also isolated. Finally, negative values that also correspond to a few pixels appearing as false positives were added to the mask. The resulting image mask was applied to the results shown in Fig. 4.7a to generate Fig. 4.7b where the false positives have been excluded.

This technique was applied to 6 AVIRIS-NG retrieval results for a 70.8 m^3/h (2,500 scfh) flux and a 0.43 km AGL flight altitude. In Fig. 4.9, results from the 6 AVIRIS-NG retrievals were combined and plotted to investigate the relationship between radiance level at band 1 of the fitting window (2,278 nm) and retrieved CH_4 concentrations. In Fig. 4.9a, a scatterplot was generated with a color overlay indicating that the highest density of points is around $0.45\,\mu W cm^{-2} sr^{-1} nm^{-1}$. In Fig. 4.9c, the histogram also clearly indicates a maximum count around $0.45\,\mu W cm^{-2} sr^{-1} nm^{-1}$, with counts decreasing on either side. In Fig. 4.9b, a boxplot was generated for radiance bins and their associated CH_4 enhancement for each bin, with central red marks indicating the median (excluding outliers), the edges of the blue boxes as the 25th and 75th percentiles, and outliers as red crosses (which represent CH_4 enhancements). Overall, median values across the entire range of radiance bins appears quite consistent and indicates that a significant retrieval bias is not present.

4.7.3 Summary of all results

For the flight campaign, AVIRIS-NG was flown at 0.43, 0.58, 1.10, 2.00, and 3.80 km above ground level (AGL) with spatial resolutions of 0.4, 0.5, 1.0, 1.9, and 3.6 m for each image pixel, respectively. All AVIRIS-NG results are summarized in Fig. 4.10 for a range of flux rates and wind speeds. A segmentation approach based on 8-connectivity was used to isolate adjacent

pixels of the CH_4 plume (see Sect. 4.6). Segmentation used matched filter scores greater than 2 (scores are standardized, so greater than 2 standard deviations) and a minimum of 16 adjacent pixels. This criteria permitted automatic detection by the algorithm, denoted as green circles in Fig. 4.10. Green crosses indicate partial detections (requiring user interpretation) and non-detections are shown as red circles.

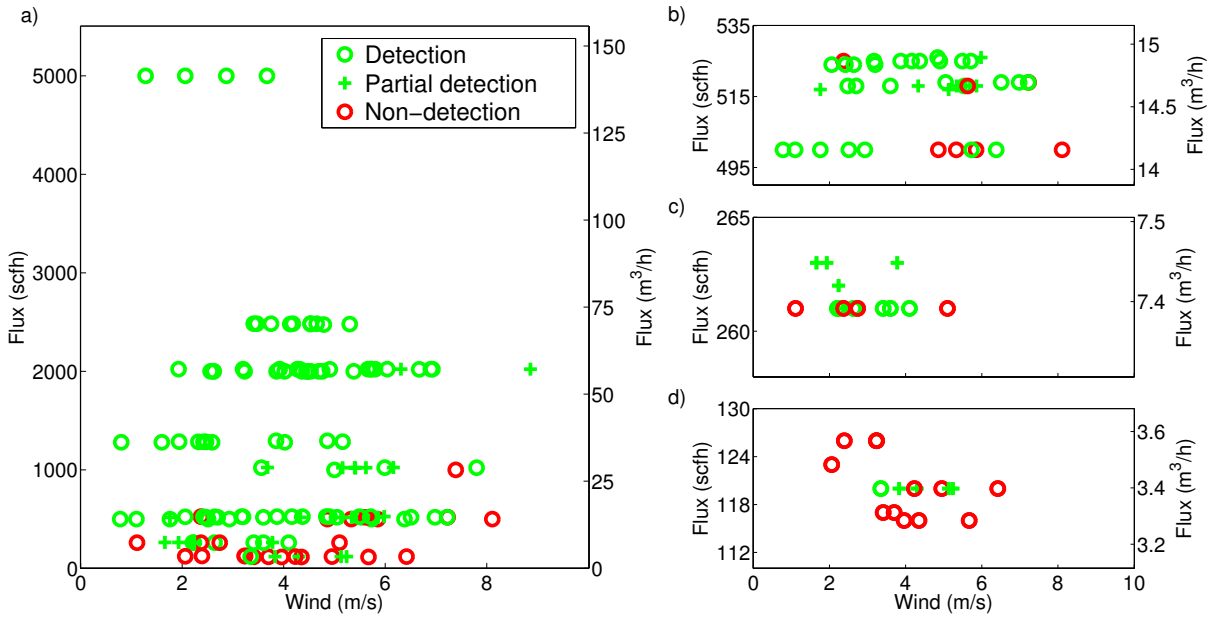

Figure 4.10. (a) For all flights (multiple altitudes) for entire range of flux rates and wind speeds, detections indicated by green circles (automatic detection by algorithm), green crosses denote partial detections (requiring user interpretation), and non-detections shown as red circles. Results for lower fluxes ranges are included in (b), (c), and (d).

The results in Fig. 4.10 indicate that AVIRIS-NG consistently detected CH_4 plumes for a range of flux rates and wind speeds. This trend is observed in Table 4.1, where detection percentages are calculated for each flux range and the majority are detections for flux ranges greater than 301 scfh (8.5 m^3/h). As seen in Fig. 4.10b, c, and d, non-detections increase as fluxes decreases to around 515 scfh (14.58 m^3/h), 263 scfh (7.45 m^3/h) and 120 scfh (3.40 m^3/h). This trend is more clearly represented in Table 4.2, where non-detections increased to 15.6%, 26.7%, and 70.6% respectively for the 700-301 scfh (19.8-8.5 m^3/h), 300-151 scfh (8.4-4.3 m^3/h)

and 150-0 scfh (4.2-0.0 m^3/h) categories.

	Count	% total	Count	% total	Count	% total	Count	% total
	6000-3001 scfh (169.9-85.0 m^3/h)		3000-2201 scfh (84.9-62.3 m^3/h)		2200-1701 scfh (62.2-48.2 m^3/h)		1700-701 scfh (48.1-19.9 m^3/h)	
Detection	4	100.0%	10	100.0%	28	93.3%	15	68.2%
Partial	0	0.0%	0	0.0%	2	6.7%	6	27.3%
Non-detection	0	0.0%	0	0.0%	0	0.0%	1	4.5%
Total	4	100.0%	10	100.0%	30	100.0%	22	100.0%

	Count	% total	Count	% total	Count	% total
	700-301 scfh (19.8-8.5 m^3/h)		300-151 scfh (8.4-4.3 m^3/h)		150-0 scfh (4.2-0.0 m^3/h)	
Detection	30	66.7%	6	40.0%	1	5.9%
Partial	8	17.8%	5	33.3%	4	23.5%
Non-detection	7	15.6%	4	26.7%	12	70.6%
Total	45	100.0%	15	100.0%	17	100.0%

Table 4.1. AVIRIS-NG detections by flux range.

	Count	% total	Count	% total	Count	% total	Count	% total	Count	% total
	0.00 to 1.99 m/s		2.00 to 3.99 m/s		4.00 to 5.99 m/s		6.00 to 7.99 m/s		8.00 to 10.00 m/s	
Detection	8	66.7%	36	70.6%	38	63.3%	9	64.3%	0	0.0%
Partial	3	25.0%	5	9.8%	13	21.7%	2	14.3%	1	50.0%
Non-detection	1	8.3%	10	19.6%	9	15.0%	3	21.4%	1	50.0%
Total	12	100.0%	51	100.0%	60	100.0%	14	100.0%	2	100.0%

Table 4.2. AVIRIS-NG detections by wind speed range.

Wind speed has been shown to influence the shape of plumes, for example lower wind speeds result in a more compact shape with higher maximum CH_4 concentrations (see Sect. 4.7.1). Therefore, lower wind speeds should improve detection percentages by permitting higher concentrations of CH_4 to build up downwind of the release point. To investigate

this, detection percentages were calculated for a number of wind speed ranges in Table 4.2. However, the percentage of detection is quite similar (63.3 to 70.6%) across most wind conditions (0.00 to 7.99 m/s). For winds between 8.00 to 10.00 m/s, the detection percentage drops to 0% with a 50% partial detection rate (note small sample size of 2 examples). Given these results, it appears that flux rate has the greatest influence on percentage of detection while the influence of winds is less clear.

In Fig. 4.11, plume area and maximum plume length are shown as a function of flux and wind speed. As expected, plume area (Fig. 4.11a) and plume length (Fig. 4.11b) both clearly increase with higher flux rates, while wind speed has a lesser influence. For moderate flux rates (25 to 75 m^3/h) in both examples, there appears to be a local maximum for moderate wind speeds (2 to 6 m/s). This could be explained by the observation that low wind speed (less than 2 m/s) leads to more compact plumes (smaller area and plume length) than for moderate wind speed (see Sect. 4.7.1). In addition, higher winds (greater than 6 m/s) would lead to increased advection of CH_4 downwind and likely result in lower concentrations that AVIRIS-NG is incapable of detecting, thereby generating smaller plume areas and lengths than for moderate wind speeds. The observed relationship between plume area or plume length to flux and wind speed offers the potential to constrain fluxes during future AVIRIS-NG flight campaigns. To do so, empirical results from the RMOTC campaign or results from plume dispersion models could be used to generate a lookup table similar to that shown in Fig. 4.11. For observed AVIRIS-NG plumes, total area and plume length can be first calculated and the flux rate could be constrained based on the lookup table and some knowledge of local wind conditions.

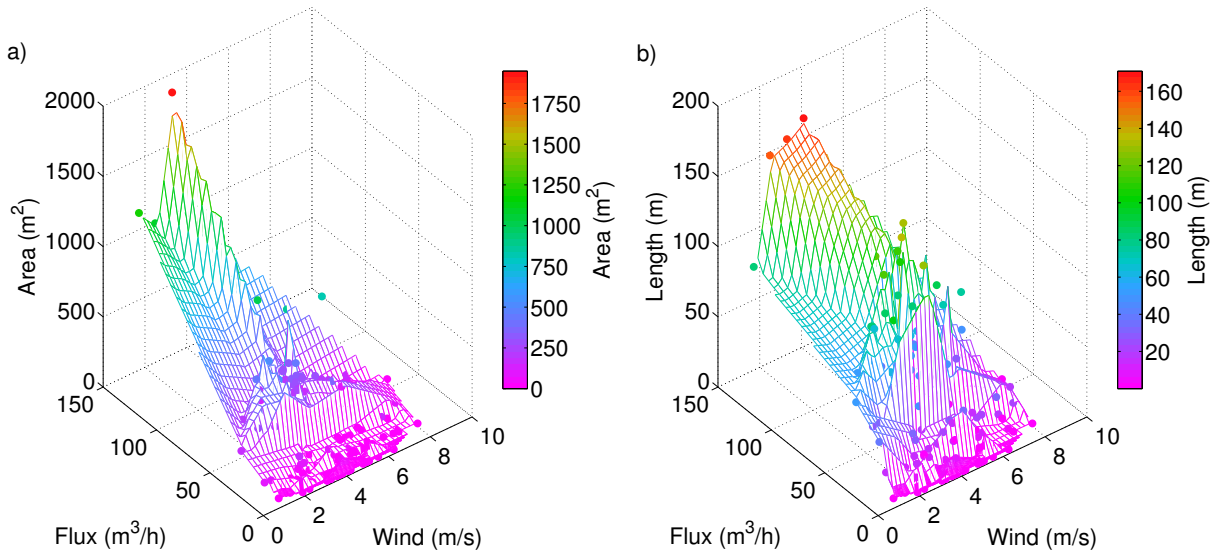

Figure 4.11. (a) Observed plume area is shown as a function of flux and wind speed. (b) Maximum plume length also increases with higher flux rates, while wind speed has a lesser influence on total length. These 2 relationships offer the potential to constrain fluxes using AVIRIS-NG results.

4.8 Discussion and conclusion

This controlled release experiment has demonstrated that AVIRIS-NG is capable of detecting CH_4 plumes for a range of fluxes using a matched filter approach. Plumes were consistently observed between 14.16 and 141.58 m^3/h (500 and 5,000 scfh) for wind conditions that ranged from 0.5 to 9 m/s (Fig. 4.10a). Below 14.16 m^3/h, the percentage of detections decreases, however, plumes were observed as low as 3.40 m^3/h (120 scfh) (Fig. 4.10d). Observed plume shapes and orientations were broadly consistent with wind direction and higher winds produced elongated plumes compared to a more compact appearance at lower wind speeds. In addition, AVIRIS-NG observed plumes at altitudes ranging from 0.43 to 3.80 km AGL, resulting in spatial resolutions between 0.4 and 3.6 m per pixel. Sensitivity at the higher flight altitudes is particularly important given increased ground coverage is a prerequisite for future flight campaigns focused on detecting point source emissions over large areas. The re-

sults from the RMOTC experiment indicate the potential for using imaging spectrometers like AVIRIS-NG for detection of CH_4 plumes and to directly attribute emissions to individual point source locations across a range of CH_4 flux rates and wind conditions.

Quantitative CH_4 retrieval results consistently indicated highest concentrations near the release point with values decreasing downwind. As seen with the matched filter detections, quantitative retrievals performed well for multiple flux rates, wind conditions, and flight altitudes. There was overall good agreement between measured and modelled radiances, but in some instances for specific surfaces like the tube trailer and meteorological tower fits were poor. In these cases, false positive were observed and residual based masks applied to exclude false positives from retrieval results. This type of false positive mitigation could be particularly useful for extended monitoring campaigns to improve the accuracy of detections and to reduce ambiguity for high-altitude observations that have less context to interpret surface features. AVIRIS-NG retrievals were combined and plotted to investigate the relationship between radiance level and retrieved CH_4 concentrations (Fig. 4.9) and do not indicate a retrieval bias.

AVIRIS-NG detected plumes for the entire range of fluxes used during the controlled release experiment, between 3.40 and 141.58 m^3/h (120 and 5,000 scfh). For comparison, published values for fugitive CH_4 from natural gas production are shown in Fig. 4.12. Fluxes are listed in m^3/h on a logarithmic scale and are shown as ranges (grey bars) or mean values (black lines). Flux rates vary considerably from 0.05 to 0.58 m^3/h for pneumatic controller (Allen et al. 2015a) to between 6.66 and 1,633.65 m^3/h for liquid unloadings for gas wells without plunger lifts (Allen et al. 2015b). It is important to note that for each source category

there is likely significant variability and uncertainty in published results, so these examples should not be viewed as definitive or comprehensive.

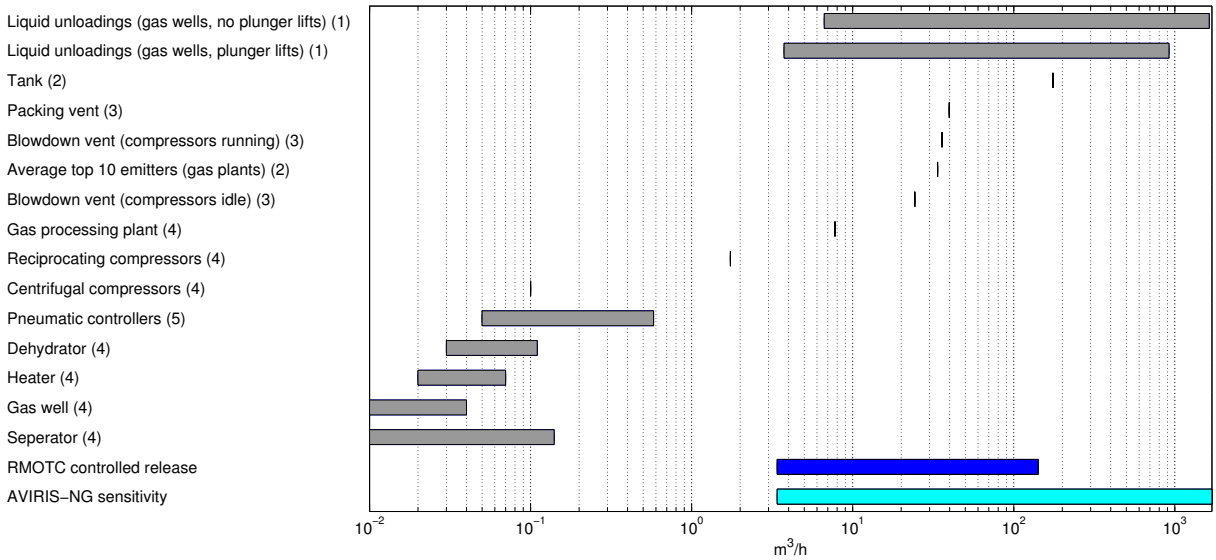

Figure 4.12. Published values of fugitive CH_4 from natural gas production in m^3/h. Multiple emission categories are listed with sources referenced by numbers in parentheses as follows: (1) (Allen et al. 2015b), (2) (EPA 2006), (3) (EPA 2010), (4) (EPA 2014), (5) (Allen et al. 2015a). Values are shown as ranges (grey bars) or mean values (black lines). For each source category there is significant variability and uncertainty. Range of fluxes used for RMOTC controlled release is shown in blue. Cyan bar represents AVIRIS-NG detection capability based on results from controlled release (above 3.40 m^3/h, 120 scfh). AVIRIS-NG was not designed for CH_4 detection, but offers the potential for monitoring a number of source categories. Calculated fluxes from Allen et al. (2015b) assume average 1.51 hour event for gas wells with plunger lifts and 2.34 hour event with no plunger lifts.

The range of fluxes tested at RMOTC are shown by the blue bar and the AVIRIS-NG sensitivity is shown in cyan, including fluxes higher than those tested at RMOTC. This indicates AVIRIS-NG can be used to detect plumes from some of the larger emission sources in existing gas fields. For example, a study by the EPA (2006) listed a 33.68 m^3/h average flux rate from the top 10 emitters for a number of gas processing plants, which is well within the detection capability of AVIRIS-NG. In addition, CH_4 plumes from liquid unloadings, tanks, some vents, and gas processing plants should be visible using AVIRIS-NG.

Since the RMOTC experiment, a new detector array with improved quantum efficiency

has been installed in AVIRIS-NG. This along with additional enhancements in spectral alignment and calibration are expected to improve the CH_4 sensitivity of AVIRIS-NG. In addition, real time detection of CH_4 plumes has been implemented using an operator interface that overlays plumes on a true color image acquired by AVIRIS-NG (Thompson et al. submitted). This has facilitated surveys over existing oil and gas fields to identify and attribute CH_4 emissions to individual point sources, including wells (Thompson et al. submitted) and well pads known to use hydraulic fracturing for natural gas extraction (Aubrey et al. 2015).

Despite these promising results, it is important to emphasize that AVIRIS-NG was not designed for CH_4 detection and the moderate spectral resolution can cause false positives. An imaging spectrometer built exclusively for detection, quantification, and attribution of CH_4 plumes would have improved sensitivity compared to AVIRIS-NG (Thorpe et al. 2014). To that end, an instrument concept is currently being developed that uses an imaging spectrometer with finer spectral resolution for improved CH_4sensitivity. This would permit detection of smaller point sources and more diffuse emissions and entirely decouple the spectroscopy of terrestrial surfaces and the atmosphere, virtually eliminating false positives.

Recent studies have suggested that a small number of 'super emitters' are responsible for the majority of fugitive emissions from natural gas systems and production sites (Brandt et al. 2014; Caulton et al. 2014; Allen et al. 2015a; Allen et al. 2015b). Results from the RMOTC controlled release experiment as well as subsequent surveys over oil and gas fields indicates that AVIRIS-NG is capable of detecting the super emitters. One benefit of imaging spectrometers is they provide the ability to rapidly image large areas with the high spatial resolution required to locate emissions and attribute emissions to individual point sources.

This offers the potential to effectively mitigate the impacts of fugitive CH_4 on global climate by identifying leaks and communicating these with site operators of oil and gas fields.

Overall oil and gas production is projected to increase steadily and natural gas production is expected to increase 44% between 2011 and 2040 (EIA 2013). This projected growth will primarily result from increased development of shale gas, tight gas, and coalbed CH_4 often using enhanced recovery techniques like hydraulic fracturing and horizontal drilling (EPA 2014). Accordingly, fugitive CH_4 emissions are expected to rise (Caulton et al. 2014) and the ability to identify these emission sources will be of even greater importance.

4.9 Acknowledgments

The authors thank the AVIRIS/AVIRIS-NG team at JPL, additional collaborators at LANL, the Chevron Energy Technology Company, and the U.S. Department of Energy for use of RMOTC. Special thanks to Martin Evans, Lance Christensen, Glynn Hulley, Pierre Guillevic, and Simon Hook for their support of the project. Portions of this research were supported by NASA Headquarters under the NASA Earth and Space Science Fellowship Program grant NNX13AM95H as well as the Chevron Energy Technology Company. This work was undertaken in part at the Jet Propulsion Laboratory, California Institute of Technology, under contract with NASA as well as at the University of California, Santa Barbara. The AVIRIS-NG data used in this study are available upon request at http://avirisng.jpl.nasa.gov/ or http://aviris.jpl.nasa.gov/.

Chapter 5

Conclusions

5.1 Summary of research

This dissertation has focused on developing techniques for detecting and quantifying CH_4 enhancements using airborne imaging spectrometers like AVIRIS and AVIRIS-NG. In Chapter 2, a non-quantitative Cluster-Tuned Matched Filter (CTMF) approach (Funk et al. 2001) was adapted for use with AVIRIS data acquired over marine and terrestrial environments known to emit CH_4. The CTMF was trained with a gas target spectrum to calculate CTMF scores for each image pixel where scores greater than one indicate significant evidence of the gas signature. The CTMF uses the inverse of the scene's covariance structure to remove large-scale noise to isolate the gas signal, so it is best suited for detecting concentrated sources rather than background concentrations.

In a high sunglint scene, CH_4 anomalies were clearly visible at the Coal Oil Point seep field near Santa Barbara, CA, a large emission source estimated at 100,000 m^3/day (Hornafius et al. 1999). The observed anomalies were consistent with known seep locations and local wind direction, extending more than 1 km downwind. The CTMF results were also in good agreement with those obtained using the non-quantitative AVIRIS CH_4 index, a band

ratio developed by Bradley et al. (2011). However, CTMF sensitivity appears greater than the AVIRIS CH_4 index thereby permitting improved ability to detect the plume. The CTMF was also applied to two AVIRIS flight lines west of downtown Los Angeles. Significant CH_4 anomalies were identified for known sources at the La Brea Tar Pits and in close proximity to probable sources, including an office complex documented as venting CH_4 continuously and likely fugitive CH_4 emissions from hydrocarbon tanks on the Inglewood Oil Field. The plume emanating from the hydrocarbon tanks extended 0.1 km downwind and was observed to change shape in the 6.5 minutes between two scenes. This represents the first detection of fugitive CH_4 using AVIRIS data.

Interpretation of anomalies was complicated by noise and false positives for surfaces with strong absorptions at the same wavelengths as CH_4 absorption features, like hydrocarbons, oil-based paints, calcite, and asphalt. To address false positives, segmentation of results was first used to identify distinct locations of contiguous pixels with high CTMF scores. Segments were then classified into probable CH_4 anomalies and confusers based on the spectral properties of the underlying surface over the full spectral range measured by AVIRIS. In Appendix A, the CTMF was also applied to additional trace gasses like CO_2 that permitted detection of a CO_2 plume from a fossil-fuel power plant.

Using the same AVIRIS scenes for COP and the Inglewood Oil Field, two quantitative CH_4 retrieval algorithms were developed in Chapter 3. The iterative maximum a posteriori differential optical absorption spectroscopy (IMAP-DOAS) algorithm, originally developed for the satellite sensor SCIAMACHY (Frankenberg et al. 2005b), was adapted for use with AVIRIS. The IMAP-DOAS algorithm uses optimal estimation theory to adjust the slant col-

umn densities of multiple gasses until total optical density fits the observed measurement. As part of this algorithm, CH_4 Jacobians (change in atmospheric transmission with respect to a change in gas concentration) and a retrieved CH_4 scaling factor are calculated, thereby permitting quantification of observed CH_4 enhancements. The IMAP-DOAS technique performed well for the high sunglint ocean scene for COP resulting in plumes consistent with previous studies (Bradley et al. 2011; Thorpe et al. 2013). IMAP-DOAS retrieval precision errors are expected to equal between 0.31 to 0.61 ppm CH_4 over the lowest atmospheric layer (height up to 1.04 km). However, IMAP-DOAS results for the terrestrial scene were adversely influenced by the underlying land cover.

A hybrid approach using IMAP-DOAS and Singular Value Decomposition (SVD) was developed to better account for spectral variability in surface reflectance. SVD transforms a large number of potentially correlated vectors into a smaller set of uncorrelated (orthogonal) vectors, denoted as singular vectors. This technique allows determination of how much of the observed radiance for each spectrum can be associated with the CH_4 Jacobian (changes in absorptions due to CH_4) and can be used to estimate CH_4 concentrations. Using this hybrid approach, maximum near surface enhancement were 2.85 and 8.45 ppm CH_4 above background (averaged over a 1.04 km subcolumn) respectively for the COP and Inglewood plumes.

Both the IMAP-DOAS and hybrid approaches permit uncertainty estimation by calculating the standard deviation of the residual (the difference between measured and modeled radiance) to evaluate the ability of each algorithm to model radiance. This technique can also be used to identify land cover types that are problematic and exclude poor fits to im-

prove retrieval results. Using the IMAP-DOAS technique at COP, bright pixels (greater than $5\,\mu Wcm^{-2}sr^{-1}nm^{-1}$ in the fitting window) resulted in poor fits (high standard deviation of the residual). In contrast, dark pixels (less than $0.1\,\mu Wcm^{-2}sr^{-1}nm^{-1}$) resulted in poor fits for the Inglewood plume. Dark pixels were problematic for the hybrid approach as well, further emphasizing that their correspondingly low signal to noise ratio causes lower single measure precision for both retrieval techniques.

Finally, a sensitivity analysis indicates CH_4 sensitivity should be more than doubled for the next generation AVIRIS sensor (AVIRIS-NG) due to improved spectral resolution. Therefore, AVIRIS-NG should be better suited for mapping both CH_4 and CO_2 plumes from concentrated point sources. However, sensors with a finer spectral resolution (1 nm) offer far greater sensitivity and would be better suited for constraining emissions on local and regional scales, including sources of increasing concern like fugitive CH_4 from the oil and gas industry.

As part of my dissertation research, I participated in a controlled CH_4 release experiment performed over seven days (20-26 June 2013) at the Rocky Mountain Oilfield Testing Center (RMOTC), a Department of Energy facility located approximately 30 miles northeast of Casper, Wyoming. This included campaign planning, experiment setup, and data analysis. Over six flight days CH_4 was released at all sites, with metered flux rates ranging between 3.40 and 141.58 m^3/h (120 and 5,000 standard cubic feet per hour, scfh). During the flight campaign, a total of 55 flight lines were acquired during the experiment at altitudes ranging between at 0.43 and 3.8 km above ground level (AGL).

In Chapter 4, AVIRIS-NG results from the RMOTC experiment were discussed. Flight lines were processed using both the non-quantitative matched filter and quantitative hybrid

approaches. There was consistent detection down to 14.16 m^3/h (500 scfh) for multiple flight altitudes and detection as low as 3.40 m^3/h (120 scfh). Results from the RMOTC controlled release experiment indicate that AVIRIS-NG has the capability of detecting a number of fugitive CH_4 source categories for natural gas fields.

5.2 Potential application

Although AVIRIS and AVIRIS-NG were not designed for gas detection, they appear well suited for attribution and quantification of CH_4 emissions from concentrated point sources. The published research as part of this dissertation focused on CH_4 from natural marine and terrestrial sources (Thorpe et al. 2013), wastewater treatment (Thorpe et al. 2012), and fugitive CH_4 from the oil and gas industry (Thorpe et al. 2014). However, there is potential application to other CH_4 sources like landfills, coal mines (Krings et al. 2013), and coal bed CH_4 (Kort et al. 2014). Additional studies have shown great potential for trace gasses like CO_2 (Dennison et al. 2013) and water vapor (Ogunjemiyo et al. 2002). More recent studies (Thompson et al. submitted; Aubrey et al. 2015) indicate the potential of AVIRIS-NG for detecting fugitive CH_4 from active oil and gas fields (Fig. 5.1, Fig. 5.2).

There is considerable disagreement over the contribution of fugitive CH_4 from oil and gas sectors to the CH_4 budget. Multiple top-down estimates suggest fugitive CH_4 emissions from natural gas and oil production can be large, ranging between 2.3 to 7.0% of CH_4 produced annually for the Denver-Julesburg Basin, Colorado (Petron et al. 2012) and between 6.2 to 11.7% of average hourly natural gas production in the Uintah County oil and gas field (Karion et al. 2013). These estimates pertain to specific locations and times, while leak rates from different facilities should vary considerably. For example, additional studies suggest that

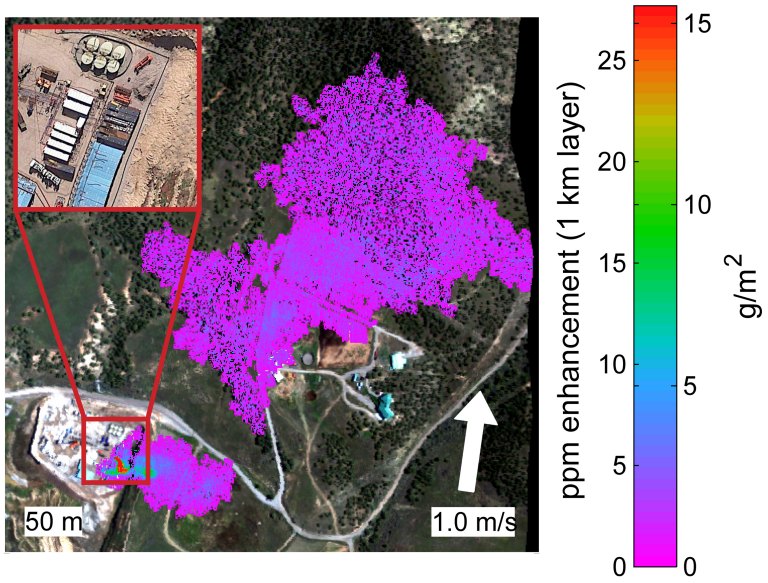

Figure 5.1. AVIRIS-NG true color image subset with superimposed CH_4 plume from September 2014 flight in Garfield County, Colorado. Plume extends over 600 m downwind of the emission source. Google Earth imagery with finer spatial resolution is also included from June 2014 (red box), however, the high density of infrastructure makes the primary emission source unclear. The blue modular units seen in Google Earth imagery are 'Frac Tanks,' which can be used to store fresh or produced water.

fugitive CH_4 leakage is considerably lower (Allen et al. 2013; Alvarez et al. 2012; O'Sullivan and Paltsev 2012).

There is also high variability in estimated leak rates from different facilities for individual sites and from different methods of extraction such as traditional versus non-conventional drilling. In the U.S., published CH_4 emission losses for individual wells are generally small but vary regionally, for example 0.059 m^3/h CH_4 (2.10 scfh) for the Rocky Mountain States up to 0.167 m^3/h (5.88 scfh) for the Appalachian States (EPA 2014). A recent study of pneumatic controllers found average emission rates that were generally low, ranging from 0.049 to 0.580 m^3/h (1.72 to 20.5 scfh) for four regions in the U.S. (Allen et al. 2014a). In contrast, gas processing plants and compressor stations have higher average loss rates, on the order of 9.328 to 9.730 m^3/h (329.42 to 343.61 scfh) respectively (EPA 2014). Loss rates as high as

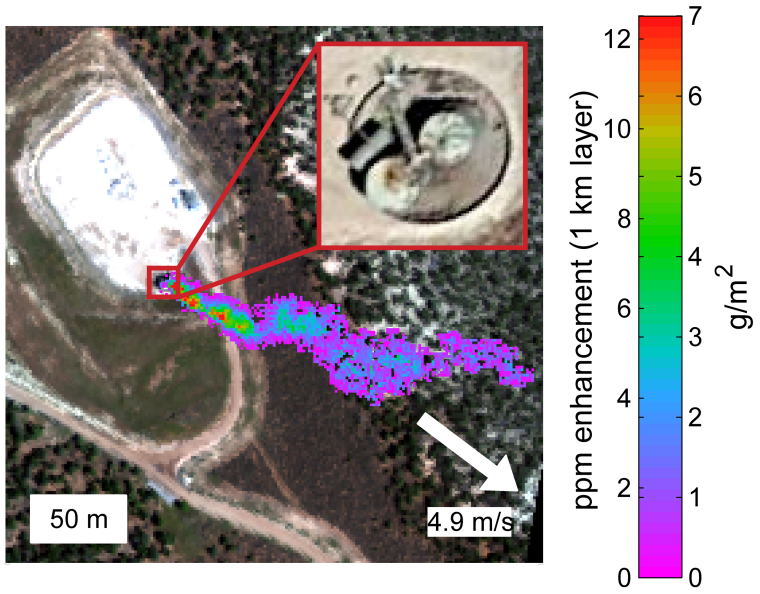

Figure 5.2. AVIRIS-NG true color image subset with superimposed CH_4 plume from September 2014 flight in Garfield County, Colorado. Plume extends 200 m downwind of the emission source. Google Earth imagery with finer spatial resolution is also included from June 2014 (red box), indicating that tanks are the likely CH_4 source. These tanks are likely either produced water storage tanks or condensate tanks.

262.950 m^3/h (9,286 scfh) have been reported for completion flowback events from hydraulic fracturing (Allen et al. 2013). Further, liquid unloadings for wells with plunger lifts averaged between 28.317 and 283.168 m^3/h (1,000 and 10,000 scfh) per event and increased to between 594.654 and 991.090 m^3/h (21,000 and 35,000 scfh) per event for wells without plunger lifts (Allen et al. 2014b). Recent studies have suggested that a small number of super emitters are responsible for the majority of fugitive emissions (Brandt et al. 2014; Caulton et al. 2014; Allen et al. 2014a; Allen et al. 2014b). For example, in one study, 58% of CH_4 losses were attributed to the 10 largest emitters, which ranged from 9.653 to 216.417 m^3/h (340.96 to 7,642.71 scfh) (EPA 2006b).

As shown in Chapter 4, results from the RMOTC field campaign indicated consistent detections at 14.2 m^3/h (500 scfh) and detections down to 3.4 m^3/h (120 scfh). Thus imaging spectrometers like AVIRIS-NG will be able to detect the super emitters, while some smaller

leaks could also be visible. Imaging spectrometers provide the ability to rapidly image large areas with the high spatial resolution required to attribute emissions to individual point sources (Fig. 5.3). This offers the potential to determine what proportion of oil and gas infrastructure represents the heavy tail of overall fugitive CH_4 emissions (for a given surveyed area, how many well pads are super emitters). These results could help constrain regional CH_4 budgets from the oil and gas sectors and explain observed discrepancies between bottom up emissions inventories and top down emission estimates (Brandt et al. 2014). Detection and quantification of fugitive CH_4 also offers the potential for direct mitigation of global warming by identifying leaks and communicating these with site operators of oil and gas fields. From the perspective of the oil and gas industry, these CH_4 emissions represent safety hazards, lost revenue, and a source for poor public relations. Given anticipated increased regulation of fugitive emissions, proactive identification and mitigation of fugitive CH_4 could also be advantageous.

Overall oil and gas production is projected to increase steadily and natural gas production is expected to increase 44% between 2011 and 2040 (EIA 2013). This projected growth will primarily result from increased development of shale gas, tight gas, and coalbed CH_4 often using enhanced recovery techniques like hydraulic fracturing and horizontal drilling (EPA 2014). Accordingly, fugitive CH_4 emissions are expected to rise. For example, applying a 7% CH_4 loss rate to projected global increases in shale gas production results in an annual loss of 24 Tg CH_4, representing around 4% of the global CH_4 emissions from natural and anthropogenic sources (Caulton et al. 2014).

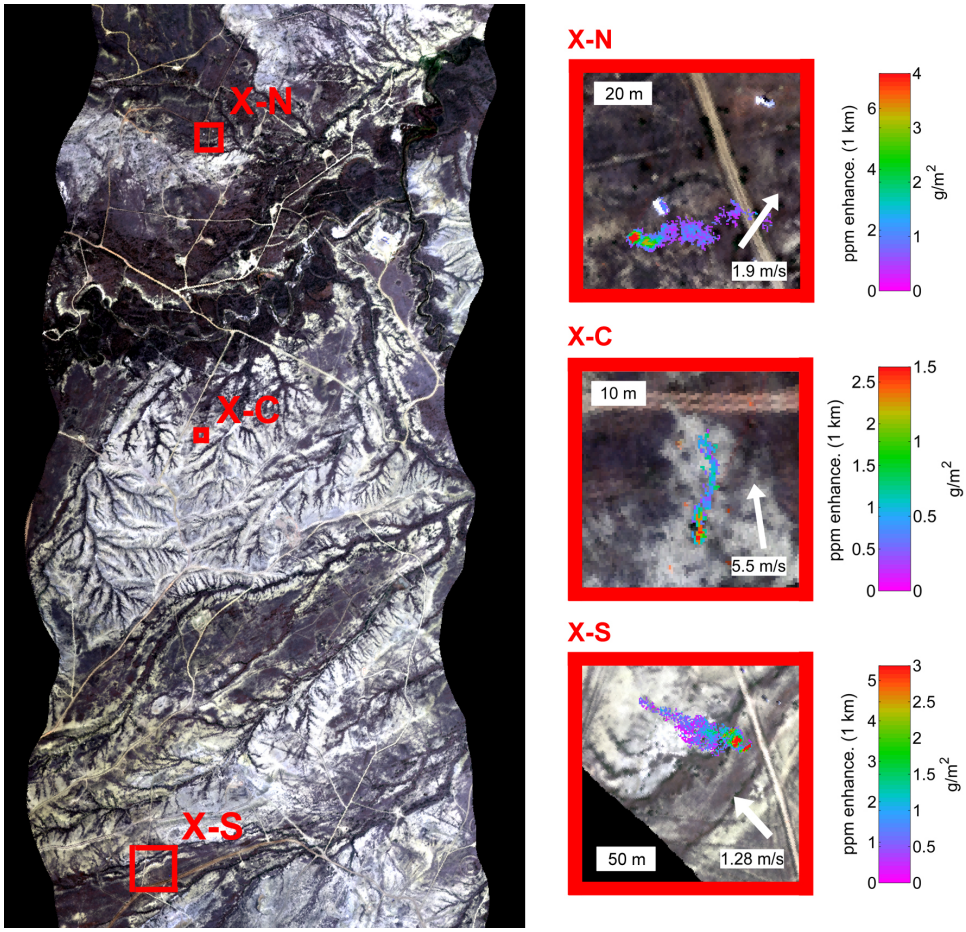

Figure 5.3. AVIRIS-NG true color image showing locations of three controlled release sites (X-N, X-C, X-S). Scene was acquired at 3.8 km AGL with a pixel resolution of 3.6 m and image swath of approximately 1.9 km. Three examples of CH_4 plumes are shown for different flux rates with concentrations shown both as ppm averaged over a 1 km layer and g/m^2. (top) 2,000 scfh flux (0.5 m pixel resolution, 0.58 km AGL). (center) 500 scfh flux (0.4 m pixel resolution, 0.43 km AGL). (bottom) 5,000 scfh flux (1.0 m pixel resolution, 1.1 km AGL).

5.3 Ongoing research and future directions

Published results from this dissertation have demonstrated the utility of using airborne imaging spectrometers for attributing CH_4 plumes to individual sources and quantifying CH_4 enhancements. However, false positives proved problematic for both AVIRIS and AVIRIS-NG because the spectral properties of the surface could not be entirely decoupled from atmospheric absorption features. To reduce false positives, a segmentation approach and land surface classification was developed in Chapter 2 and residual based masks were used in

Chapter 4. These existing techniques can be further improved and new techniques are currently being developed to better suppress false positives. As part of these efforts, ongoing work is focused on generating synthetic images with plumes of known gas concentration to further investigate false positives, detection limits, and the influence of albedo on both detection and quantification algorithms.

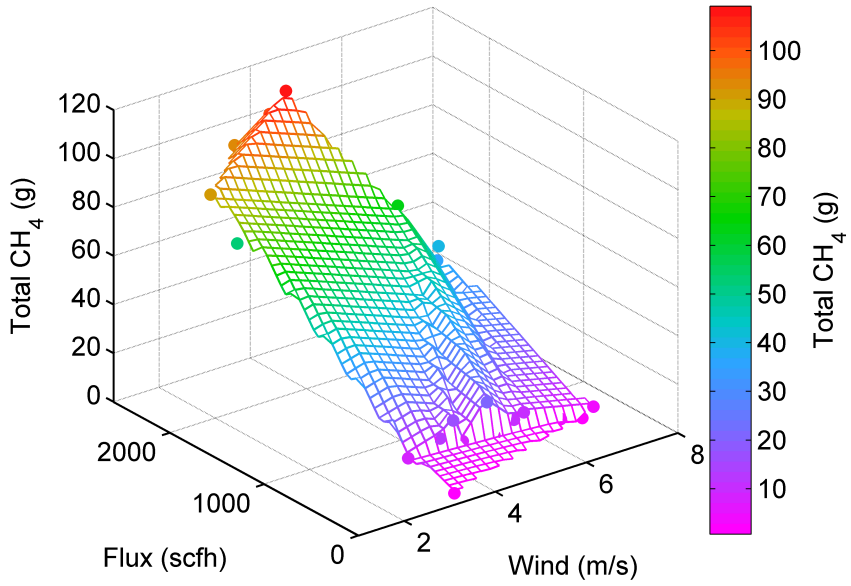

Figure 5.4. Observed total CH_4 is shown as a function of flux and wind speed. This relationship offers the potential to constrain fluxes using AVIRIS-NG CH_4 retrievals.

In Chapter 4, a strong relationship was observed between flux rates and both observed plume areas and plume lengths in AVIRIS-NG results. Further, ongoing work indicates that total CH_4 calculated for AVIRIS-NG retrievals increases with flux rate, while wind speed has a lesser influence (Fig. 5.4). This suggests that a mass balance technique, like those utilized since the 1970s (White et al. 1976) could be applied to AVIRIS-NG retrievals. This would permit leveraging the fully imaged plume to quantify the flux by measuring the total CH_4 added to the atmosphere from each point source, which is impossible to do with in situ measurements

that only sample portions of the plume and make assumptions about mixing.

These observed relationships between total CH_4, plume area, or plume length to flux and wind speed offers the potential to constrain fluxes during future AVIRIS-NG flight campaigns. To do so, empirical results from the RMOTC campaign or results from plume dispersion models could be used to generate a lookup table similar to that shown in Fig. 5.4. For observed AVIRIS-NG plumes, total CH_4, total area, or plume length can be first calculated and the flux rate could be constrained based on the lookup table and some knowledge of local wind conditions. In addition, simple flux calculations using measured wind speeds and orthogonal transects can also be used to calculate fluxes directly. As shown in Fig. 5.5, this technique was applied to one AVIRIS-NG CH_4 plume at RMOTC and resulted in a calculated flux in good agreement with the known flux rate. While these results suggest the potential for constraining fluxes based on CH_4 retrievals, additional research is required to further explore this possibility.

Finally, the CH_4 sensitivity of imaging spectrometers can be improved dramatically by building an instrument designed exclusively for gas detection. Given the potential utility of such systems, a proposed imaging spectrometer using a 1 nm spectral resolution has been proposed (Aubrey et al. 2015). This imaging spectrometer of the future could be deployed both on helicopters to fly low and slow, improving signal to noise, and on fixed wing aircraft to fly higher and faster, thereby improving areal coverage. The 1 nm spectral resolution will improve detection capabilities down to around 0.28 m^3/h (10 scfh) and false positives will be virtually eliminated by decoupling the spectroscopy of terrestrial surfaces and the atmosphere. This system could offer a method of covering large areas to identify and attribute

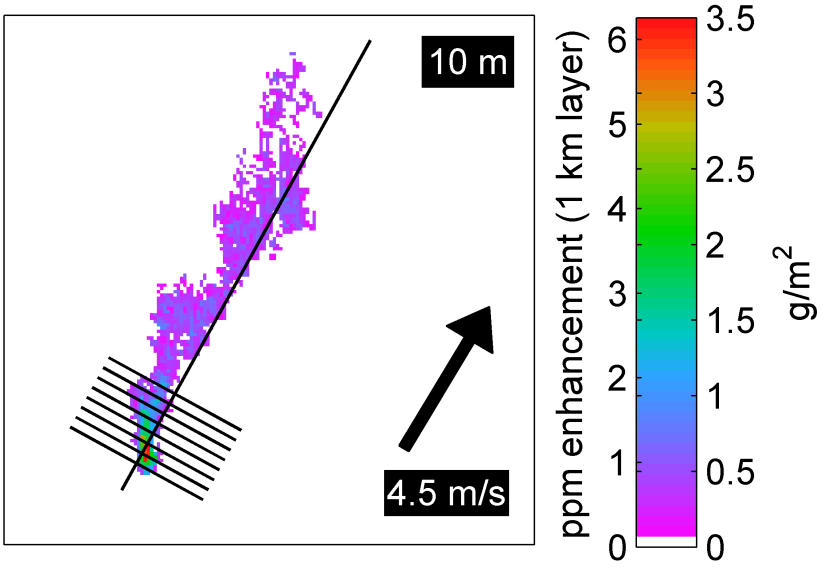

Figure 5.5. AVIRIS-NG retrieval for a 5.08×10^4 g/hour flux (2,500 scfh) showing CH_4 enhancements in g/m^2 and ppm. Wind measured at nearby meteorological station had velocity of 4.5 m/s and 211° direction (black arrow). For each of the eight transects shown (orthogonal to wind) a total mass was calculated across the transect for a unit time, yielding an average of 5.34×10^4 g/hour in good agreement (within 5%) with the metered flux rate.

both super emitters as well as smaller emissions and has great potential for regulatory applications.

Appendix A

Point source emissions mapping using the Airborne Visible/Infrared Imaging Spectrometer (AVIRIS)

A. K. Thorpe[1], D. A. Roberts[1], P. E. Dennison[2], E. S. Bradley[1], C. C. Funk[1,3]

[1]Department of Geography, University of California, Santa Barbara, Santa Barbara, CA

[2]Department of Geography, University of Utah, Salt Lake City, UT

[3]U.S. Geological Survey, Department of Geography, University of California, Santa Barbara, CA

This chapter was published in Proceedings SPIE and is referenced as Thorpe et al. (2012).

A.1 Abstract

The Airborne Visible/Infrared Imaging Spectrometer (AVIRIS) measures reflected solar radiation in the shortwave infrared and has been used to map methane (CH_4) using both a radiative transfer technique (Roberts et al. 2010) and a band ratio method (Bradley et al. 2011). However, these methods are best suited to water bodies with high sunglint and are not well suited for terrestrial scenes. In this study, a Cluster-Tuned Matched Filter (CTMF) algorithm originally developed by Funk et al. (2001) for synthetic thermal infrared data was used for gas plume detection over more heterogeneous backgrounds.

This approach permits mapping of CH_4, CO_2 (carbon dioxide), and N_2O (nitrous oxide) trace gas emissions in multiple AVIRIS scenes for terrestrial and marine targets. At the Coal Oil Point marine seeps offshore of Santa Barbara, CA, strong CH_4 anomalies were detected that closely resemble results obtained using the band ratio index. CO_2 anomalies were mapped for a fossil-fuel power plant, while multiple N_2O and CH_4 anomalies were present at the Hyperion wastewater treatment facility in Los Angeles, CA. Nearby, smaller CH_4 anomalies were also detected immediately downwind of hydrocarbon storage tanks and centered on a flaring stack at the Inglewood Gas Plant.

Improving these detection methods might permit gas detection over large search areas, e.g. identifying fugitive CH_4 emissions from damaged natural gas pipelines or hydraulic fracturing. Further, this technique could be applied to other trace gasses with distinct absorption features and to data from planned instruments such as AVIRIS-NG, the NEON Airborne Observation Platform (AOP), and the visible-shortwave infrared (VSWIR) sensor on the proposed HyspIRI satellite.

A.2 Introduction

Methane (CH_4), carbon dioxide (CO_2), and nitrous oxide (N_2O) are considered the three greenhouse gasses most important to climate change, and global concentrations of these long-lived gasses have increased rapidly since the Industrial Revolution, mainly as a result of human activity. Increasing radiative forcing due to higher concentrations of CH_4, CO_2, and N_2O makes up the majority of the total net increase in radiative forcing since 1750 (IPCC 2007). On a 20 year time scale, one molecule of CH_4 is at least 70 times as effective at trapping radiant energy than a molecule of CO_2, while N_2O has a 20 year global warming potential 289 times greater than CO_2 (IPCC 2007). In addition to being a potent greenhouse gas, CH_4 contributes to ozone (O_3) production and photochemical smog, while N_2O will be the most important contributor to O_3 depletion throughout the 21st century (Ravishankara et al. 2009).

For each of these gasses, the majority of present-day emissions are anthropogenic and often emitted from concentrated point sources. Estimates indicate the majority of pre-industrial CH_4 emissions were from natural sources (Houweling et al. 2000), while between 60 to 70% of CH_4 emissions are presently anthropogenic (Lelieveld et al. 1998) and have an atmospheric residence of 8.4 years (IPCC 2007). Approximately 75% of anthropogenic CO_2 emissions have resulted from burning of fossil fuels and cement production (IPCC 2007) and atmospheric residence varies between 5 and 200 years due to large differences in rates of CO_2 uptake (IPCC 2001). About half of N_2O emissions are presently anthropogenic and emissions remain in the atmosphere on average for 114 years (IPCC 2007).

Existing spaceborne remote sensing provides an effective means of detecting continental scale variation in CH_4, CO_2, and N_2O concentrations using sensors that sample the mid-

infrared (MIR) and thermal-infrared (TIR) (Aires et al. 2002; Beer et al. 2001; Tobin et al. 2006; Saitoh et al. 2009) as well as in the shortwave infrared (SWIR) (Frankenberg et al. 2011). These sensors lack the fine spatial resolution needed to detect near-surface local emissions, including individual plumes from concentrated point sources. Detecting faint gas signatures over heterogeneous surfaces remains challenging, however, one technique of particular promise is matched filters, which have successfully detected gas plumes in simulated data (Villeneuve et al. 1999; Theiler et al. 2006). A matched filter algorithm generates a linear weighting function that produces highest values when an image spectrum matches the shape of the gas target. When applied to a scene, this algorithm reduces noise while enhancing the gas signature and outputs an image indicating those regions with anomalous gas concentrations.

This study aims to improve methods for fine spatial resolution gas detection using a Cluster-Tuned Matched Filter technique originally developed by Funk et al. (2001) for simulated thermal data. The Cluster-Tuned Matched Filter improves performance over traditional matched filter algorithms because it first applies k-means clustering to partition the background surface, then creates a matched filter that is specifically tuned for each cluster. These algorithms were modified for the airborne imaging sensor AVIRIS, which samples 224 contiguous spectral channels between 350 nm and 2,500 nm. To test the feasibility of this approach, the Cluster-Tuned Matched Filter was applied to a diversity of locations known to emit CH_4, CO_2, and N_2O and results were analyzed for consistency with known or probable emission sources.

Developing techniques to map local emissions using airborne imaging spectrometry could permit emission monitoring and hazard detection over large areas. For example, detecting

fugitive CH_4 emissions from leaking natural gas pipelines (Murdock et al. 2008), hydraulic fracturing (Howarth et al. 2011), and coal bed fields is of increasing concern. High resolution mapping of trace gasses from concentrated sources could also improve national greenhouse gas budgets, partitioning between anthropogenic and natural sources, and compliment ongoing global monitoring efforts at coarser spatial resolutions.

A.3 Methodology

A.3.1 AVIRIS data and Modtran radiative transfer model

AVIRIS measures reflected solar radiance over 224 contiguous spectral channels between 350 nm and 2,500 nm, with a spectral sampling interval and nominal Full Width Half Maximum (FWHM) of 10 nm, 34° field of view (FOV), and 1 mrad instantaneous field of view (IFOV) (Green et al. 1998). AVIRIS encoded radiance data are georectified and radiometrically calibrated by the Jet Propulsion Laboratory (JPL). Flown on aircraft, AVIRIS has a high signal-to-noise ratio and a ground-instantaneous field of view (GIFOV) typically ranging between 3 m to 20 m, which offers the potential for detecting gaseous emissions from point sources. This has enabled detection of CH_4 over the Coal Oil Point Seeps offshore of Santa Barbara, CA (Roberts et al. 2010; Bradley et al. 2011), however, these techniques are limited to water bodies with high sunglint and are not well suited for terrestrial scenes.

CH_4, CO_2, and N_2O have absorptions in the SWIR that can be resolved with the 10 nm spectral sampling of AVIRIS. Examples of transmittance spectra are shown in Fig. A.1, calculated using a Modtran 5.3 radiative transfer model parameterized for an AVIRIS flight at 3.8 km altitude for a Los Angeles scene. Absorption features for CH_4 and CO_2 have some spectral overlap with H_2O, however, CH_4 absorptions at 2,300 nm and CO_2 absorptions around

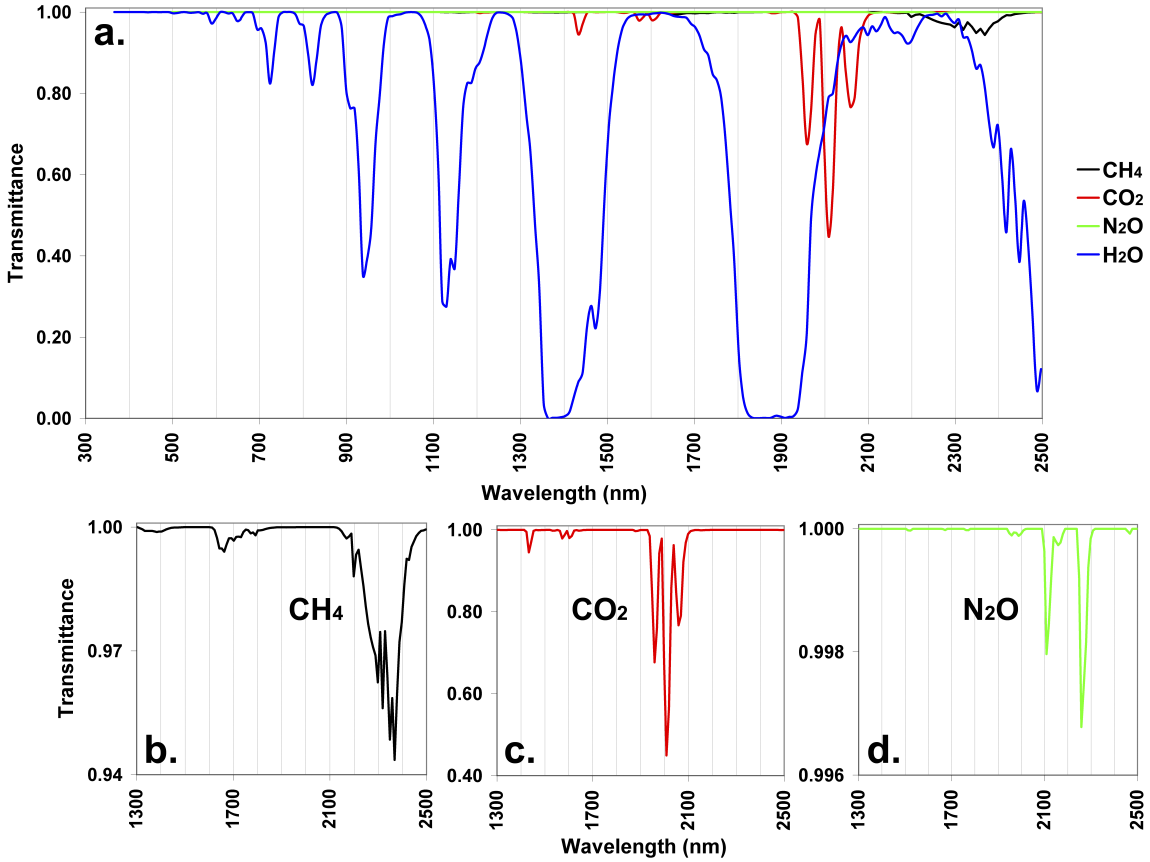

Figure A.1. (a) Transmittance spectra for trace gasses convolved to AVIRIS bands generated using Modtran 5.3, parameterized for a mid-latitude summer model atmosphere and 3.8 km sensor altitude. (b) CH_4 exhibits prominent absorptions between 2,150 nm and 2,450 nm. (c) CO_2 has strong absorptions centered at 1,958 nm, 2,008 nm, and 2,058 nm. (d) N_2O absorptions at 2,109 nm and 2,258 nm are weak compared to those of other trace gases due to low N_2O concentration in the atmosphere.

1,572 nm, 1,602 nm, and 2,058 nm have the least overlap with H_2O absorptions (Fig. A.1a). CH_4, CO_2, and N_2O transmittance spectra were calculated with Modtran parameterized for different flight lines and convolved to AVIRIS wavelengths using the band centers and FWHM supplied by JPL. These transmittance spectra were used as gas targets for the Cluster-Tuned Matched Filter analysis; CH_4, CO_2, and N_2O gas targets for a Los Angeles scene are shown in Fig. A.1b, A.1c, A.1d.

A.3.2 Study sites

To identify AVIRIS images for the Cluster-Tuned Matched Filter analysis, four flight lines containing likely point source emissions of CH_4, CO_2, and N_2O were identified (Fig. A.2). The first scene was acquired over the Coal Oil Point Seeps offshore of Santa Barbara, CA, one of the largest and best studied natural sources of CH_4 emissions and oil with total atmospheric emissions estimated at 100,000 m^3/day (Hornafius et al. 1999). A second AVIRIS flight near Moss Landing, CA imaged a natural gas power generation station with multiple smokestacks, providing an anthropogenic CO_2 emission source. An additional scene covered the Mid-Wilshire district of Los Angeles, known for natural CH_4 and oil seepage, and the Inglewood Oil Field, with active natural gas and hydrocarbon extraction. The final AVIRIS flight line covered the El Segundo neighborhood of Los Angeles and included the Hyperion wastewater treatment facility, a potential source of CH_4 and N_2O emissions.

A.3.3 Cluster-Tuned Matched Filter algorithm

The Cluster-Tuned Matched Filter algorithm first applies k-means clustering to classify the image and partition the background surface (clutter) to minimize within-class variance. To do so, the algorithm uses the first few principle components of the image to assign extreme locations for each of the k-class centroids (Funk et al. 2001). After the k-means algorithm assigns a specified number of classes (defined a priori) and creates a k-means class image, matched filters specifically tuned for each class are applied to the scene using the following equation,

$$\vec{q_j} = \frac{\mathbf{C}_j^{-1}\vec{b}}{\sqrt{\vec{b^T}\mathbf{C}_j^{-1}\vec{b}}} \tag{A.1}$$

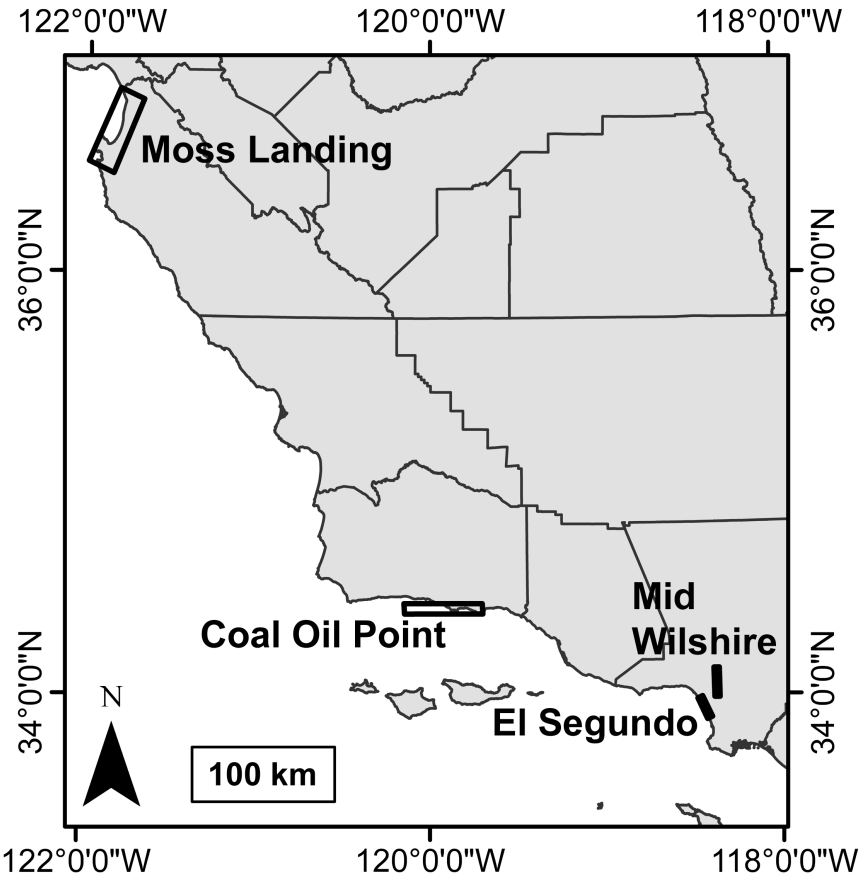

Figure A.2. Extent of four AVIRIS flight lines overlain on map of California showing county boundaries. AVIRIS scenes were acquired near Moss Landing, the Coal Oil Point Seeps offshore of Santa Barbara, and the Mid-Wilshire and El Segundo regions of Los Angeles.

where $\vec{q_j}$ is the Cluster-Tuned Matched Filter for class j, $\mathbf{C}_j^{-1}$ is the inverted covariance matrix for the jth class, and $\vec{b}$ is the gas target spectrum. Multiplication by the inverted covariance matrix in the numerator 'whitens' the data by removing spectral cross-correlation in the background clutter. The denominator standardizes the filtered data so that the expected filtered results have a standard deviation of 1. These filtered pixels are then recomposed as a final output image that reduces noise and sensitivity to surface features while enhancing the gas signature and outputs an image indicating gas anomalies. Cluster-Tuned Matched Filters were applied to each AVIRIS image using transmittance spectra as gas targets, calculated with Modtran parameterized for each flight line.

A.4 Initial results and discussion

Cluster-Tuned Matched Filters were effective for mapping CH_4, CO_2, and N_2O anomalies for concentrated marine and terrestrial emission sources. On 19 June 2008, AVIRIS acquired an image containing the Coal Oil Point marine seeps near Santa Barbara, CA with a spatial resolution of 7.5 m. The scene was characterized by high sunglint and a relatively homogeneous ocean surface, which permitted detection of prominent CH_4 anomalies (Fig. A.3). The anomalies emanate from known seeps, including the Trilogy Seep and IV Super Seep, and are consistent with southwesterly wind measured at the time of image acquisition. These CH_4 anomalies also closely resemble results obtained using the band ratio technique developed by Bradley et al. (2011). Marine seeps are significant but poorly constrained sources of CH_4, releasing an estimated 20 Tg yr^{-1} (Kvenvolden et al. 2005).

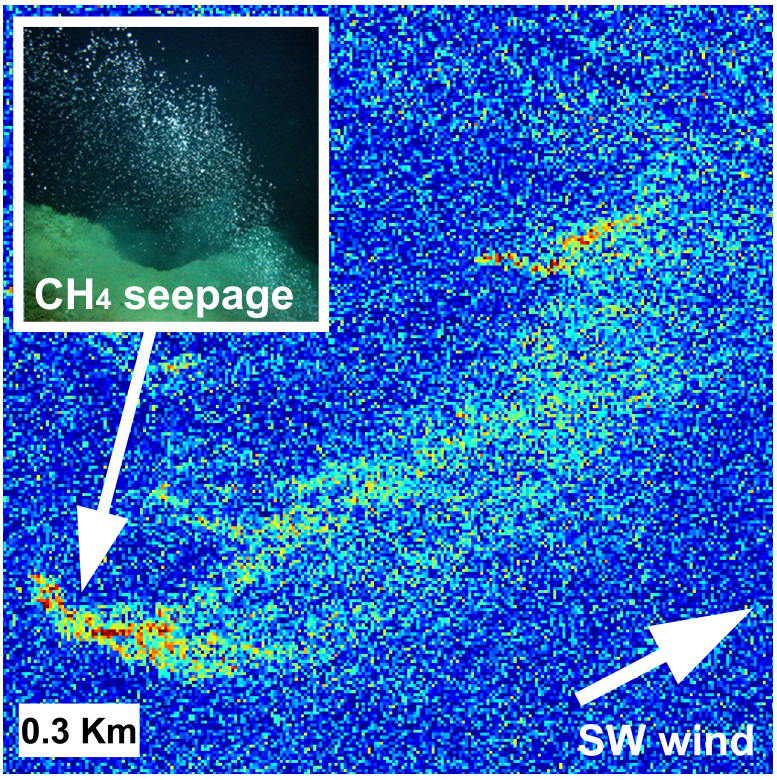

Figure A.3. CH_4 matched filter results for Coal Oil Point seeps.

Analysis of an AVIRIS scene from 19 July 2011 with a spatial resolution of approximately 6 m revealed a prominent CO_2 anomaly for the Moss Landing Power Plant (Fig. A.4), which is powered with natural gas and generated 1,435,507 MT CO_2 in 2010 (EPA 2011a). This anomaly crosses over multiple k-means classes and thus different land cover types and is consistent with a CO_2 plume emitted from four, closely-spaced smokestacks and transported by northwesterly winds. Power plants are a significant emissions source, with 76% of U.S. CO_2 stationary source emissions attributed to electricity production (DOE 2011).

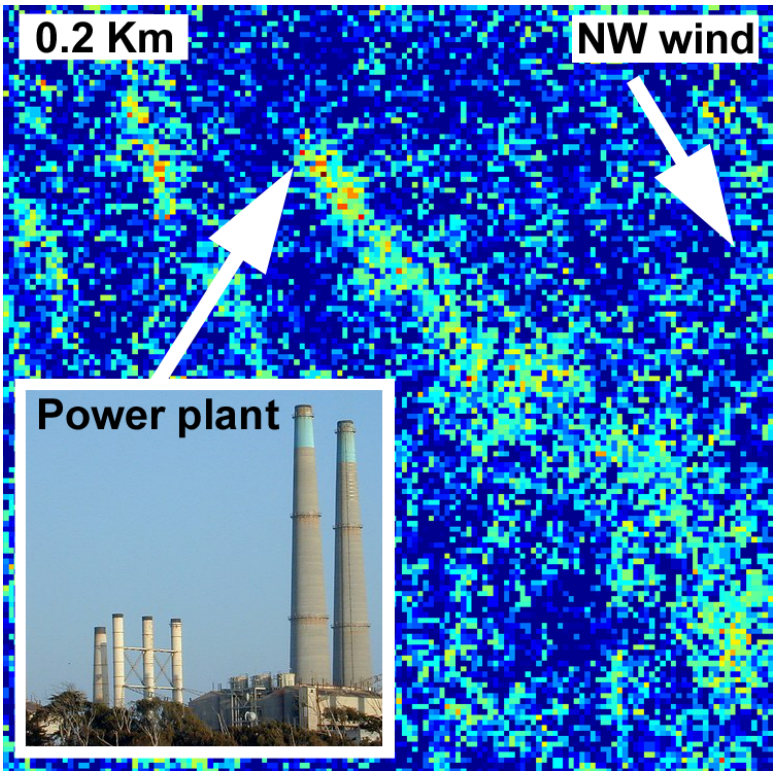

Figure A.4. Cluster-Tuned Matched Filter CO_2 anomalies for the Moss Landing Power Plant.

For an AVIRIS scene covering the El Segundo neighborhood of Los Angeles with a spatial resolution of approximately 3 m (Fig. A.2), multiple N_2O and CH_4 anomalies were present at the Hyperion Sewage Treatment Plant (Fig. A.5). CH_4 anomalies appear throughout the scene (green pixels in Fig. A.5), while N_2O anomalies are observed in close proximity with

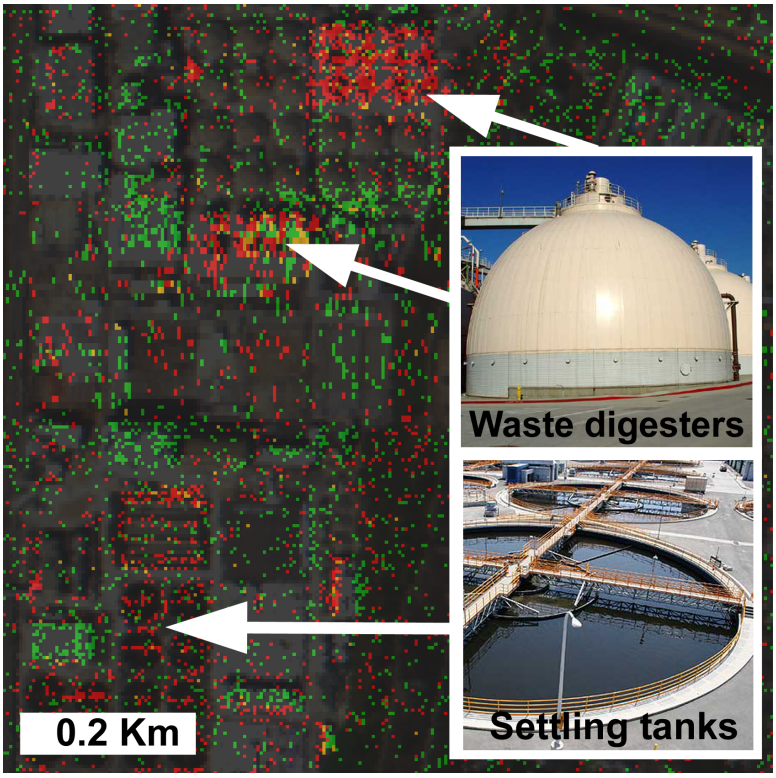

Figure A.5. Matched filter results overlain on a visible band image of the wastewater treatment facility (darkened for presentation). N_2O anomalies (red pixels), appear near two groups of waste digesters. CH_4 anomalies (green pixels) are also present, causing considerable overlap of N_2O and CH_4 anomalies (orange pixels).

egg-shaped digesters and settling tanks (red pixels). Wastewater treatment facilities produce CH_4 and significant N_2O emissions, which result from denitrification and nitrification in both anoxic and anaerobic environments (EPA 2011a; Brown et al. 2010). In 2009, U.S. emissions of CH_4 and N_2O from wastewater treatment were estimated at 24.5 Tg CO_2 Eq. and 5.0 Tg CO_2 Eq. respectively (EPA 2011a).

In the AVIRIS scene covering the Mid-Wilshire region of Los Angeles (Fig. A.2), a CH_4 anomaly was detected at the Inglewood Oil Field that crosses multiple land cover classes and is consistent with local meteorological data indicating a 2.2 m s^{-1} southwesterly wind (Fig. A.6b). The spatial resolution is approximately 3 m for this scene and Google Earth imagery was used to resolve surface features, including what appears to be two hydrocarbon

storage tanks located immediately upwind of the anomaly (Fig. A.6a). Nearby, an additional CH_4 anomaly was identified centered on a flaring stack at the Inglewood Gas Plant (Fig. A.6c and A.6d) and sensor saturation in the SWIR indicated active flaring at the time of image acquisition. Fugitive CH_4 emissions associated with hydrocarbon production are considerable, estimated in 2009 at 221.2 Tg CO_2 Eq. for natural gas systems, 71.0 Tg CO_2 Eq. for coal mining, and 30.9 Tg CO_2 Eq. for petroleum systems (EPA 2011a).

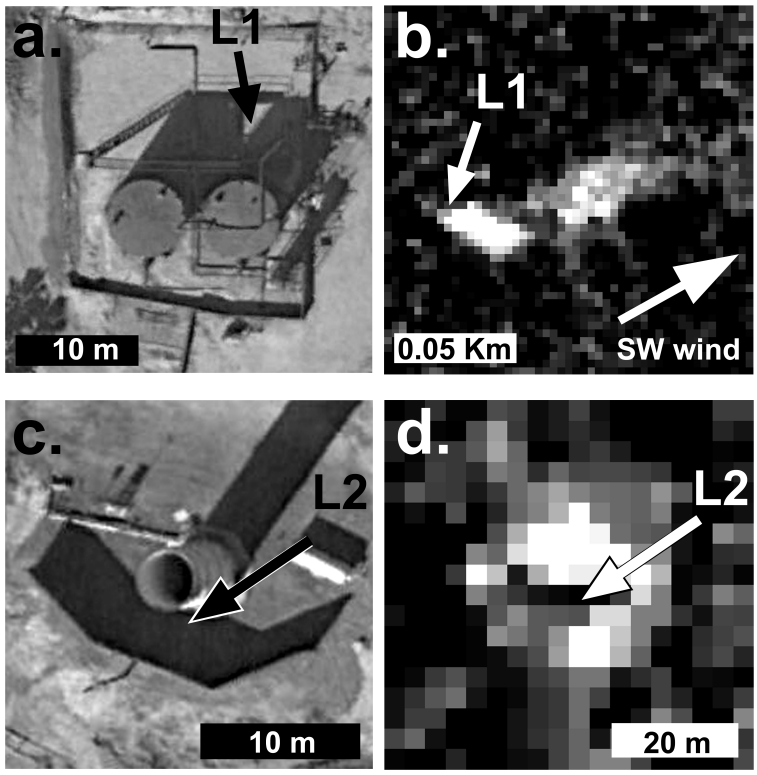

Figure A.6. (a) Close-up of hydrocarbon storage tanks (Location L1) (Google Earth 2012). (b) CH_4 anomaly downwind of L1, shown using median smoothing filter. (c) Close-up flaring stack (Location L2) (Google Earth 2012). (d) CH_4 anomaly centered on stack at L2, shown using median smoothing filter.

Despite these promising results, 'speckle' and false positives observed in matched filter results make interpretation of anomalies challenging. False positives result for surfaces with strong absorptions located at the same wavelengths as gas absorption features; for example, the CH_4 Cluster-Tuned Matched Filter produced false positives for roofs with limestone peb-

bles that exhibit strong carbonate (CO_3) absorption at 2,338 nm. Therefore, to distinguish trace gas emissions from false positives, methods of smoothing results and suppressing false positives must be developed.

While Cluster-Tuned Matched Filters are well suited for detecting anomalies, they do not provide concentrations necessary to calculate fluxes or generate maps of gas concentrations. In order to create robust techniques for detection and quantification of trace gas emissions in AVIRIS data, additional research is required. A sensitivity analysis using synthetic images and radiative transfer simulations is necessary to determine minimum detectable gas concentrations by the Cluster-Tuned Matched Filter approach and determine how surface composition and albedo influence matched filter scores. Multiple approaches will be used to estimate concentrations, including Modtran 5.3 radiative transfer simulations to generate synthetic spectra with elevated gas concentrations that will be best fit to AVIRIS radiance data as well as additional residual based techniques. Evaluating the accuracy of these concentrations is an important prerequisite for creating maps of gas concentrations and estimating fluxes from individual point sources to better constrain regional emissions.

A.5 Conclusions

The Cluster-Tuned Matched Filter technique is effective for mapping CH_4, CO_2, and N_2O anomalies for concentrated natural and anthropogenic emission sources in AVIRIS imagery, including the Coal Oil Point marine seeps (CH_4), the Moss Landing Power Plant (CO_2), and the Hyperion Sewage Treatment Plant (N_2O and CH_4). These long-lived trace gasses are often emitted at concentrated sources; an estimated 4,507 stationary point sources produced 63% of U.S. CO_2 emissions from fossil fuel combustion in 2008 (DOE 2011). Therefore, targeting

reductions in anthropogenic CH_4, CO_2, and N_2O emissions from concentrated sources is a particularly efficient means of mitigating their effects.

Airborne imaging spectrometers are well suited for monitoring local sources because they provide areal coverage with high spatial resolution necessary to resolve point source emissions. Developing gas detection techniques for airborne platforms could better constrain local emissions as well as improve national greenhouse gas budgets and partitioning between anthropogenic and natural sources. To create robust techniques for mapping trace gas emissions in AVIRIS data, additional research is required to determine minimum detectable gas concentrations by the Cluster-Tuned Matched Filter, reduce false positives, and develop techniques for estimating gas concentrations.

Given these promising preliminary results, the Cluster-Tuned Matched Filter might be capable of detecting additional trace gasses with distinct absorption features and could be applied to data from planned AVIRIS-like instruments such as AVIRIS-NG, the NEON Airborne Observation Platform (AOP), and the proposed HyspIRI VSWIR sensor. The addition of these planned sensors could greatly improve mapping of local and regional emissions by providing the spatial coverage necessary to detect individual emission sources and potential for repeat temporal coverage to monitor global change.

References

Aires, F., Chedd, A., Scott, N.A., and Rossow, W.B. (2002). A regularized neural net approach for retrieval of atmospheric and surface temperatures with the IASI instrument. *Journal of Applied Meteorology, 41*, 144-159.

Allen, D.T., Pacsi, A.P., Sullivan, D.W., Zavala-Araiza, D., Harrison, M., Keen, K., Fraser, M.P., Daniel Hill, A., Sawyer, R.F., and Seinfeld, J.H. (2015). Methane emissions from process equipment at natural gas production sites in the United States: Pneumatic controllers. *Environmental Science & Technology, 49*, 633-640.

Allen, D.T., Sullivan, D.W., Zavala-Araiza, D., Pacsi, A.P., Harrison, M., Keen, K., Fraser, M.P., Daniel Hill, A., Lamb, B.K., Sawyer, R.F., and Seinfeld, J.H. (2015). Methane emissions from process equipment at natural gas production sites in the United States: Liquid unloadings. *Environmental Science & Technology, 49*, 641-648.

Allen, D.T., Torres, V.M., Thomas, J., Sullivan, D.W., Harrison, M., Hendler, A., Herndon, S.C., Kolb, C.E., Fraser, A., Hill, D., Lamb, B.K., Miskimins, J., Sawyer, R.F., and Seinfeld, J.H. (2013). Measurements of methane emissions at natural gas production sites in the United States. *Proceedings of the National Academy of Sciences of the United States of America, 110*, 17768-17773.

Alvarez, R.A., Pacala, S.W., Winebrake, J.J., Chameides, W.L., and Hamburg, S.P. (2012). Greater focus needed on methane leakage from natural gas infrastructure. *Proceedings of the National Academy of Sciences of the United States of America, 109*, 6435-6440.

ARCTAS (2010). Arctic Research of the Composition of the Troposphere from Aircraft and

Satellites, National Aeronautics and Space Administration. Retrieved 2 March 2015, from http://www-air.larc.nasa.gov/missions/arctas/arctas.html

Asner, G.P., Knapp, D.E., Boardman, J., Green, R.O., Kennedy-Bowdoin, T., Eastwood, M., Martin, R.E., Anderson, C., and Field, C.B. (2012). *Carnegie Airborne Observatory-2: Increasing science data dimensionality via high-fidelity multi-sensor fusion. Remote Sensing of Environment, 124*, 454-465.

Aubrey, A.D., Frankenberg, C., Green, R.O., Eastwood, M.L., Thompson, D.R., and Thorpe, A. K. (2015). Crosscutting airborne remote sensing technologies for oil and gas and earth science applications, paper presented at Offshore Technology Conference, Houston, Texas.

Beer, R., Glavich, T.A., and Rider, D.M. (2001). *Tropospheric emission spectrometer for the Earth Observing System's Aura Satellite. Applied Optics, 40*, 2356-2367.

Bergamaschi, P., Krol, M., Meirink, J.F., Dentener, F., Segers, A., van Aardenne, J., Monni, S., Vermeulen, A.T., Schmidt, M., Ramonet, M., Yver, C., Meinhardt, F., Nisbet, E.G., Fisher, R.E., O'Doherty, S., and Dlugokencky, E.J. (2010). *Inverse modeling of European CH_4 emissions 2001-2006. Journal of Geophysical Research-Atmospheres, 115*, D22309.

Berk, A., Bernstein, L.S., and Robertson, D.C. (1989). MODTRAN: A moderate resolution model for LOWTRAN7, AFGL-TR-89-0122, paper presented at SPIE proceedings on optical spectroscopic techniques and instrumentation for atmospheric and space research III.

Boles, J.R., Clark, J.F., Leifer, I., and Washburn, L. (2001). Temporal variation in natural methane seep rate due to tides, Coal Oil Point area, California. *Journal of Geophysical*

Research-Oceans, 106, 27077-27086.

Bousquet, P., Ciais, P., Miller, J.B., Dlugokencky, E.J., Hauglustaine, D.A., Prigent, C., Van der Werf, G.R., Peylin, P., Brunke, E.G., Carouge, C., Langenfelds, R.L., Lathiere, J., Papa, F., Ramonet, M., Schmidt, M., Steele, L.P., Tyler, S.C., and White, J. (2006). *Contribution of anthropogenic and natural sources to atmospheric methane variability. Nature, 443*, 439-443.

Bovensmann, H., Doicu, A., Stammes, P., Van Roozendael, M., von Savigny, C., Penning de Vries, M., Beirle, S., Wagner, T., Chance, K., Buchwitz, M., Kokhanovsky, A., Richter, A., Rozanov, A.V., and Rozanov, V.V. (2011). *SCIAMACHY - Exploring the changing EarthâĂŹs atmosphere*, Springer, Dordrecht.

Bovensmann, H., Buchwitz, M., Burrows, J.P., Reuter, M., Krings, T., Gerilowski, K., Schneising, O., Heymann, J., Tretner, A., and Erzinger, J. (2010). A remote sensing technique for global monitoring of power plant CO_2 emissions from space and related applications. *Atmospheric Measurement Techniques, 3*, 781-811.

Bradley, E.S., Leifer, I., Roberts, D.A., Dennison, P.E., and Washburn, L. (2011). Detection of marine methane emissions with AVIRIS band ratios. *Geophysical Research Letters, 38*, L10702.

Brandt, A.R., Heath, G.A., Kort, E.A., O'Sullivan, F., Petron, G., Jordaan, S.M., Tans, P., Wilcox, J., Gopstein, A.M., Arent, D., Wofsy, S., Brown, N.J., Bradley, R., Stucky, G.D., Eardley, D., and Harriss, R. (2014). Methane leaks from North American natural gas systems. *Science, 343*, 733-735.

Brown, S., Beecher, N., and Carpenter, A. (2010). Calculator tool for determining greenhouse gas emissions for biosolids processing and end use. *Environmental Science & Technology, 44*, 9509-9515.

Buchwitz, M., de Beek, R., Burrows, J.P., Bovensmann, H., Warneke, T., Notholt, J., Meirink, J.F., Goede, A.P.H., Bergamaschi, P., Korner, S., Heimann, M., and Schulz, A. (2005a). Atmospheric methane and carbon dioxide from SCIAMACHY satellite data: initial comparison with chemistry and transport models. *Atmospheric Chemistry and Physics, 5*, 941-962.

Buchwitz, M., de Beek, R., Noel, S., Burrows, J.P., Bovensmann, H., Bremer, H., Bergamaschi, P., Korner, S., and Heimann, M. (2005b). Carbon monoxide, methane and carbon dioxide columns retrieved from SCIAMACHY by WFM-DOAS: Year 2003 initial data set. *Atmospheric Chemistry and Physics, 5*, 3313-3329.

Buchwitz, M., and Burrows, J.P. (2003). Retrieval of CH_4, CO, and CO_2 total column amounts from SCIAMACHY near-infrared nadir spectra: retrieval algorithm and first results. *Proc. SPIE, 5235*, 375-388.

Buchwitz, M., Rozanov, V.V., and Burrows, J.P. (2000). A near-infrared optimized DOAS method for the fast global retrieval of atmospheric CH_4, CO, CO_2, H_2O, and N_2O total column amounts from SCIAMACHY Envisat-1 nadir radiances. *Journal of Geophysical Research-Atmospheres, 105*, 15231-15245.

Butler, J. (2012). National Oceanic and Atmospheric Administration, *The NOAA annual greenhouse gas index (AGGI).* Retrieved 2 March 2015, from http://www.esrl.noaa.gov/gmd/aggi

Butz, A., Guerlet, S., Hasekamp, O., Schepers, D., Galli, A., Aben, I., Frankenberg, C., Hart-

mann, J.M., Tran, H., Kuze, A., Keppel-Aleks, G., Toon, G., Wunch, D., Wennberg, P., Deutscher, N., Griffith, D., Macatangay, R., Messerschmidt, J., Notholt, J., and Warneke, T. (2011). Toward accurate CO_2 and CH_4 observations from GOSAT. *Geophysical Research Letters, 38*, L14812.

Cambaliza, M.O., Shepson, P.B., Caulton, D., Stirm, B., Samarov, D., Gurney, K.R., Turnbull, J., Davis, K.J., Possolo, A., Karion, A., Sweeney, C., Moser, B., Hendricks, A., Lauvaux, T., Mays, K., Whetstone, J., Huang, J., Razlivanov, I., Miles, N.L., and Richardson, S.J. (2013). Assessment of uncertainties of an aircraft-based mass-balance approach for quantifying urban greenhouse gas emissions. *Atmospheric Chemistry and Physics Discussions, 13*, 29895-29945.

Caulton, D.R., Shepson, P.B., Santoro, R.L., Sparks, J.P., Howarth, R.W., Ingraffea, A.R., Cambaliza, M.O.L., Sweeney, C., Karion, A., Davis, K.J., Stirm, B.H., Montzka, S.A., and Miller, B.R. (2014). Toward a better understanding and quantification of methane emissions from shale gas development. *Proceedings of the National Academy of Sciences, 111*, 6237-6242.

Chilingar, G.V., and Endres, B. (2005). Environmental hazards posed by the Los Angeles Basin urban oilfields: An historical perspective of lessons learned. *Environmental Geology, 47*, 302-317.

Christensen, L.E, et al. (2015). Open-Path Laser Spectrometer (OPLS) methane detector for hand-held applications, Manuscript in preparation.

Ciais, P., Sabine, C., Bala, G., Bopp, L., Brovkin, V., Canadell, J., Chhabra, A., DeFries, R., Galloway, J., Heimann, M., Jones, C., Le Quere, C., Myneni, R.B., Piao, S., and Thornton, P.

(2013). Carbon and other biogeochemical cycles. In: *Climate change 2013: The physical science basis. Contribution of working group I to the fifth assessment report of the Intergovernmental Panel on Climate Change*, Cambridge University Press, Cambridge and New York.

Clark, J.F., Washburn, L., and Emery, K.S. (2010). Variability of gas composition and flux intensity in natural marine hydrocarbon seeps. *Geo-Marine Letters, 30*, 379-388.

Clark, R., Swayze, G., Livo, E., Kokaly, R., King, T.V.V., Dalton, B., Vance, S., Rockwell, B., Hoefen, T., and McDougal, R. (2002). *Surface reflectance calibration of terrestrial imaging spectroscopy data: A tutorial using AVIRIS*, Proceedings of the 11th JPL airborne earth science workshop, Jet Propulsion Laboratory Publications, Pasadena.

Cliff, A. D., and Ord J. K. (1981). *Spatial processes, models and applications*, Pion, London.

Dennison, P.E., Thorpe, A.K., Pardyjak, E.R., Roberts, D.A., Qi, Y., Green, R.O., Bradley, E.S., and Funk, C.C. (2013). High spatial resolution mapping of elevated atmospheric carbon dioxide using airborne imaging spectroscopy: Radiative transfer modeling and power plant plume detection. *Remote Sensing of Environment, 139*, 116-129.

Dennison, P.E., and Roberts, D.A. (2003). Endmember selection for multiple endmember spectral mixture analysis using endmember average RMSE. *Remote Sensing of Environment, 87*, 123-135.

Dlugokencky, E.J., Nisbet, E.G., Fisher, R., and Lowry, D. (2011). Global atmospheric methane: Budget, changes and dangers. *Philosophical Transactions of the Royal Society a-Mathematical Physical and Engineering Sciences, 369*, 2058-2072.

Dlugokencky, E.J., Bruhwiler, L., White, J.W.C., Emmons, L.K., Novelli, P.C., Montzka, S.A., Masarie, K.A., Lang, P.M., Crotwell, A.M., Miller, J.B., and Gatti, L.V. (2009). Observational constraints on recent increases in the atmospheric CH_4 burden. *Geophysical Research Letters, 36*, L18803.

DOE (2011). U.S. Department of Energy, *CO_2 stationary sources*, National Energy Technology Laboratory (NETL). Retrieved 2 March 2015, from http://www.netl.doe.gov/technologies/carbon$_s eq/natcarb/stationary.html$

DOGGR (2010a). State of California Department of Conservation, *Division of oil, gas and geothermal resources, GIS and well data downloads*, Retrieved 2 March 2015, from http://www.consrv.ca.gov/dog/maps/Pages/goto$_w elllocation.aspx$

DOGGR (2010b). State of California Department of Conservation, *Online production and injection query*, Retrieved 2 March 2015, from http://opi.consrv.ca.gov/opi/opi.dll

Dufour, E., and Breon, F.M. (2003). Spaceborne estimate of atmospheric CO_2 column by use of the differential absorption method: error analysis. *Applied Optics, 42*, 3595-3609.

EIA (2013), U.S. Energy Information Administration, *Annual energy outlook 2013 with projections to 2040*, Washington, D.C.

EPA (2014), U.S. Environmental Protection Agency, U.S. EPA Office of Air Quality Planning and Standards (OAQPS), *Report for oil and natural gas sector leaks, Oil and natural gas sector leaks*, Washington, D.C.

EPA (2013), U.S. Environmental Protection Agency, *Inventory of U.S. greenhouse gas emissions and sinks: 1990-2011, Technical report EPA 430-R-13-001*, Washington, D.C.

EPA (2011a). U.S. Environmental Protection Agency, *Greenhouse gas (GHG) emissions from large facilities.* Retrieved 2 March 2015, from http://ghgdata.epa.gov/ghgp/main.do

EPA (2011b), U.S. Environmental Protection Agency, *Inventory of U.S. greenhouse gas emissions and sinks: 1990-2019*, Washington, D.C.

EPA (2010). U.S. Environmental Protection Agency, *Producers technology transfer workshop: Reducing methane emission with vapor recovery on storage tanks, Lessons learned from the Natural Gas STAR Program*, Washington, D.C.

EPA (2006a). U.S. Environmental Protection Agency, *Global anthropogenic non- CO_2 greenhouse gas emissions: 1990-2020*, Washington, D.C.

EPA (2006b). U.S. Environmental Protection Agency, *Technical report, EPA Phase II aggregate site report, Cost-effective directed inspection and maintenance control opportunities at five gas processing plants and upstream gathering compressor stations and well sites*, Washington, D.C.

Etheridge, D.M., Steele, L.P., Francey, R.J., and Langenfelds, R.L. (1998). Atmospheric methane between 1000 AD and present: Evidence of anthropogenic emissions and climatic variability. *Journal of Geophysical Research-Atmospheres, 103*, 15979-15993.

Etiope, G., Feyzullayev, A., and Baciu, C.L. (2009). Terrestrial methane seeps and mud volcanoes: A global perspective of gas origin. *Marine and Petroleum Geology, 26*, 333-344.

Eugster, W., and Pluss, P. (2010). A fault-tolerant eddy covariance system for measuring CH_4 fluxes. *Agricultural and Forest Meteorology, 150*, 841-851.

Farrell, P., Culling, D., and Leifer, I. (2013). Transcontinental methane measurements: Part

1. A mobile surface platform for source investigations. *Atmospheric Environment, 74*, 422-431.

Frankenberg, C., Aben, I., Bergamaschi, P., Dlugokencky, E.J., van Hees, R., Houweling, S., van der Meer, P., Snel, R., and Tol, P. (2011). Global column-averaged methane mixing ratios from 2003 to 2009 as derived from SCIAMACHY: Trends and variability. *Journal of Geophysical Research-Atmospheres, 116*, D04302.

Frankenberg, C., Meirink, J.F., van Weele, M., Platt, U., and Wagner, T. (2005a). Assessing methane emissions from global space-borne observations. *Science, 308*, 1010-1014.

Frankenberg, C., Platt, U., and Wagner, T. (2005b). Iterative maximum a posteriori (IMAP)-DOAS for retrieval of strongly absorbing trace gases: Model studies for CH_4 and CO_2 retrieval from near infrared spectra of SCIAMACHY onboard ENVISAT. *Atmospheric Chemistry and Physics, 5*, 9-22.

Frankenberg, C., Platt, U., and Wagner, T. (2005c). Retrieval of CO from SCIAMACHY onboard ENVISAT: Detection of strongly polluted areas and seasonal patterns in global CO abundances. *Atmospheric Chemistry and Physics, 5*, 1639-1644.

Fu, D., Pongetti, T.J., Blavier, J.-F.L., Crawford, T.J., Manatt, K.S., Toon, G.C., Wong, K.W., and Sander, S.P. (2014). Near-infrared remote sensing of Los Angeles trace gas distributions from a mountaintop site. *Atmospheric Measurement Techniques, 7*, 713-729.

Funk, C.C., Theiler, J., Roberts, D.A., and Borel, C.C. (2001). Clustering to improve matched filter detection of weak gas plumes in hyperspectral thermal imagery. *IEEE Transactions on Geoscience and Remote Sensing, 39*, 1410-1420.

GAO (2010). United States Government Accountability Office, *Federal oil and gas leases: Opportunities exist to capture vented and flared natural gas, which would increase royalty payments and reduce greenhouse gases, GAO-11-34*, Washington, D.C.

Gerilowski, K., Tretner, A., Krings, T., Buchwitz, M., Bertagnolio, P.P., Belemezov, F., Erzinger, J., Burrows, J.P., and Bovensmann, H. (2011). MAMAP - A new spectrometer system for column-averaged methane and carbon dioxide observations from aircraft: instrument description and performance analysis. *Atmospheric Measurement Techniques, 4*, 215-243.

Green, R.O., Eastwood, M.L., Sarture, C.M., Chrien, T.G., Aronsson, M., Chippendale, B.J., Faust, J.A., Pavri, B.E., Chovit, C.J., Solis, M.S., Olah, M.R., and Williams, O. (1998). Imaging spectroscopy and the Airborne Visible Infrared Imaging Spectrometer (AVIRIS). *Remote Sensing of Environment, 65*, 227-248.

Guanter, L., Frankenberg, C., Dudhia, A., Lewis, P.E., Gomez-Dans, J., Kuze, A., Suto, H., and Grainger, R.G. (2012). Retrieval and global assessment of terrestrial chlorophyll fluorescence from GOSAT space measurements. *Remote Sensing of Environment, 121*, 236-251.

Gurevich, A.E., Endres, B.L., Robertson, J.O., and Chilingar, G.V. (1993). Gas migration from oil and gas fields and associated hazards. *Journal of Petroleum Science and Engineering, 9*, 223-238.

Hamlin, L., Green, R.O., Mouroulis, P., Eastwood, M., Wilson, D., Dudik, M., and Paine, C. (2011). Imaging spectrometer science measurements for terrestrial ecology: AVIRIS and new developments, paper presented at Aerospace Conference, 2011 IEEE, 1-7.

Herold, M., Roberts, D.A., Gardner, M.E., and Dennison, P.E. (2004). Spectrometry for urban

area remote sensing - Development and analysis of a spectral library from 350 to 2400 nm. *Remote Sensing of Environment, 91*, 304-319.

Hornafius, J.S., Quigley, D., and Luyendyk, B.P. (1999). The world's most spectacular marine hydrocarbon seeps (Coal Oil Point, Santa Barbara Channel, California): Quantification of emissions. *Journal of Geophysical Research-Oceans, 104*, 20703-20711.

Houweling, S., Dentener, F., and Lelieveld, J. (2000). Simulation of preindustrial atmospheric methane to constrain the global source strength of natural wetlands. *Journal of Geophysical Research-Atmospheres, 105*, 17243-17255.

Howarth, R.W., Santoro, R., and Ingraffea, A. (2011). Methane and the greenhouse-gas footprint of natural gas from shale formations. *Climatic Change, 106*, 679-690.

Hsu, Y.K., VanCuren, T., Park, S., Jakober, C., Herner, J., FitzGibbon, M., Blake, D.R., and Parrish, D.D. (2010). Methane emissions inventory verification in Southern California. *Atmospheric Environment, 44*, 1-7.

Hulley, G. (2015). High spatial resolution imaging of trace gas sources with the airborne Hyperspectral Thermal Emission Spectrometer (HyTES). *Remote Sensing of Environment*, Manuscript in preparation.

Hurley, J., Dudhia, A., and Grainger, R.G. (2009). Cloud detection for MIPAS using singular vector decomposition. *Atmospheric Measurement Techniques, 2*, 533-547.

IPCC (2013). Intergovernmental Panel on Climate Change, *Climate change 2013: The physical science basis. Contribution of working group I to the fifth assessment report of the intergovernmental panel on climate change*, Cambridge University Press, Cambridge and New

York.

IPCC (2007). Intergovernmental Panel on Climate Change, *Climate change 2007: The physical science basis. Contribution of working group I to the fourth assessment report of the Intergovernmental Panel on Climate Change*, Cambridge University Press, Cambridge and New York.

IPCC (2001). Intergovernmental Panel on Climate Change, *Climate change 2001: The scientific basis. Contribution of working group I to the third assessment report of the Intergovernmental Panel on Climate Change*, Cambridge University Press, Cambridge and New York.

IPCC (2000). Intergovernmental Panel on Climate Change, *Good practice guidance and uncertainty management in national greenhouse gas inventories*, Cambridge University Press, Cambridge and New York.

Johnson, W.R., Hook, S.J., Mouroulis, P., Wilson, D.W., Gunapala, S.D., Realmuto, V., Lamborn, A., Paine, C., Mumolo, J.M., and Eng, B.T. (2011). HyTES: Thermal imaging spectrometer development, paper presented at Aerospace Conference, 2011 IEEE, 1-8.

JPL (2014). Jet Propulsion Laboratory, Megacities Carbon Project. Retrieved 2 March 2015, from http://megacities.jpl.nasa.gov/portal/

Kalnay, E., Kanamitsu, M., Kistler, R., Collins, W., Deaven, D., Gandin, L., Iredell, M., Saha, S., White, G., Woollen, J., Zhu, Y., Chelliah, M., Ebisuzaki, W., Higgins, W., Janowiak, J., Mo, K.C., Ropelewski, C., Wang, J., Leetmaa, A., Reynolds, R., Jenne, R., and Joseph, D. (1996). The NCEP/NCAR 40-year reanalysis project. *Bulletin of the American Meteorological Society, 77*, 437-471.

Kampe, T.U., Johnson, B.R., Kuester, M., and Keller, M. (2010). NEON: the first continental-scale ecological observatory with airborne remote sensing of vegetation canopy biochemistry and structure. *Journal of Applied Remote Sensing, 4*, 043510.

Karion, A., Sweeney, C., Petron, G., Frost, G., Hardesty, R.M., Kofler, J., Miller, B.R., Newberger, T., Wolter, S., Banta, R., Brewer, A., Dlugokencky, E., Lang, P., Montzka, S.A., Schnell, R., Tans, P., Trainer, M., Zamora, R., and Conley, S. (2013). Methane emissions estimate from airborne measurements over a western United States natural gas field. *Geophysical Research Letters, 40*, 4393-4397.

Kirschke, S., Bousquet, P., Ciais, P., Saunois, M., Canadell, J.G., Dlugokencky, E.J., Bergamaschi, P., Bergmann, D., Blake, D.R., Bruhwiler, L., Cameron-Smith, P., Castaldi, S., Chevallier, F., Feng, L., Fraser, A., Heimann, M., Hodson, E.L., Houweling, S., Josse, B., Fraser, P.J., Krummel, P.B., Lamarque, J.F., Langenfelds, R.L., Le Quere, C., Naik, V., O'Doherty, S., Palmer, P.I., Pison, I., Plummer, D., Poulter, B., Prinn, R.G., Rigby, M., Ringeval, B., Santini, M., Schmidt, M., Shindell, D.T., Simpson, I.J., Spahni, R., Steele, L.P., Strode, S.A., Sudo, K., Szopa, S., van der Werf, G.R., Voulgarakis, A., van Weele, M., Weiss, R.F., Williams, J.E., and Zeng, G. (2013). Three decades of global methane sources and sinks. *Nature Geoscience, 6*, 813-823.

Kluser, L., Martynenko, D., and Holzer-Popp, T. (2011). Thermal infrared remote sensing of mineral dust over land and ocean: a spectral SVD based retrieval approach for IASI. *Atmospheric Measurement Techniques, 4*, 757-773.

Kneizys, F.X., Abreu, L.W., Anderson, G.P., Chetwynd, J.H., Shettle, E.P., Robertson, D.C., Acharya, P., Rothman, L., Selby, J.E.A., Gallery, W.O., and Clough, S.A. (1996). *The MOD-*

TRAN 2/3 report and LOWTRAN 7 model, Tech. rep., Hanscom AFB.

Kort, E.A., Frankenberg, C., Costigan, K.R., Lindenmaier, R., Dubey, M.K., and Wunch, D. (2014). Four Corners: the largest US methane anomaly viewed from space. *Geophysical Research Letters, 41*, 6898-6903.

Kort, E.A., Eluszkiewicz, J., Stephens, B.B., Miller, J.B., Gerbig, C., Nehrkorn, T., Daube, B.C., Kaplan, J.O., Houweling, S., and Wofsy, S.C. (2008). Emissions of CH_4 and N_2O over the United States and Canada based on a receptor-oriented modeling framework and COBRA-NA atmospheric observations. *Geophysical Research Letters, 35*, L18808.

Krings, T., Gerilowski, K., Buchwitz, M., Hartmann, J., Sachs, T., Erzinger, J., Burrows, J.P., and Bovensmann, H. (2013). Quantification of methane emission rates from coal mine ventilation shafts using airborne remote sensing data. *Atmospheric Measurement Techniques, 6*, 151-166.

Krings, T., Gerilowski, K., Buchwitz, M., Reuter, M., Tretner, A., Erzinger, J., Heinze, D., Pfluger, U., Burrows, J.P., and Bovensmann, H. (2011). MAMAP - a new spectrometer system for column-averaged methane and carbon dioxide observations from aircraft: retrieval algorithm and first inversions for point source emission rates. *Atmospheric Measurement Techniques, 4*, 1735-1758.

Kvenvolden, K.A., and Rogers, B.W. (2005). Gaia's breath - Global methane exhalations. *Marine and Petroleum Geology, 22*, 579-590.

Kvenvolden, K.A. (1988). Methane Hydrate - A major reservoir of carbon in the shallow geosphere. *Chemical Geology, 71*, 41-51.

Lamb, B.K., Mcmanus, J.B., Shorter, J.H., Kolb, C.E., Mosher, B., Harriss, R.C., Allwine, E., Blaha, D., Howard, T., Guenther, A., Lott, R.A., Siverson, R., Westberg, H., and Zimmerman, P. (1995). Development of atmospheric tracer methods to measure methane emissions from natural-gas facilities and urban areas. *Environmental Science & Technology, 29*, 1468-1479.

Leifer, I., Culling, D., Schneising, O., Farrell, P., Buchwitz, M., and Burrows, J.P. (2013). Transcontinental methane measurements: Part 2. Mobile surface investigation of fossil fuel industrial fugitive emissions. *Atmospheric Environment, 74*, 432-441.

Leifer, I., Kamerling, M.J., Luyendyk, B.P., and Wilson, D.S. (2010). Geologic control of natural marine hydrocarbon seep emissions, Coal Oil Point seep field, California. *Geo-Marine Letters, 30*, 331-338.

Leifer, I., Luyendyk, B.P., Boles, J., and Clark, J.F. (2006a). Natural marine seepage blowout: Contribution to atmospheric methane. *Global Biogeochemical Cycles, 20*, GB3008.

Leifer, I., Roberts, D., Margolis, J., and Kinnaman, F. (2006b). In situ sensing of methane emissions from natural marine hydrocarbon seeps: A potential remote sensing technology. *Earth and Planetary Science Letters, 245*, 509-522.

Lelieveld, J., Crutzen, P.J., and Dentener, F.J. (1998). Changing concentration, lifetime and climate forcing of atmospheric methane. *Tellus Series B-Chemical and Physical Meteorology, 50*, 128-150.

Lelieveld, J., Crutzen, P.J., and Bruhl, C. (1993). Climate effects of atmospheric methane. *Chemosphere, 26*, 739-768.

Miller, C.E., and Dinardo, S.J. (2012). CARVE: The Carbon in Arctic Reservoirs Vulnerability Experiment, paper presented at Aerospace Conference, 2012 IEEE, 1-17.

Miller, S.M., Wofsy, S.C., Michalak, A.M., Kort, E.A., Andrews, A.E., Biraud, S.C., Dlugockenky, E.J., Eluszkiewicz, J., Fisher, M.L., Janssens-Maenhout, G., Miller, B.R., Miller, J.B., Montzka, S.A., Nehrkorn, T., and Sweeney, C. (2013). Anthropogenic emissions of methane in the United States. *Proceedings of the National Academy of Sciences of the United States of America, 110(50)*, 20018-20022.

Montzka, S.A., Dlugokencky, E.J., and Butler, J.H. (2011). Non-CO_2 greenhouse gases and climate change. *Nature, 476*, 43-50.

Murdock, D.G., Stearns, S.V., Lines, R.T., Lenz, D., Brown, D.M., and Philbrick, C.R. (2008). Applications of real-world gas detection: Airborne Natural Gas Emission Lidar (ANGEL) system. *Journal of Applied Remote Sensing, 2*, 023518.

Murtagh, F., and Heck, A. (1987). *Multivariate data analysis*, D. Reidel Publishing Company, Dordrecht.

Myhre, G., Shindell, D., Breon, F.-M., Collins, W., Fuglestvedt, J., Huang, J., Koch, D., Lamarque, J.-F., Lee, D., Mendoza, B., Nakajima, T., Robock, A., Stephens, G., Takemura, T., and Zhang, H. (2013). Anthropogenic and natural radiative forcing. In: *Climate change 2013: The physical science basis. Contribution of working group I to the fifth assessment report of the Intergovernmental Panel on Climate Change*, Cambridge University Press, Cambridge and New York.

Nisbet, E.G., Dlugokencky, E.J., and Bousquet, P. (2014). Methane on the rise-Again. *Science,*

343, 493-49.

NOAA (2015). National Oceanic and Atmospheric Administration, Earth System Research Laboratory, Global Monitoring Division, *GMD measurement locations*. Retrieved 2 March 2015, from http://www.esrl.noaa.gov/gmd/dv/data/?site=MLO&parameter_name=Methane

NOAA (2013). National Oceanic and Atmospheric Administration, Earth System Research Laboratory, Global Monitoring Division, *GMD measurement locations*. Retrieved 2 March 2015, from http://www.esrl.noaa.gov/gmd/ccgg/trends/global.html

NOAA (2012). National Oceanic and Atmospheric Administration, Earth System Research Laboratory, Global Monitoring Division, *GMD measurement locations*. Retrieved 2 March 2015, from http://www.esrl.noaa.gov/gmd/ccgg/trends/global.html

NRC (2010). National Research Council, *Verifying greenhouse gas emissions: Methods to support international climate agreements*, National Academies Press, Washington, D.C.

Ogunjemiyo, S., Roberts, D.A., Keightley, K., Ustin, S.L., Hinckley, T., and Lamb, B. (2002). Evaluating the relationship between AVIRIS water vapor and poplar plantation evapotranspiration. *Journal of Geophysical Research-Atmospheres, 107(D23)*, 4719.

O'Sullivan, F., and Paltsev, S. (2012). Shale gas production: potential versus actual greenhouse gas emissions. *Environmental Research Letters, 7*, 044030.

Parker, R., Boesch, H., Cogan, A., Fraser, A., Feng, L., Palmer, P.I., Messerschmidt, J., Deutscher, N., Griffith, D.W.T., Notholt, J., Wennberg, P.O., and Wunch, D. (2011). Methane observations from the Greenhouse Gases Observing SATellite: Comparison to

ground-based TCCON data and model calculations. *Geophysical Research Letters, 38*, L15807.

Peischl, J., Ryerson, T.B., Brioude, J., Aikin, K.C., Andrews, A.E., Atlas, E., Blake, D., Daube, B.C., de Gouw, J.A., Dlugokencky, E., Frost, G.J., Gentner, D.R., Gilman, J.B., Goldstein, A.H., Harley, R.A., Holloway, J.S., Kofler, J., Kuster, W.C., Lang, P.M., Novelli, P.C., Santoni, G.W., Trainer, M., Wofsy, S.C., and Parrish, D.D. (2013). Quantifying sources of methane using light alkanes in the Los Angeles Basin, California. *Journal of Geophysical Research-Atmospheres, 118*, 4974-4990.

Petron, G., Frost, G., Miller, B.R., Hirsch, A.I., Montzka, S.A., Karion, A., Trainer, M., Sweeney, C., Andrews, A.E., Miller, L., Kofler, J., Bar-Ilan, A., Dlugokencky, E.J., Patrick, L., Moore, C.T., Ryerson, T.B., Siso, C., Kolodzey, W., Lang, P.M., Conway, T., Novelli, P., Masarie, K., Hall, B., Guenther, D., Kitzis, D., Miller, J., Welsh, D., Wolfe, D., Neff, W., and Tans, P. (2012). Hydrocarbon emissions characterization in the Colorado Front Range: A pilot study. *Journal of Geophysical Research-Atmospheres, 117*, D0430.

Pipkin, B.W., and Proctor, R.J. (1992). *Engineering geology practice in Southern California, Special Publication No. 4, Association of Engineering Geologists, Southern California section.* Star Publishing Company, Belmont.

Platt, U., and Stutz, J. (2008). *Differential optical absorption spectroscopy, Principles and applications.* Springer-Verlag, Berlin.

Platt, U. (1994). *Differential optical absorption spectroscopy (DOAS), In: Air monitoring by spectroscopic techniques.* John Wiley and Sons, New York.

Press, W.H., Teukolosky, S.A., Vetterling, W.T., and Flannery, B.P. (2007). *Numerical recipes: The art of scientific computing, Vol. 3.* Cambridge University Press, Cambridge.

Ravishankara, A.R., Daniel, J.S., and Portmann, R.W. (2009). Nitrous Oxide (N_2O): The dominant ozone-depleting substance emitted in the 21st century. *Science, 326*, 123-125.

Roberts, D.A., Quattrochi, D.A., Hulley, G.C., Hook, S.J., and Green, R.O. (2012). Synergies between VSWIR and TIR data for the urban environment: An evaluation of the potential for the Hyperspectral Infrared Imager (HyspIRI) Decadal Survey mission. *Remote Sensing of Environment, 117*, 83-101.

Roberts, D.A., Bradley, E.S., Cheung, R., Leifer, I., Dennison, P.E., and Margolis, J.S. (2010). Mapping methane emissions from a marine geological seep source using imaging spectrometry. *Remote Sensing of Environment, 114*, 592-606.

Roberts, D.A., Gardner, M., Church, R., Ustin, S., Scheer, G., and Green, R.O. (1998). Mapping chaparral in the Santa Monica Mountains using multiple endmember spectral mixture models. *Remote Sensing of Environment, 65*, 267-279.

Roberts, D.A., Green, R.O., and Adams, J.B. (1997). Temporal and spatial patterns in vegetation and atmospheric properties from AVIRIS. *Remote Sensing of Environment, 62*, 223-240.

Rodgers, C.D. (2000). *Inverse methods for atmospheric sounding, theory and practice.* World Scientific, London.

Rothman, L.S., Gordon, I.E., Barbe, A., Benner, D.C., Bernath, P.E., Birk, M., Boudon, V., Brown, L.R., Campargue, A., Champion, J.P., Chance, K., Coudert, L.H., Dana, V., Devi, V.M., Fally, S., Flaud, J.M., Gamache, R.R., Goldman, A., Jacquemart, D., Kleiner, I., Lacome,

N., Lafferty, W.J., Mandin, J.Y., Massie, S.T., Mikhailenko, S.N., Miller, C.E., Moazzen-Ahmadi, N., Naumenko, O.V., Nikitin, A.V., Orphal, J., Perevalov, V.I., Perrin, A., Predoi-Cross, A., Rinsland, C.P., Rotger, M., Simeckova, M., Smith, M.A.H., Sung, K., Tashkun, S.A., Tennyson, J., Toth, R.A., Vandaele, A.C., and Vander Auwera, J. (2009). The HITRAN 2008 molecular spectroscopic database. *Journal of Quantitative Spectroscopy & Radiative Transfer, 110*, 533-572.

Saitoh, N., Imasu, R., Ota, Y., and Niwa, Y. (2009). CO_2 retrieval algorithm for the thermal infrared spectra of the Greenhouse Gases Observing Satellite: Potential of retrieving CO_2 vertical profile from high-resolution FTS sensor. *Journal of Geophysical Research-Atmospheres, 114*, D17305.

Schepers, D., Guerlet, S., Butz, A., Landgraf, J., Frankenberg, C., Hasekamp, O., Blavier, J.F., Deutscher, N.M., Griffith, D.W.T., Hase, F., Kyro, E., Morino, I., Sherlock, V., Sussmann, R., and Aben, I. (2012). Methane retrievals from Greenhouse Gases Observing Satellite (GOSAT) shortwave infrared measurements: Performance comparison of proxy and physics retrieval algorithms. *Journal of Geophysical Research-Atmospheres, 117*, D10307.

Schneising, O., Bergamaschi, P., Bovensmann, H., Buchwitz, M., Burrows, J.P., Deutscher, N.M., Griffith, D.W.T., Heymann, J., Macatangay, R., Messerschmidt, J., Notholt, J., Rettinger, M., Reuter, M., Sussmann, R., Velazco, V.A., Warneke, T., Wennberg, P.O., and Wunch, D. (2012). Atmospheric greenhouse gases retrieved from SCIAMACHY: Comparison to ground-based FTS measurements and model results. *Atmospheric Chemistry and Physics, 12*, 1527-1540.

Schuck, T.J., Ishijima, K., Patra, P.K., Baker, A.K., Machida, T., Matsueda, H., Sawa, Y.,

Umezawa, T., Brenninkmeijer, C.A.M., and Lelieveld, J. (2012). Distribution of methane in the tropical upper troposphere measured by CARIBIC and CONTRAIL aircraft. *Journal of Geophysical Research-Atmospheres, 117*, D19304.

Shakhova, N., Semiletov, I., Salyuk, A., Yusupov, V., Kosmach, D., and Gustafsson, O. (2010). Extensive methane venting to the atmosphere from sediments of the east siberian arctic shelf. *Science, 327*, 1246-1250.

Shindell, D.T., Faluvegi, G., Koch, D.M., Schmidt, G.A., Unger, N., and Bauer, S.E. (2009). Improved attribution of climate forcing to emissions. *Science, 326*, 716-718.

Shindell, D.T., Walter, B.P., and Faluvegi, G. (2004). Impacts of climate change on methane emissions from wetlands. *Geophysical Research Letters, 31*, L21202.

Stutz, J., Oh, H.J., Whitlow, S.I., Anderson, C., Dibbb, J.E., Flynn, J.H., Rappengluck, B., and Lefer, B. (2010). Simultaneous DOAS and mist-chamber IC measurements of HONO in Houston, TX. *Atmospheric Environment, 44*, 4090-4098.

Theiler, J., and Foy, B.R. (2006). Effect of signal contamination in matched-filter detection of the signal on a cluttered background. *IEEE Geoscience and Remote Sensing Letters, 3*, 98-102.

Thompson, D.R., Leifer, I., Bovensmann, H., Eastwood, M.L., Green, R.O., Eastwood, M.L., Fladeland, M., Frankenberg, C., Gerilowski, K., Green, R.O., Kratwurst, S., Krings, T., Luna, B., and Thorpe, A.K. (2015). Real time remote detection and measurement for airborne imaging spectroscopy: A case study with methane. *Atmospheric Measurement Techniques*, Manuscript submitted.

Thorpe, A.K., Frankenberg, C., Roberts, D.A., et al. (2015). Measuring methane concentrations from a controlled release experiment using the next generation Airborne Visible/Infrared Imaging Spectrometer (AVIRIS-NG). *Remote Sensing of Environment*, Manuscript submitted.

Thorpe, A.K., Frankenberg, C., and Roberts, D.A. (2014). Retrieval techniques for airborne imaging of methane concentrations using high spatial and moderate spectral resolution: Application to AVIRIS. *Atmospheric Measurement Techniques, 7*, 491-506.

Thorpe, A.K., Roberts, D.A., Bradley, E.S., Funk, C.C., Dennison, P.E., and Leifer, I. (2013). High resolution mapping of methane emissions from marine and terrestrial sources using a Cluster-Tuned Matched Filter technique and imaging spectrometry. *Remote Sensing of Environment, 134*, 305-318.

Thorpe, A.K., Roberts, D.A., Dennison, P.E., Bradley, E.S., and Funk, C.C. (2012). Point source emissions mapping using the Airborne Visible/Infrared Imaging Spectrometer (AVIRIS). *Proceedings of SPIE, 8390*, Algorithms and technologies for multispectral, hyperspectral, and ultraspectral imagery XVIII, 839013.

Tobin, D.C., Revercomb, H.E., Moeller, C.C., and Pagano, T.S. (2006). Use of atmospheric infrared sounder high-spectral resolution spectra to assess the calibration of Moderate resolution Imaging Spectroradiometer on EOS Aqua. *Journal of Geophysical Research-Atmospheres, 111*, D09S05.

Townsend-Small, A., Tyler, S.C., Pataki, D.E., Xu, X.M., and Christensen, L.E. (2012). Isotopic measurements of atmospheric methane in Los Angeles, California, USA: Influence of

"fugitive" fossil fuel emissions. *Journal of Geophysical Research-Atmospheres, 117*, D0730.

Tratt, D.M., Buckland, K.N., Hall, J.L., Johnson, P.D., Keim, E.R., Leifer, I., Westberg, K., and Young, S.J. (2014). Airborne visualization and quantification of discrete methane sources in the environment. *Remote Sensing of Environment, 154*, 74-88.

Villeneuve, P.V., Fry, H.A., Theiler, J.P., Clodius, W.B., Smith, B.W., and Stocker, A.D. (1999). Improved matched-filter detection techniques. *Proc. SPIE, 3753*, 278-285.

Wennberg, P.O., Mui, W., Wunch, D., Kort, E.A., Blake, D.R., Atlas, E.L., Santoni, G.W., Wofsy, S.C., Diskin, G.S., Jeong, S., and Fischer, M.L. (2012). On the sources of methane to the Los Angeles atmosphere. *Environmental Science & Technology, 46*, 9282-9289.

White, W.H., Anderson, J.A., Blumenthal, D.L., Husar, R.B., Gillani, N.V., Husar, J.D., and Wilson, W.E. (1976). Formation and transport of secondary air-pollutants - Ozone and aerosols in St-Louis urban plume. *Science, 194*, 187-189.

Woodwell, G.M., Mackenzie, F.T., Houghton, R.A., Apps, M., Gorham, E., and Davidson, E. (1998). Biotic feedbacks in the warming of the earth. *Climatic Change, 40*, 495-518.

Wuebbles, D.J., and Hayhoe, K. (2002). Atmospheric methane and global change. *Earth-Science Reviews, 57*, 177-210.

Wunch, D., Wennberg, P.O., Toon, G.C., Keppel-Aleks, G., and Yavin, Y.G. (2009). Emissions of greenhouse gases from a North American megacity. *Geophysical Research Letters, 36*, L15810.